



Terms and Conditions of Use of Digitised Theses from Trinity College Library Dublin

Copyright statement

All material supplied by Trinity College Library is protected by copyright (under the Copyright and Related Rights Act, 2000 as amended) and other relevant Intellectual Property Rights. By accessing and using a Digitised Thesis from Trinity College Library you acknowledge that all Intellectual Property Rights in any Works supplied are the sole and exclusive property of the copyright and/or other IPR holder. Specific copyright holders may not be explicitly identified. Use of materials from other sources within a thesis should not be construed as a claim over them.

A non-exclusive, non-transferable licence is hereby granted to those using or reproducing, in whole or in part, the material for valid purposes, providing the copyright owners are acknowledged using the normal conventions. Where specific permission to use material is required, this is identified and such permission must be sought from the copyright holder or agency cited.

Liability statement

By using a Digitised Thesis, I accept that Trinity College Dublin bears no legal responsibility for the accuracy, legality or comprehensiveness of materials contained within the thesis, and that Trinity College Dublin accepts no liability for indirect, consequential, or incidental, damages or losses arising from use of the thesis for whatever reason. Information located in a thesis may be subject to specific use constraints, details of which may not be explicitly described. It is the responsibility of potential and actual users to be aware of such constraints and to abide by them. By making use of material from a digitised thesis, you accept these copyright and disclaimer provisions. Where it is brought to the attention of Trinity College Library that there may be a breach of copyright or other restraint, it is the policy to withdraw or take down access to a thesis while the issue is being resolved.

Access Agreement

By using a Digitised Thesis from Trinity College Library you are bound by the following Terms & Conditions. Please read them carefully.

I have read and I understand the following statement: All material supplied via a Digitised Thesis from Trinity College Library is protected by copyright and other intellectual property rights, and duplication or sale of all or part of any of a thesis is not permitted, except that material may be duplicated by you for your research use or for educational purposes in electronic or print form providing the copyright owners are acknowledged using the normal conventions. You must obtain permission for any other use. Electronic or print copies may not be offered, whether for sale or otherwise to anyone. This copy has been supplied on the understanding that it is copyright material and that no quotation from the thesis may be published without proper acknowledgement.

University of Dublin
Trinity College



Interactions at Nano-Bio Interfaces

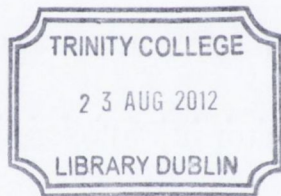
A thesis submitted to the University of Dublin,
Trinity College in applications for the degree of
Doctor of Philosophy

by

Aliaksandra Rakovich

School of Physics

October, 2011



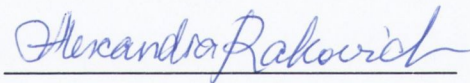
Thesis 954

To my friends and family

DECLARATION

I declare that this thesis has not been submitted as an exercise for a degree at this or any other university. The work presented is entirely my own work, apart from the assistance mentioned in the acknowledgements. The work of others was duly acknowledged in the text whenever included.

I agree to deposit this thesis in the University's open access institutional repository or allow the library to do so on my behalf, subject to Irish Copyright Legislation and Trinity College Library conditions of use and acknowledgement.

A handwritten signature in blue ink, reading "Aliaksandra Rakovich", is written over a horizontal line.

Aliaksandra Rakovich

SUMMARY

The development of new materials that can be integrated into current technologies is one of the most important challenges of today. As a result, fields such as nanotechnology and biotechnology have seen great advances. More recently, a link between these two fields has been established and has resulted in nano-biosciences being considered to be an important economic factor by many. The field of nanobiotechnology continuously test the boundaries and promises many breakthrough results in the near future. The purpose of this work was thus to add to and advance this very promising field with an emphasis on biomolecules with technologically exploitable properties. In order to achieve this, the interactions between nanomaterials and biomaterials were studied at nanoscale, with further investigations into the effects that these interactions have on the functionalities of biomolecules. Three model systems were chosen for the investigations based on the range of potential applications that they can provide. Semiconductor quantum dots (QDs) were selected as the nanomaterials component in each of these systems.

In Chapter 1, the motivation behind this work is described in a little more detail. It also includes an introduction to semiconductor QDs and a short overview of the state-of-the-art on nanobiotechnology. This is followed by a description of methods and techniques that were common to each of the three model systems (Chapter 2). Chapter 3 introduces the first model system composed from a photosensitiser molecule (methylene blue dye) and QDs. The effect of the energy and charge transfer from QDs to the photosensitiser is examined in terms of the photodynamic efficiency of the dye and its ability to inhibit the growth of cancerous cells in vitro. In Chapter 4, QDs are employed as light-collecting elements instead of the naturally-occurring light-harvesting complexes of photosynthetic reaction centres. This model system reveals great potential for the utilization of QDs in artificial photosynthetic devices. Finally, research involving the third model system, containing bacteriorhodopsin (bR) membrane protein, is described in Chapters 5 and 6. In Chapter 5, the bR/QD system is first introduced and examined for energy transfer interactions, as well as the effect of these interactions on the in-built functionality of the protein (proton pumping). In Chapter 6 the effect of the nanoscale interactions on the nonlinear optical properties of the bR/QD material is investigated.

ACKNOWLEDGEMENTS

First of all, I would like to thank my family for their love, support and patience during the last four years and for never letting me settle for less than I can be. A special thanks to my dad for constantly driving me forward and all of his help along the way.

I wish to express my gratitude to my supervisor Prof. John Donegan for accepting me into his group and for his support and guidance along the way.

I would also like to acknowledge our many collaborators, without who this project would not have been the same. In particular, a special thanks to Prof. Nabiev and Dr. Alyona Sukhanova for your assistance with the bio-related side of this thesis and also for your hospitality during my stay in San Sebastian. In the group of Prof. Nabiev, Nicolas Bouchonville and Michael Molinari are acknowledged for the AFM imaging of the quantum dot/bacteriorhodopsin hybrids. Dr. Alyona Sukhanova is acknowledged for the chemical conjugation of quantum dots with the bacteriorhodopsin protein and reaction centres. I would also like to thank our Russian collaborators, and in particular, Evgeniy Lukashev from the Lomonosov Moscow State University and Vladimir Oleinikov from Russian Academy of Sciences for the extraction and purification of the bacterial reaction centres and the measurements of proton pumping by bacteriorhodopsin. In addition, I would like to thank Prof. Vincent Kelly in the RNA Biology Group (TCD) for the use of his facilities and help with the in vitro studies of cancerous cell lines. I would like to thank Prof. Alexander Govorov for providing theoretical support. Finally, a special thanks to Prof. Yury Gun'ko, Dr. Mikhail Artemyev and Dr. Nikolai Gaponik for their expertise and for the synthesis of semiconductor QDs used as part of this project.

I would like to thank the Irish Research Council of Science, Engineering and Technology and Trinity College Dublin for funding my PhD.

Finally, I would like to give special thanks all my friends for making this experience an enjoyable one.

Aliaksandra Rakovich

PUBLICATIONS

S. J. Byrne, Y. Williams, A. Davies, S. A. Corr, Aliaksandra Rakovich, Y. K. Gun'ko, Y. P. Rakovich, J. F. Donegan, Y. Volkov. *"Jelly-dots": Synthesis and Cytotoxicity Studies on CdTe Quantum Dot-Gelatin Nanocomposites*. *Small* **3**, 1152-1156 (2007)

Aliaksandra Rakovich, V. Stockhausen, A. S. Susha, S. Sapra, A. L. Rogach. *Decorated wires as a reaction product of the microwave assisted synthesis of CdSe in the presence of glycine*. *Colloids and Surfaces A: Physicochemical and Engineering Aspects* **317**, 737-741 (2008)

Aliaksandra Rakovich, Y. P. Rakovich, J. F. Donegan. *Optical studies of Methylene Blue – Semiconductor Nanocrystals Hybrid System*. *e-Journal of Surface Science and Nanotechnology* **7**, 349-353 (2009)

Aliaksandra Rakovich, A. Sukhanova, N. Bouchonville, M. Molinari, M. Troyon, J. H. M. Cohen, Y. P. Rakovich, J. F. Donegan, I. Nabiev. *Energy Transfer Processes in Semiconductor Quantum Dots – Bacteriorhodopsin Hybrid System*. *Proceedings of SPIE* **7366**, 736620 (2009)

Aliaksandra Rakovich, T. Rakovich, V. Kelly, V. Lesnyak, A. Eychmüller, Y. P. Rakovich, J. F. Donegan. *Photosensitizer Methylene Blue – Semiconductor Nanocrystals Hybrid System for Photodynamic Therapy*. *Journal of Nanoscience and Nanotechnology* **10**, 2656-2662 (2010)

Aliaksandra Rakovich, D. Savateeva, T. Rakovich, J. F. Donegan, Y. P. Rakovich, V. Kelly, V. Lesnyak, A. Eychmüller. *CdTe Quantum Dot / Dye Hybrid System as Photosensitizer for Photodynamic Therapy*. *Nanoscale Research Letters* **5**, 753-760 (2010)

Aliaksandra Rakovich, A. Sukhanova, N. Bouchonville, E. Lukashev, V. Oleinikov, M. Artemyev, V. Lesnyak, N. Gaponik, M. Molinari, M. Troyon, Y. P. Rakovich, J. F. Donegan, I. Nabiev. *Resonance Energy Transfer Improves the Biological Function of Bacteriorhodopsin within a hybrid Material Built from Purple Membranes and Semiconductor Quantum Dots*. *NanoLetters* **10**, 2640-2648 (2010)

I. Nabiev, Aliaksandra Rakovich, A. Sukhanova, E. Lukashev, V. Zagidullin, V. Pachenko, Y. P. Rakovich, J. F. Donegan, A. B. Rubin, A. O. Govorov. *Fluorescent Quantum Dots as Artificial Antennas for Enhanced Light Harvesting and Energy Transfer to Photosynthetic Reaction Centers*. *Angewandte Chemie International Edition* **49**, 7217-7221 (2010)

CONFERENCES

Nanocrystals-Bacteriorhodopsin hybrid material for integrated biological-semiconductor nanodevices. Aliaksandra Rakovich, Y. P. Rakovich, Y. Gun'ko, J. F. Donegan, A. Sukhanova, I. Nabiev. Oral presentation. 3rd International Conference on Nanomaterials and Nanomanufacturing, 17-18 December 2007, Trinity College Dublin, Ireland.

Nanocrystals-Bacteriorhodopsin hybrid material for integrated biological-semiconductor nanodevices. Aliaksandra Rakovich, Y. P. Rakovich, J. F. Donegan, Y. Gun'ko, A. Sukhanova, I. Nabiev. Poster presentation. 2nd International Conference on Advanced Nanomaterials, 22-25 June 2008, Aveiro, Portugal.

Photosensitizer Methylene Blue – Semiconductor Nanocrystals hybrid system for Photodynamic Therapy. Aliaksandra Rakovich, T. Rakovich, V. Kelly, Y. P. Rakovich, J. F. Donegan. Poster presentation. 2nd International Conference on Advanced Nanomaterials, 22-25 June 2008, Aveiro, Portugal.

Methylene Blue – Semiconductor Nanocrystals hybrid system for solar energy conversion applications. Aliaksandra Rakovich, Y. P. Rakovich, J. F. Donegan. Poster presentation. 14th International Conference on Solid Films and Surfaces, 29th June – 4th July 2008, Trinity College Dublin, Ireland.

Methylene Blue – Semiconductor Nanocrystals Hybrid System for Photodynamic and Photochemical Applications. Aliaksandra Rakovich, T. Rakovich, V. Kelly, Y. P. Rakovich, J. F. Donegan. Poster presentation. 22nd General Conference of the Condensed Matter Division of the European Physical Society, 25-29 August 2008, University of Roma La Sapienza, Rome, Italy.

Hybrid Material from Fluorescent Quantum Dots and Photochromic Membrane Protein Bacteriorhodopsin: Engineering and Dynamic Optical Switching Applications. Aliaksandra Rakovich, P. Gilliot, S. Haacke, A. Sukhanova, N. Bouchonville, M. Molinari, M. Troyon, J. H. M. Cohen, Y. P. Rakovich, J. F. Donegan, I. Nabiev. Poster presentation. Hybrid Materials Conference, 15-19 March 2009, Tours, France.

Energy Transfer Processes in Semiconductor Quantum Dots – Bacteriorhodopsin Hybrid System. Aliaksandra Rakovich, A. Sukhanova, N. Bouchonville, M. Molinari, M. Troyon, J. H. M. Cohen, Y. P. Rakovich, J. F. Donegan, I. Nabiev. Poster presentation. Photonic Materials, Devices and

Applications Conference, SPIE Symposium on Microtechnologies for the New Millennium. 4-6 May 2009, Dresden, Germany.

Development of a Functional Nano-Bio Hybrid Material Based on Energy Transfer between Semiconductor Quantum Dots and Photochromic Protein Bacteriorhodopsin. Aliaksandra Rakovich, A. Sukhanova, Y. P. Rakovich, I. Nabiev, J. F. Donegan. Poster presentation. Photonics Ireland 2009 conference. 13-16 September 2009, Kinsale, Ireland.

Energy Transfer in Hybrid Material Engineered from Photochromic Membrane Protein Bacteriorhodopsin and Semiconductor Quantum Dots. Aliaksandra Rakovich, A. Sukhanova, N. Bouchonville, M. Molinari, M. Troyon, Y. P. Rakovich, J. F. Donegan, I. Nabiev. Poster presentation. Nano2009 workshop/Atom-by-Atom conference, 28-30 September 2009, San Sebastian, Spain.

Energy Transfer in Hybrid Material Engineered from Bacteriorhodopsin and Semiconductor Quantum Dots. Aliaksandra Rakovich, A. Sukhanova, N. Bouchonville, M. Molinari, M. Troyon, Y. P. Rakovich, J. F. Donegan, I. Nabiev. Poster presentation. Inspire-09 Conference (NanoWeek). 30th November – 1st December, Cork, Ireland.

Development of Nano-Bio Hybrid Material Based on CdTe Quantum Dots and Bacteriorhodopsin Protein for Future Technologies. Aliaksandra Rakovich, A. Sukhanova, E. Lukashev, N. Bouchonville, V. Oleinikov, M. Artemyev, N. Gaponik, M. Molinari, M. Troyon, Y. P. Rakovich, J. F. Donegan, I. Nabiev. Oral presentation. 11th International Conference on Trends in Nanotechnology, 6-10 September 2010, International Iberian Nanotechnology Laboratory, Braga, Portugal.

Colloidal Semiconductor Quantum Dots as Light-Harvesting Elements for Artificial Photosynthesis Applications. Aliaksandra Rakovich, I. Nabiev, A. Sukhanova, E. Lukashev, V. Zagidullin, V. Pachenko, Y. P. Rakovich, J. F. Donegan, A. B. Rubin, A. O. Govorov. Poster presentation. Globe Forum Dublin 2010, 17-18th November, Dublin, Ireland.

Semiconductor Quantum Dots as Light-Harvesting Antennae for Artificial Photosynthesis Applications. Aliaksandra Rakovich, A. Sukhanova, E. Lukashev, V. Zagidullin, V. Pachenko, A. B. Rubin, I. Nabiev, A. O. Govorov, Y. P. Rakovich, J. F. Donegan. Poster presentation. Photonics Ireland 2011 conference, 7-9th September 2011, Malahide, Ireland.

ABBREVIATIONS & ANNOTATIONS

Units

°C	Celsius
a.u.	Arbitrary units
eV	Electron volt
g	Standard gravity or gram
K	Kelvin
Da	Dalton
L	Litre
m	Metre
M	Molar (concentration)
Hz	Hertz
min	Minute
mol	Mole
V	Volt
rpm	Revolutions per minute
s or sec	Second
W	Watt

Mathematical symbols

A	Absorbance
C	Concentration
d or D	Diameter
D_i	Diffusion coefficient of species i
E	FRET efficiency
E_g or ΔE	Bandgap energy
$G(t)$	Correlation intensity at time lag t
h	Planck's constant
$J(\lambda)$	Spectral overlap integral
I	Signal intensity or Irradiance
k	Kinetic rate constant or wavevector ($= 2\pi/\lambda$)

k_v	Eccentricity of effective excitation volume
l or L	Sample length, width or thickness
L_{eff}	Effective sample thickness
n	Linear refractive index
n_2	Nonlinear refractive index
$\langle N \rangle$	Average number of particles
N_A	Avogadro's number
Q_D	Quantum yield of a donor
r	Radius or separation distance
R_0	Förster radius
S	Aperture transmittance
t	Time or time lag
T (ΔT)	Transmittance (change)
V_{eff}	Effective excitation volume
w_0	Lateral focal radius or beam waist
x	Molar ratio
Z_0	Focal length along optical axis
α	Linear absorption coefficient
β	Nonlinear absorption coefficient
ε	Extinction coefficient
κ^2	Dipole orientation factor
λ	Wavelength
τ_i	Lifetime or diffusion length of species i
ν	Frequency
$\Delta\Phi_0$	Phase change due to nonlinear refraction
$\Delta\Psi_0$	Phase change due to nonlinear absorption

Chemical groups and compounds

$^1\text{O}_2$	Singlet oxygen
^3MB	Triplet excited state of methylene blue
ADP	Adenosine Diphosphate
Al_2Te_3	Aluminium Telluride
ATP	Adenosine Triphosphate
$\text{Cd}(\text{ClO}_4)_2$	Cadmium perchlorate

CdSe	Cadmium Selenide
CdTe	Cadmium Telluride
CO ₂	Carbon Dioxide
-COOH	Carboxylic acid group
Cys	Cysteine
D ₂ O	Heavy water
DMSO	Dimethyl sulfoxide
DNA	Deoxyribonucleic acid
EDTA	Ethylenediaminetetraacetic acid
H ⁺	Proton
H ₂ O	Water
H ₂ SO ₄	Sulphuric Acid
HCl	Hydrochloric acid
HDA	Hexadecylamine
ITO	Indium Tin Oxide
LDAO	Lauryl dimethylamine oxide
MB	Methylene Blue
N ₂	Nitrogen (gas)
Na	Sodium
NaOH	Sodium Hydroxide
-NH ₂	Amino group
-OH	Hydroxyl group
PEG	Polyethylene glycol
PO ₃ ⁻	Phosphite
TGA	Thiol-glycolic acid
TOP	Trioctylphosphine
TOPO	Trioctylphosphine oxide
Tris-HCl	tris(hydroxymethyl)aminomethane hydrochloride
ZnS	Zinc Sulphide

Other abbreviations

2-D	Two-dimensional
3-D	Three-dimensional
AFM	Atomic Force Microscopy

AGR	Aggregated
APS	Artificial Photosynthetic (e.g device)
B	Bacteriochlorophyll
bR	Bacteriorhodopsin protein
CB	Covalence Band
CC	Chemically conjugated
D96N	Bacteriorhodopsin mutant
DLS	Dynamic Light Scattering
EPR	Enhanced Permeability and Retention
FCS	Fluorescence Correlation Spectroscopy
FRET	Förster Resonance Energy Transfer
FWHM	Full-Width Half-Maximum
H	Bacteriopheophytin
LH	Light-harvesting
MPA	Multi-photon absorption
NC(s)	Nanocrystal(s)
NIR	Near Infra-Red (spectral region)
NLA	Nonlinear absorption
NLO	Nonlinear optical (e.g. properties)
NLR	Nonlinear refraction
NP(s)	Nanoparticle(s)
P or P870	Special pair
PDT	Photodynamic Therapy
PDT	Photoinduced charge transfer
PM(s)	Purple Membrane(s)
PS	Photosensitiser
PS	Photosynthetic (e.g. system)
PTL(s)	Proteoliposome(s)
PV	Photovoltaic
Q	Quinone
QD(s)	Quantum Dot(s)
QY	Quantum Yield
RC(s)	Reaction Centre(s)
ROS	Reactive Oxygen Species

SA	Self-assembled
TCSPC	Time-Correlated Single Photon Counting
TTTR	Time-Tagged Time-Resolved
UV	Ultra-Violet (spectral region)
UV-Vis	Absorption spectroscopy
VB	Valence Band
Vis	Visible (spectral region)
WD	Well-dispersed
WM(s)	White Membrane(s)
WT	Wild-type (bacteriorhodopsin)

TABLE OF CONTENTS

CHAPTER 1 – INTRODUCTION	1
1.1. Biomaterials for technological applications	3
1.2. Nanomaterials – Quantum Dots	4
1.2.1. Size-quantization in Quantum Dots	4
1.2.2. Optical properties of Quantum Dots	5
1.2.3. Quantum Dots and Förster Resonance Energy Transfer	7
1.2.4. Advantages of Quantum Dots over fluorescent dyes	10
1.3. Nanobiotechnology research and Quantum Dots	12
References	14
CHAPTER 2 – MATERIALS AND METHODS	21
2.1. Quantum Dots preparation and characterization	21
2.1.1. Cadmium Telluride Quantum Dots	21
2.1.2. Cadmium Selenide / Zinc Sulphide Quantum Dots	23
2.1.3. Initial characterisation of Quantum Dot samples	24
2.2. Spectroscopic measurements	27
2.2.1. Steady-state spectroscopic measurements	27
<i>Absorption spectroscopy</i>	27
<i>Photoluminescence spectroscopy</i>	27
<i>Deconvolution of spectra into contributions from constituents</i>	29
2.2.2. Time-resolved photoluminescence measurements	29
<i>Fluorescence measurements</i>	29
<i>Fluorescence Correlation Spectroscopy</i>	30

2.3. Other techniques	34
2.3.1. Zeta potential and nanoparticles size measurements	34
References	36

CHAPTER 3 – PHOTOSENSITISER / QUANTUM DOT SYSTEM **37**

3.1 Introduction	37
3.1.1. Photodynamic therapy	37
3.1.2. Use of Quantum Dots in medicine	38
3.1.3. Methylene Blue as a photosensitiser	39
3.2. Interaction in MB/QD complexes	41
3.2.1. Sample preparation and labelling	41
3.2.2. Assembly of MB/QD complexes	42
3.2.3. Mechanism of photoluminescence quenching	46
3.3. Photodynamic properties of MB/QD complexes	49
3.3.1. Production of singlet oxygen	49
3.3.2. Cell growth in the presence of PS/QD complexes	50
3.4. Conclusions	54
References	55

CHAPTER 4 – QUANTUM DOTS AS LIGHT-HARVESTING ANTENNAE **57**

4.1. Mimicking natural photosynthesis	59
4.1.1. Bacterial photosynthesis	59
4.1.2. Bacterial reaction centres	60
4.1.3. Artificial photosynthesis	62

4.2. Sample preparation	65
4.2.1. Extraction and purification of reaction centres	65
4.2.2. Properties of extracted reaction centres	66
4.2.3. Reaction centre / quantum dot assembly	68
4.3. Energy transfer in QD/RC complexes	70
4.3.1. Photoluminescence of self-assembled complexes	70
4.3.2. Covalently linked complexes	73
4.3.3. Time-resolved photoluminescence measurements	75
4.3.4. Special pair emission in QD/RC complexes	76
4.4. Conclusions	79
References	80

CHAPTER 5 – PROTEIN-BASED PHOTOCROMIC MATERIAL **83**

5.1. Bacteriorhodopsin protein	84
5.1.1. Purple membranes (PMs)	84
5.1.2. Bacteriorhodopsin – structure and function	86
5.1.3. Applications of bacteriorhodopsin	88
5.1.4. Bacteriorhodopsin and semiconductor nanocrystals	89
5.2. Preparation of PM/QD material	92
5.2.1. QD/PM complex formation	92
5.2.2. Self-assembly of QDs on PMs	93
5.3. Investigations of energy transfer	96
5.3.1. Verification of energy transfer occurrence	96
5.3.2. Parameters affecting energy transfer	98
<i>Quantum Dots' diameter</i>	100
<i>Quantum Dots' composition</i>	102
<i>Quantum Dots' surface charge and pH of solution</i>	102

<i>Covalent conjugation</i>	104
<i>Mutation of bacteriorhodopsin</i>	105
5.4. Proton pumping	107
5.5. Conclusions	109
References	110

CHAPTER 6 – NONLINEAR OPTICAL PROPERTIES OF QUANTUM DOT / BACTERIORHODOPSIN MATERIAL **113**

6.1. Nonlinear properties of materials	113
6.2. The Z-scan technique	115
6.2.1. Measurements of nonlinear absorption and refraction	115
6.2.2. Extraction of nonlinear coefficients from Z-scan data	118
6.2.3. Z-scan set-up	119
6.3. Optical nonlinearities in bR/QD material	120
6.3.1. Assembly of PM/QD complexes	120
6.3.2. Enhancement of nonlinear optical properties of bR	121
<i>Temporal evolution of n_2</i>	123
<i>Effect of QD aggregation</i>	123
6.3.3. Origin of n_2 enhancement	126
<i>Wavelength dependence of n_2 enhancement</i>	126
<i>FRET contribution to n_2 enhancement</i>	129
6.4. Conclusions and future work	130
References	132

CHAPTER 7 – CONCLUSIONS **133**

APPENDICES

135

A. Determination of effective excitation volume for FCS **135**

A.1. FCS measurements on a dilution series of a dye 135

A.2. Raster scanning of sub-resolution fluorescent particles 136

B. Cell counting using haemocytometer **138**

B.1. Introduction to the technique 138

B.2. Protocol for cell counting 138

1. INTRODUCTION

The increasing energy demands (by both the developing and developed countries), the drive for technological advancement and concurrent ever-approaching limits of the semiconductor industry have all made the development of new materials one of the most crucial challenges of today. The demand for new materials has inspired scientists to expand their research beyond the standard materials and techniques.

One of the earliest alternative materials to be considered for technological applications were biomaterials. Optimised over millions of years by evolution, the complexity, functionality, sustainability and efficiency of some of the bio-systems cannot be rivalled despite the extraordinary scientific advancements of the last centuries. More recently, the discovery of chemical methods to produce nano-sized particles has sparked the conception of nanotechnology. Nanomaterials possess unique properties that can vary significantly from those of their bulk counterparts; moreover, these properties can be tuned to requirements by manipulation of nanoparticles' (NPs) size. Both of these fields contributed appreciably towards the field of materials development with the discovery of some extraordinary materials (such as the bacteriorhodopsin protein and graphene).

Recent years have seen the emergence of a new field in the materials research that still remains largely unexplored – nanobiotechnology. Broadly defined as the amalgamation of the nano- and bio- technologies, the field is in its infancy with the main research directions still being defined. The interface of these fields is most promising in that it would combine the unique properties of the nanomaterials with the complex performance of the bio-systems. The possible applications of these nano-bio materials should span from the medical to technological applications, and perhaps provide a way to better interface the two. As such, nanobiotechnology has enormous potential for many breakthrough discoveries in advanced materials research.

The main topics of nanobiotechnology can be roughly divided into only a few categories, such as the applications of nanomaterials in biosciences (medicine, diagnostics), bacterial production of nanomaterials, and utilisation of biomaterials as templates for production of ordered nanoparticulate films. A much more exciting prospect of nanobiotechnology is the development of nano-bio hybrids that would take advantage of the properties of both the nano- and bio- materials. For example, one can postulate that incorporation of NPs can greatly

enhance the exploitable properties of bio-materials, endorsing the integration of these hybrid materials in technological applications.

The main aim of this work was to look at the viability of this approach for the development of next-generation photonic materials (Figure 1.1). In particular, three model systems were looked at with possible applications in medicine, green energy technology and optical communications. Due to the complexity and varied functionalities of these chosen bio-systems, the introductions to each are given in later chapters. Here, only the possibilities of biomaterials are discussed briefly, followed by an introduction to the nanomaterials (in particular, quantum dots) and the application of these.

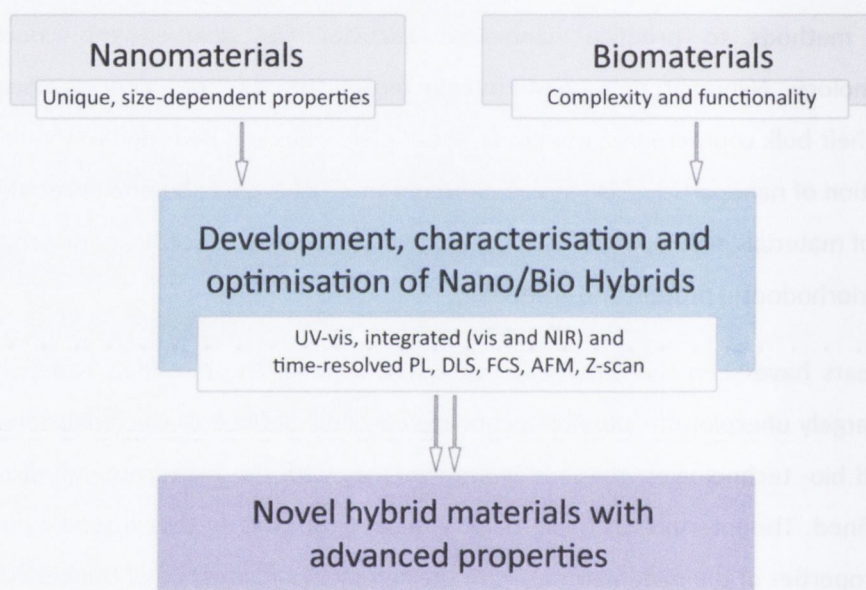


Figure 1.1| Flow-chart of the project. The integration of nano- and bio- materials into nano/bio hybrids can exploit the merits of each. Hybrids were characterised and optimised using a well-established spectroscopic platform with the aim of developing hybrid materials with advanced functional properties.

1.1. Biomaterials for technological applications

Biotechnology recognises the exquisite nature of the biological systems and applies the recently gained understanding of the structure and function of many of these systems to fabricate functional devices.

The viability of the use of such “molecular devices” can be attested to by considering the many merits of bio-materials over conventional materials – the ability of these systems to self-assemble, and the level of the molecular recognition required for this, is particularly remarkable. For example, the components of photosynthetic systems will reconstitute into the original complexes [1, 2], purified membrane proteins dissolved in solutions containing phospholipids will form ordered structures within lipid bilayer membranes [3-7], and two complementary DNA strands will assemble into a double helix structure – a process known as DNA hybridisation [8].

The progressive insight into the structure and function of the bio-systems over the last few decades provided methods for the extraction of these systems from their natural habitat without the loss of their functionalities [9], and the ability to alter and fine-tune these systems for a specific application using genetic engineering (mutagenesis) at a molecular level [10]. Both the self-assembly and the genetic modification provide sophisticated control over the manipulation of the structure and function of biomaterials.

Millions of years of evolution have often solved problems similar to those that man attempts to solve in materials development research through perfection of the built-in functionalities of biological systems on an atom-by-atom basis. As a result, biosystems often perform at efficiencies close to theoretic (thermodynamic) maxima with only minimum energy requirements, further attesting the promise of biomaterials for the development of next-generation materials [11].

The biggest challenge in the implementation of biomaterials in technological applications is a perception that, in contrast to conventional solid state materials, biomaterials are “soft” and thus not capable of providing the sort of stability and cyclicity that is required. This, however, is not always the case, as is demonstrated by a number of organisms that live under extreme conditions including extreme pH values, salt concentrations and high and low temperatures [12].

1.2. Nanomaterials – Quantum Dots

Nanomaterials research is an interdisciplinary subject that involves physicists, chemists, material scientists, biochemists, medics and engineers working together with the aim of progression of this highly dynamic and growing field [13]. Today, nanomaterials encompass a large range of materials such as graphene, carbon nanotubes and a variety of nanoparticles each possessing unique and often superior properties relative to their bulk counterparts. The immense and varied interest in nanoparticles arises from the finding that many of these properties (optical, catalytic, magnetic or electronic) depend not only on the chemical composition of the nanoscale materials, but also on their size [14] allowing fine-tuning of the properties according to requirements. For example, the optical properties of nano-sized crystals of semiconductor material, known as Quantum Dots (QDs), can be tuned by adjustments of their size [15].

1.2.1. Size-quantization in Quantum Dots.

Bulk semiconductors have full valence bands and empty conduction bands at 0 K, but the latter become occupied at finite temperatures [16]. The optical transitions in semiconductors are defined by the energy gap between these two bands, known as a band gap (Figure 1.2(a)). When an electron is promoted into the conduction band, it leaves a hole in the valence band and, in crystalline semiconductors, the electron and the hole weakly couple to form an exciton. Theoretically, the exciton can be treated as a hydrogen atom-like entity, and from this formulation the exciton binding energy and also the average electron-hole separation (Bohr-exciton radius) can be calculated [16].

Colloidal QDs are crystalline particles of semiconductor material of 2 to 10 nm in diameter, which are surrounded by a shell of ligand molecules. The ligand shell prevents the aggregation of QDs in solution and also defines their chemical properties, such as miscibility and solubility [13]. The size-dependent optical properties of QDs arise from the fact that their size is of the order of or smaller than the Bohr-exciton radius. The result is the confinement of the exciton by the potential well, defined by the particle boundaries, giving rise to size quantization effects [15]. In essence, this situation is equivalent to that of a particle-in-a-box problem, in which the spacing of energy levels is inversely proportional to the size of the confining potential. For QDs, discrete energy levels “split off” from the edges of the two bands and the separation between these is inversely defined by QD’s size (Figure 1.2(a)).

1.2.2. Optical properties of Quantum Dots

As a consequence of the quantum confinement effects, the optical properties of QDs are a function of their size. The absorption spectrum of a solution of QDs is a superposition of peaks corresponding to optical transitions between *discrete* hole and electron energy levels (indicated by arrows in Figure 1.2(b)). Upon absorption of a photon by a QD, the excited electron quickly decays (thermally) to the lowest excited level. It then recombines with the hole in the valence band with an emission of a photon, whose energy is equal to the band gap energy of the QD (Figure 1.2(a)). Thus, the emission spectrum of a single QD is just a narrow line at the band gap energy and, for any given material, the emission line of the QD can be tuned simply by adjusting its size (Figure 1.2(c)).

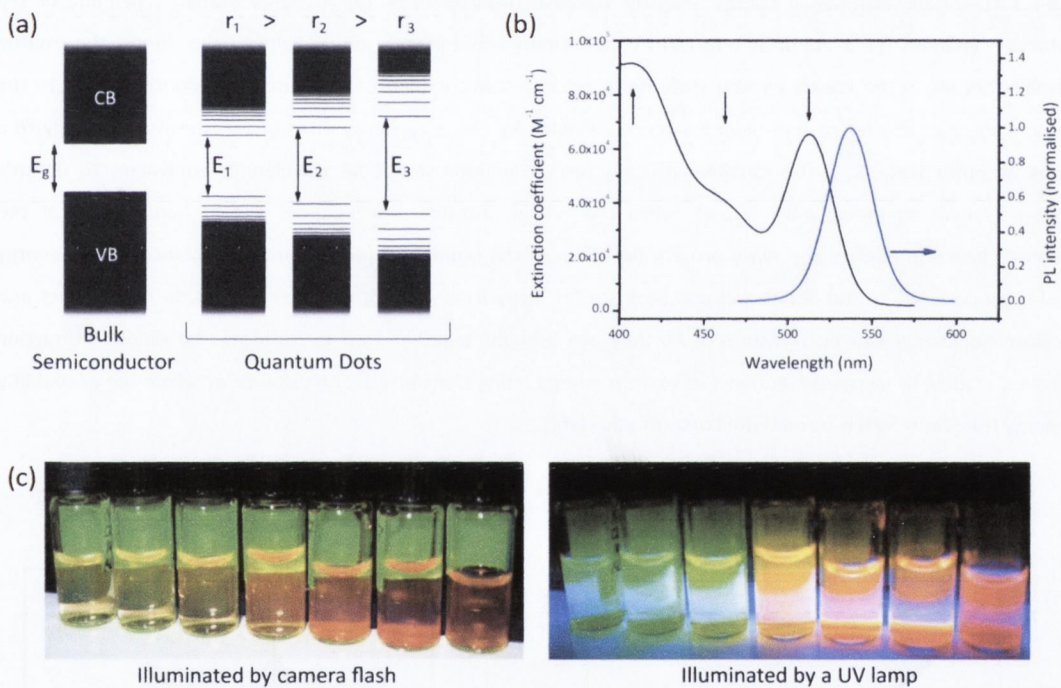


Figure 1.2| Optical properties of semiconductor quantum dots. (a) A schematic representation comparing band structures of bulk semiconductors and those of semiconductor quantum dots. Bulk semiconductors have continuous valence and conduction bands (VB and CB respectively), while quantum dots have discrete energy levels at the bands' edges. Due to size-quantisation effects, the bandgap of a QD increases ($E_1 < E_2 < E_3$) as the size of the QD is reduced ($r_1 > r_2 > r_3$). **(b)** The QDs' absorption spectrum (black curve, left axis) is a superposition of lines corresponding to optical transitions between discrete energy levels (indicated by black arrows). The emission spectrum (blue curve, right axis) is a single peak at the bandgap energy. The peak has a Gaussian profile due to the distribution of QDs sizes within a sample. The spectra shown are those of CdSe/ZnS core-shell QDs emitting at 530 nm. **(c)** A series of QD samples of increasing diameters (left-to-right), illuminated by a camera flash (absorption) and a standard UV lamp (emission), showing shifts of optical bands towards lower energies.

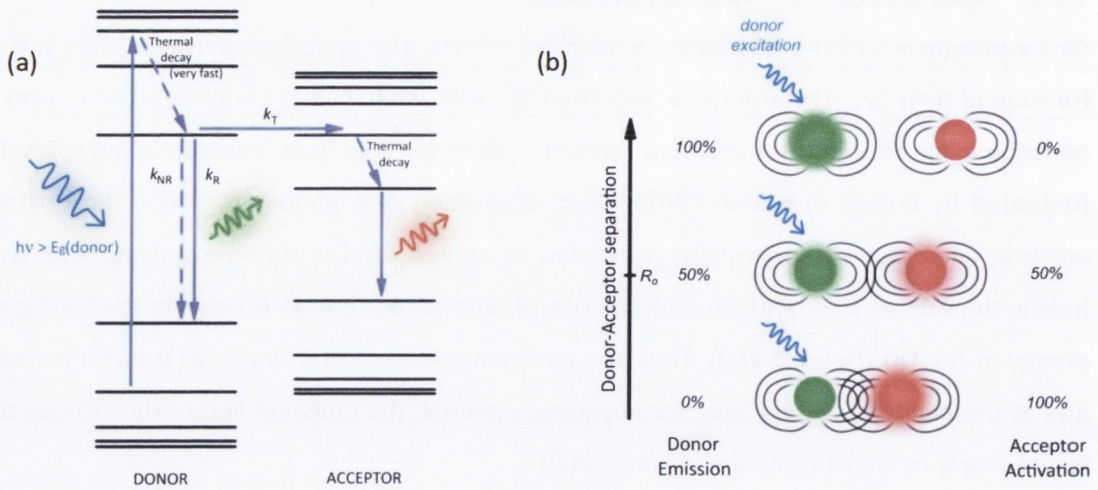


Figure 1.3| Förster Resonance Energy Transfer between fluorophores. (a) A representative schematic of the excitation dynamics for a donor-acceptor FRET pair. Upon initial absorption of light by the donor, the exciton thermally decays to the lowest excited state (very quick in semiconductor QDs). After this, donor returns to the ground state via radiative or non-radiative processes with k_R and k_{NR} decay rates or via transfer of energy to a nearby acceptor (rate k_T). The radiative process results in fluorescence at wavelength equivalent to donor’s bandgap (shown by green wavy arrow), while the energy transfer process gives rise to fluorescence at the acceptor’s bandgap energy (red wavy arrow). **(b)** Effect of the donor-acceptor separation distance on the energy transfer process. When the donor and acceptor are far away from each other, their dipoles do not interact and therefore no energy can be transferred. As they are brought together (top to bottom), the dipole interaction improves, leading to increased amounts of exciton energy being transferred. The distance at which the probability of energy transfer is 50% is termed the Förster radius (R_0).

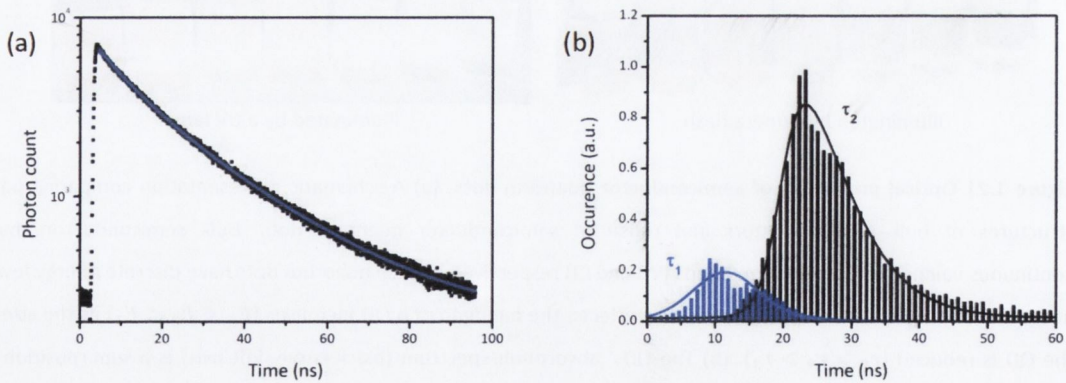


Figure 1.4| Decay of fluorescence in semiconductor QDs. (a) A typical fluorescence decay curve for a QD sample is not linear when plotted on a log Y-scale, indicating multi-exponential decay – usually, bi-exponential. **(b)** The values of the two contributing lifetimes (τ_1 and τ_2) can be extracted from the decay curve. Both of these have a Gaussian-like profile, similar to the distribution of QDs’ sizes.

A typical sample of colloidal QDs has a Gaussian-like distribution of diameters and, as a result, the emission spectrum of a colloidal QDs solution also has a Gaussian-like profile (Figure 1.4(b)). Similarly, exciton lifetimes also have a distribution of values (Figure 1.4(b)).

Time-resolved measurements typically show a double-exponential decay of fluorescence, with a faster and a slower component (Figure 1.4). The shorter lifetime – the faster component – is usually attributed to direct band-to-band transitions, while the involvement of surface defect states has been suggested to be responsible for the longer lifetime. The latter contribution can be reduced by addition of an inorganic shell around the core of the QD – the so-called “core-shell” QDs. The core and the shell are made from different semiconductors, such that the shell material has a larger band-gap. This treatment chemically passivates the surface defects of the QDs’ core, which reduces the involvement of the defects states in QDs’ de-excitation and increases the emission efficiency of the QDs. On average, the complete de-excitation of QDs in solution occurs within 10-100 ns [17], although this is significantly reduced when QDs are deposited onto solid substrates or incorporated into thin films. These timescales are significantly larger than the lifetimes of conventional fluorescent dyes (usually less than 5 ns, [17]), which can be advantageous for some technological applications.

The QDs used in this work were the as-prepared core-only Cadmium Telluride (CdTe) QDs and core-shell Cadmium Selenide/Zinc Sulphide (CdSe/ZnS) QDs that were synthesised in an organic solvent but later phase-transferred into aqueous solution and coated with a number of different ligands (cysteine and polyethylene glycol (PEG)-derived polymers).

1.2.3. Quantum Dots and Förster Resonance Energy Transfer

Extensive research is under way into the application of QDs in different areas of technology and medicine (more on this later). A considerable portion of these are based on the utilisation of QDs as donors of energy in Förster Resonance Energy Transfer (FRET).

FRET is a radiationless transfer of energy between an emitter (termed donor) in its excited state and an acceptor in its ground state, through long-range dipole-dipole interactions [18]. The rate of energy transfer (k_T) depends strongly on the donor-acceptor separation distance (r), as illustrated qualitatively in Figure 1.3(b):

$$k_T(r) = \frac{1}{\tau_D} \left(\frac{R_0}{r} \right)^6 \quad (1.1)$$

In this expression¹, τ_D is the fluorescence decay time of the donor in the absence of acceptor and R_0 is the Förster distance (or radius), defined as the donor-acceptor separation at which the FRET efficiency is 50% (Figure 1.3(b)). The Förster distance can be calculated from the material and spectral properties of the donor and acceptor using:

$$R_0^6 = 8.79 \times 10^{-5} (\kappa^2 n^{-4} Q_D J(\lambda)) \quad (1.2)$$

Here Q_D is the fluorescence quantum yield (QY) of donor, n is the refractive index of the medium. κ^2 is a factor that expresses the relative orientation of the transition dipoles of donor and acceptor in space; it is usually assumed to be equal to 2/3 [18]. The overlap integral ($J(\lambda)$) relates to the degree of spectral overlap between the donor emission and acceptor absorption bands and is defined mathematically as:

$$J(\lambda) = \int_0^{\infty} F_D(\lambda) \varepsilon_A(\lambda) \lambda^4 d\lambda \quad (1.3)$$

where $F_D(\lambda)$ is the fluorescence intensity of the donor in the range λ to $\lambda + \Delta\lambda$ with total intensity normalised to unity, and $\varepsilon_A(\lambda)$ is the extinction coefficient² of the acceptor at λ .

The FRET efficiency (E) is the percentage of the donor excitation events that result in energy transfer or, equivalently, acceptor activation (Figure 1.3):

$$E = \frac{k_T(r)}{\tau_D^{-1} + k_T(r) + \sum k_i} \quad (1.4)$$

where k_i are the rate constants of any de-excitation pathways other than radiative emission or energy transfer (Figure 1.3). If no such other pathways exist, this equation can be re-arranged to a simpler form that shows the dependency of E on the donor-acceptor separation distance:

$$E = \frac{R_0^6}{R_0^6 + r^6} \quad (1.5)$$

¹ It should be noted that the distance dependence of the energy transfer rate given in equation 1.1 is valid for two point dipoles. For entities of finite sizes, the equation is only valid if the separation distance between them is much larger than their size. In cases outside of these conditions, the transfer rates still follow a power-law dependence (with a smaller exponent). Therefore, equation 1.1 can be used to provide a qualitative explanation of the distance dependence of the FRET process for all cases.

² Equation 1.3 is only valid for acceptor samples with negligible scattering. For strongly-scattering samples, only the absorption contribution to the extinction coefficient should be used in the expression.

As can be seen from the definition of R_0 above (equation 1.2), the FRET efficiency is not only sensitive to acceptor-donor separation, but also depends on the spectral overlap between the donor emission and acceptor absorption bands, the emission QY of the donor and the relative orientation of donor's and acceptor's dipoles.

The advantage of using semiconductor QDs as donors in FRET pairs is that maximum spectral overlap can be achieved by selecting QDs with appropriate photoluminescence (PL) spectrum, thus ensuring maximum FRET efficiencies. The fact that their size is of the order of a typical Förster radius is also beneficial since it results in small donor-acceptor separation distances and hence high FRET efficiencies. Furthermore, QDs have wide absorption bands, which allows QDs to be excited at wavelengths where no direct excitation of the acceptor occurs [19]. While this is not crucial for technological applications, it does make the interpretation of the data more straightforward.

Experimentally, the energy transfer process in QDs-based system can be verified because it represents an additional de-excitation pathway. As a result, when QDs act as energy donors, their PL intensity is reduced – a process known as quenching – with an additional decrease of their average radiative lifetime [20]. A shift of the PL band is also expected due to the distribution of QDs sizes within a sample – the smaller or larger QDs will typically have better spectral overlap with the acceptors absorption band and hence they will transfer the energy more efficiently. In the case of a fluorescent acceptor, an increase of its emission intensity is also expected, which is sometimes accompanied by a lengthening of the lifetime [21] (despite the fact that, theoretically, the radiative behaviour of the acceptor is not expected to be affected by the energy transfer process).

It should be noted that, while in QD-based systems energy transfer is by far the most exploited interaction, these systems are by no means limited to it. For example, given favourable band alignment, charge transfer is also frequently observed. In fact, both energy and charge transfer can occur simultaneously in a complementary manner, which is often exploited in QD-based solar cells [21-25]. Spectroscopically, the two processes can in some cases be separated: charge transfer does not necessarily result in the enhancement of the acceptor's emission and in some cases it is actually quenches it [21, 26]. Also, the acceptor lifetime decreases in the case of charge transfer and remains unchanged or increases when energy transfer occurs.

1.2.4. Advantages of Quantum Dots over fluorescent dyes

As discussed above, the tunability of QDs' emission spectra is of great importance for their use in FRET-based applications. However, by far the strongest impact of the discovery of semiconductor QDs have been in the field of bio-imaging, previously dominated by fluorescent organic dyes. This is due to the many advantageous properties that QDs possess, in particular:

- The molar extinction coefficients of QDs can be much larger than those of organic chromophores, reaching values of up to $1,000,000 M^{-1}cm^{-1}$ for the largest QDs [27], compared to maximum values of $\sim 300,000 M^{-1}cm^{-1}$ for organic dyes [28, 29]. This is particularly significant in the near infra-red (NIR) region of the spectrum where, unlike organic dyes, QDs can have fairly large two-photon absorption cross-sections [30-32]. Furthermore, the fluorescence QYs of QDs are comparable to those of organic dyes in the visible region of the spectrum, and are significantly larger in the NIR [17]. As a result, QDs are generally considered to be **brighter** than organic fluorophores¹.
- QDs have **superior photo- and thermal stabilities** [17], especially when an NIR-emitting fluorophore is required [33]. This makes them better suited for applications that require imaging at high laser intensities or over long periods of time [34-37].
- Their relatively **long fluorescence lifetimes** [38, 39] allow easy temporal discrimination between the signal and the autofluorescence of cellular components as well as scattered excitation light, thus improving the sensitivity of the imaging technique.
- The presence of stabilising molecules on QDs' surfaces allows **straightforward modification of their surface chemistry** without adverse changes of their basic optical properties, such as the position and shape of absorption and emission spectra [40, 41]. In contrast, the chemical structure of organic dyes is the key factor determining their optical properties. Therefore, fine-tuning of their chemical properties, such as solubility and specificity, typically requires an in-depth knowledge of their structure-property relationship and complicated design strategies [17].

In addition to the above, several of QDs' properties are beneficial for multi-fluorophore applications, including their **large absorption bands** with increasing extinction coefficients towards the higher-energy end of the spectrum, their relatively **narrow and symmetric PL bands** and the large spectral separations between their absorption and emission maxima, i.e. **large Stokes' shifts**:

¹ Here, brightness is defined as the product of absorption coefficient and fluorescence quantum yield.

- The wide absorption bands allow excitation of several QD samples at a single wavelength – thus, a single light source is required for the simultaneous detection of several QD-labelled analytes. On the contrary, the narrow absorption bands of the organic dyes impose the use of multiple light sources.
- The narrow and symmetric PL bands of QDs facilitate deconvolution of the measured signal into individual contributions from QDs of different colours – a technique known as spectral multiplexing [42-44].
- Finally, small Stoke's shifts favour cross-talk between different fluorophores and reduce the spectral detection windows [17, 19]. QDs have large Stokes' shifts, owing to the strong exchange splitting of the excitonic states [45, 46], and so they are the ideal candidates for multi-fluorophore applications.

1.3. Nanobiotechnology research and Quantum Dots

The unification of nanotechnology with biosciences has great potential to deliver breakthrough discoveries in the near future. This is reflected in the great variety of topics that are already being addressed, despite the fact that the field of nanobiotechnology is still in its infancy. The main research directions are still being defined, but most can be attributed to one of the five main branches.

Firstly, the **use of biomaterials as templates** for assembly of nanostructures has seen a significant rise over the last decade, facilitated both by the advances in NP conjugation techniques and the ever-expanding knowledge of biological systems. To date, S-layers, DNA, peptides, proteins, viruses and microorganisms have all been utilised to produce ordered nano-structures [47-54].

Secondly, extensive nanotechnology research into the **nanoscale control of surface properties** is now being **applied to bio-related systems**, such as medical implants and stents [55-60], microfluidic devices [61-63], cantilever array sensors [64], and also for immobilisation of proteins and cells on substrates [65-67].

Bio-production and patterning of nanostructures is another fascinating topic that involves the production of plasmonic and magnetic nanoparticles by bacterial, microbial and biocatalytic growth [68-73].

Finally, the last two topics – nanoanalytics and nanomedicine – deal with the utilisation of nanomaterials in medicinal and analytics applications respectively. In **nanoanalytics**, the bioconjugated or biofunctionalised NPs and NCs are employed for cell imaging and analysis of structures (e.g. DNA, proteins) via microscopic and spectroscopic means [42, 74-84]. **Nanomedicine**, on the other hand, involves the use of NPs for diagnostic imaging, as contrast agents (e.g. for MRI) and as nano-carriers for delivery of therapeutic and imaging agents [85-94]. Both of these fields have received the most attention up to date due to their potential impact on the quality and efficacy of the available healthcare. These are also the areas in which the use of QDs features prominently. In fact, due to the several advantages of QDs over the conventional organic dyes (see above), most of the proposed practical applications of QDs have been in these fields.

QDs have so far been employed as diagnostic and therapeutic agents and as contrast material for advanced molecular, cellular and tissue imaging. Tumour targeting and imaging in live

animals [95-99], specific labelling of tissues *in vivo* and *in vitro* [39, 95, 100], real-time tracking of embryonic development [101], multiplexed nucleic acid detection [77, 102], monitoring of DNA replication and telomerisation [103], *in vitro* assay detection of proteins and analytes [43, 104, 105], deep-tissue imaging of vasculatures [30], *in vivo* tracking of cancer cells during metastasis [96, 106, 107], lymph node mapping [108] and subcellular resolution imaging of a mouse brain [109] have all been achieved, whilst many more applications have been proposed and are currently under investigation (e.g. gene profiling and high throughput drug and disease screening [110], super-resolution analysis and imaging of tissue sections [111]).

Despite great advances in the abovementioned categories, there remains one largely unexplored area of nanobiotechnology: the development of nano-bio hybrid materials that exploit the unique properties of nanomaterials to enhance the functionalities of technologically-promising biomaterials. The aim of this thesis was to address this issue and to demonstrate the potential of QDs/biomolecule integration for the development of materials for a variety of applications, ranging from light-harvesting to optical communications. This approach is rarely explored in the literature, with the majority of reports appearing in the last few years [112-117]. As such, this thesis represents a significant contribution to nanobiotechnology and materials research.

References

1. Brotsudarmo, T.H.P., et al., Peridinin-chlorophyll-protein reconstituted with chlorophyll mixtures: Preparation, bulk and single molecule spectroscopy. *FEBS Lett.* **580**, 5257-5262 (2006)
2. Miller, D., et al., Reconstitution of the Peridinin–chlorophyll a Protein (PCP): Evidence for Functional Flexibility in Chlorophyll Binding. *Photosynth. Res.* **86**, 229-240 (2005)
3. Oesterhelt, D. and L. Schuhmann, Reconstitution of bacteriorhodopsin. *FEBS Lett.* **44**, 262-265 (1974)
4. Racker, E. and W. Stoeckenius, Reconstitution of Purple Membrane Vesicles Catalyzing Light-driven Proton Uptake and Adenosine Triphosphate Formation. *J. Biol. Chem.* **249**, 662-663 (1974)
5. Ritchie, T.K., et al., Reconstitution of Membrane Proteins in Phospholipid Bilayer Nanodiscs, in *Methods in Enzymology* (Eds.: D. Nejat). pp. 211-231. Academic Press (2009)
6. Sizer, P.J.H., A. Miller, and A. Watts, Functional reconstitution of the integral membrane proteins of influenza virus into phospholipid liposomes. *Biochem.* **26**, 5106-5113 (1987)
7. Darveau, R.P., et al., Purification and reconstitution in lipid bilayer membranes of an outer membrane, pore-forming protein of *Aeromonas salmonicida*. *J. Bacteriol.* **156**, 1006-1011 (1983)
8. Drmanac, R., et al., DNA sequence determination by hybridization: a strategy for efficient large-scale sequencing. *Science* **260**, 1649-1652 (1993)
9. Bräuchle, C., N. Hampp, and D. Oesterhelt, Optical Applications of Bacteriorhodopsin and its mutated variants. *Adv. Mat.* **3**, 420-428 (1991)
10. Haarer, D., How to tailor molecular electronics or why is nature taking the ‘soft’ approach. *Adv. Mater.* **1**, 362-365 (1989)
11. Birge, R.R., et al., Biomolecular electronics: protein-based associative processors and volumetric memories. *J. Phys. Chem. B* **103**, 10746-10766 (1999)
12. Rothschild, L.J. and R.L. Mancinelli, Life in extreme environments. *Nature* **409**, 1092-1101 (2001)
13. Rogach, A.L., ed. *Semiconductor Nanocrystal Quantum Dots: Synthesis, Assembly, Spectroscopy and Applications*. 1 ed. Springer, Wien, (2008)
14. Nouailhat, A., Frontmatter, in *An Introduction to Nanoscience and Nanotechnology* (Eds.: A. Nouailhat). pp. i-xix. ISTE (Wiley) (2010)
15. Prasad, P.N., Quantum-Confined Materials, in *Nanophotonics* (Eds.: P.N. Prasad). pp. 79-127. John Wiley & Sons, Inc., Hoboken, NJ, USA (2004)
16. Cardona, M. and P.Y. Yu, eds. *Fundamentals of Semiconductors*. 4 ed. Springer, Berlin, (2010)
17. Resch-Genger, U., et al., Quantum dots versus organic dyes as fluorescent labels. *Nat. Meth.* **5**, 763-775 (2008)
18. Lakowicz, J.R., Energy Transfer, in *Principles of Fluorescence Spectroscopy* (Eds.: J.R. Lakowicz). pp. 443-475. Springer, New York (2006)
19. Prasad, P.N., Nanophotonics for Biotechnology and Nanomedicine, in *Nanophotonics* (Eds.: P.N. Prasad). pp. 355-379. John Wiley & Sons, Inc., New Jersey (2004)
20. Clapp, A.R., I.L. Medintz, and H. Mattoussi, Forster resonance energy transfer investigations using quantum-dot fluorophores. *Chemphyschem.* **7**, 47-57 (2006)
21. Giménez, S., et al., Energy transfer versus charge separation in hybrid systems of semiconductor quantum dots and Ru-dyes as potential co-sensitizers of TiO₂-based solar cells. *J. Appl. Phys.* **110**, 014314 (2011)
22. Sharma, S.N., Z.S. Pillai, and P.V. Kamat, Photoinduced Charge Transfer between CdSe Quantum Dots and p-Phenylenediamine. *J. Phys. Chem. B* **107**, 10088-10093 (2003)

23. Martinez-Ferrero, E., et al., Charge transfer kinetics in CdSe quantum dot sensitized solar cells. *Phys. Chem. Chem. Phys.* **12**, 2819-2821 (2010)
24. Buhbut, S., et al., Built-in Quantum Dot Antennas in Dye-Sensitized Solar Cells. *ACS Nano* **4**, 1293-1298 (2010)
25. Xu, Z. and M. Cotlet, Quantum Dot–Bridge–Fullerene Heterodimers with Controlled Photoinduced Electron Transfer. *Angew. Chem. Int. Ed.* **50**, 6079-6083 (2011)
26. Rakovich, A., et al., CdTe Quantum Dot/Dye Hybrid System as Photosensitizer for Photodynamic Therapy. *Nanoscale Res. Lett.* **5**, 753 - 760 (2010)
27. Yu, W.W., et al., Experimental determination of the extinction coefficient of CdTe, CdSe, and CdS nanocrystals. *Chem. Mater.* **15**, 2854-2860 (2003)
28. Berlier, J.E., et al., Quantitative Comparison of Long-wavelength Alexa Fluor Dyes to Cy Dyes: Fluorescence of the Dyes and Their Bioconjugates. *J. Histochem. Cytochem.* **51**, 1699-1712 (2003)
29. Leong, H.S., et al., Intravital imaging of embryonic and tumor neovasculature using viral nanoparticles. *Nat. Protoc.* **5**, 1406-1417 (2010)
30. Larson, D.R., et al., Water-soluble quantum dots for multiphoton fluorescence imaging in vivo. *Science* **300**, 1434-1436 (2003)
31. Padilha, L.A., et al., Frequency degenerate and nondegenerate two-photon absorption spectra of semiconductor quantum dots. *Phys. Rev. B* **75**, 075325 (2007)
32. Clapp, A.R., et al., Two-Photon Excitation of Quantum-Dot-Based Fluorescence Resonance Energy Transfer and Its Applications. *Adv. Mater.* **19**, 1921-1926 (2007)
33. Amiot, C., et al., Near-Infrared Fluorescent Materials for Sensing of Biological Targets. *Sensors* **8**, 3082-3105 (2008)
34. Mason, J.N., et al., Novel fluorescence-based approaches for the study of biogenic amine transporter localization, activity, and regulation. *J. Neurosci. Methods* **143**, 3-25 (2005)
35. Riegler, J., et al., Visualizing the self-assembly of tubulin with luminescent nanorods. *J. Nanosci. Nanotechnol.* **3**, 380-385 (2003)
36. Smith, A.M., et al., Multicolor quantum dots for molecular diagnostics of cancer. *Expert Rev. Mol. Diagn.* **6**, 231-244 (2006)
37. Sukhanova, A., et al., Biocompatible fluorescent nanocrystals for immunolabeling of membrane proteins and cells. *Anal. Biochem.* **324**, 60-67 (2004)
38. Schlegel, G., et al., Fluorescence decay time of single semiconductor nanocrystals. *Phys. Rev. Lett.* **88**, 137401-137405 (2002)
39. Dahan, M., et al., Time-gated biological imaging by use of colloidal quantum dots. *Opt. Lett.* **26**, 825-827 (2001)
40. Smith, A.M., et al., A systematic examination of surface coatings on the optical and chemical properties of semiconductor quantum dots. *Phys. Chem. Chem. Phys.* **8**, 3895-3903 (2006)
41. Wang, Q., et al., A Facile One-Step in situ Functionalization of Quantum Dots with Preserved Photoluminescence for Bioconjugation. *J. Am. Chem. Soc.* **129**, 6380-6381 (2007)
42. Medintz, I.L., et al., Quantum dot bioconjugates for imaging, labelling and sensing. *Nat. Mater.* **4**, 435-446 (2005)
43. Goldman, E.R., et al., Multiplexed toxin analysis using four colors of quantum dot fluororeagents. *Anal. Chem.* **76**, 684-688 (2004)

44. Jaiswal, J.K., et al., Long-term multiple color imaging of live cells using quantum dot bioconjugates. *Nat. Biotechnol.* **21**, 47-51 (2003)
45. Bagga, A., P.K. Chattopadhyay, and S. Ghosh, The Origin of Stokes Shift in Semiconductor Quantum Dots. *arXiv:cond-mat/0503612v19* (2005)
46. Bagga, A., P.K. Chattopadhyay, and S. Ghosh, Origin of Stokes shift in InAs and CdSe quantum dots: Exchange splitting of excitonic states. *Phys. Rev. B* **74**, 035341 (2006)
47. Erika, G., et al., Formation of Nanoparticle Arrays on S-Layer Protein Lattices. *J. Nanosci. Nanotechnol.* **4**, 115-120 (2004)
48. Pum, D. and U.B. Sleytr, The application of bacterial S-layers in molecular nanotechnology. *Trends Biotechnol.* **17**, 8-12 (1999)
49. Mertig, M. and W. Pompe, Biomimetic Fabrication of DNA-Based Metallic Nanowires and Networks, in *Nanobiotechnology* (Eds.: C.A. Mirkin and C.M. Niemeyer). pp. 256-277. Wiley-VCH Verlag GmbH & Co. KGaA (2005)
50. Nguyen, K., S. Campidelli, and A. Filoramo, DNA-Templated Pd Conductive Metallic Nanowires, in *DNA Nanotechnology: Methods and Protocols* (Eds.: G. Zuccheri and B. Samori). pp. 49-59. Springer, New York Heidelberg London Dordrecht (2011)
51. Dong, L.Q., et al., DNA-templated semiconductor nanoparticle chains and wires. *Adv. Mater.* **19**, 1748-1751 (2007)
52. Ryadnov, M.G. and D.N. Woolfson, Self-Assembling Nanostructures from Coiled-Coil Peptides, in *Nanobiotechnology II* (Eds.: C.A. Mirkin and C.M. Niemeyer). pp. 17-38. Wiley-VCH Verlag GmbH & Co. KGaA, Weinheim (2007)
53. Dujardin, E. and S. Mann, Synthesis and Assembly of Nanoparticles and Nanostructures Using Bio-Derived Templates, in *Nanobiotechnology II* (Eds.: C.A. Mirkin and C.M. Niemeyer). pp. 39-63. Wiley-VCH Verlag GmbH & Co. KGaA, Weinheim (2007)
54. Rajagopal, K. and J.P. Schneider, Self-assembling peptides and proteins for nanotechnological applications. *Curr. Opin. Struct. Biol.* **14**, 480-486 (2004)
55. Giavaresi, G., et al., Histomorphometric, ultrastructural and microhardness evaluation of the osseointegration of a nanostructured titanium oxide coating by metal-organic chemical vapour deposition: an in vivo study. *Biomaterials* **25**, 5583-5591 (2004)
56. Shane, A.C., et al., Nanostructured Ceramics for Biomedical Implants. *J. Nanosci. Nanotechnol.* **2**, 293-312 (2002)
57. Chen, F., et al., Biocompatibility of electrophoretical deposition of nanostructured hydroxyapatite coating on roughen titanium surface: In vitro evaluation using mesenchymal stem cells. *J. Biomed. Mater. Res. A* **82B**, 183-191 (2007)
58. Shtansky, D.V., et al., Multifunctional biocompatible nanostructured coatings for load-bearing implants. *Surf. Coat. Tech.* **201**, 4111-4118 (2006)
59. Variola, F., et al., Improving Biocompatibility of Implantable Metals by Nanoscale Modification of Surfaces: An Overview of Strategies, Fabrication Methods, and Challenges. *Small* **5**, 996-1006 (2009)
60. Pareta, R.A., et al., Increased endothelial cell adhesion on plasma modified nanostructured polymeric and metallic surfaces for vascular stent applications. *Biotechnol. Bioeng.* **103**, 459-471 (2009)

61. Bartos, H., F. Goetz, and R.-P. Peters, Microfluidics Meets Nano: Lab-on-a-Chip Devices and their Potential for Nanobiotechnology, in *Nanobiotechnology* (Eds.: C.A. Mirkin and C.M. Niemeyer). pp. 13-30. Wiley-VCH Verlag GmbH & Co. KGaA, Weinheim (2005)
62. Cao, H., et al., Gradient nanostructures for interfacing microfluidics and nanofluidics. *Appl. Phys. Lett.* **81**, 3058-3061 (2002)
63. Krupenkin, T.N., et al., From Rolling Ball to Complete Wetting: The Dynamic Tuning of Liquids on Nanostructured Surfaces. *Langmuir* **20**, 3824-3827 (2004)
64. Lang, H.P., M. Hegner, and C. Gerber, Cantilever array sensors. *Mater. Today* **8**, 30-36 (2005)
65. Mao, H., T. Yang, and P.S. Cremer, Design and Characterization of Immobilized Enzymes in Microfluidic Systems. *Anal. Chem.* **74**, 379-385 (2001)
66. Freire, S.L.S. and A.R. Wheeler, Proteome-on-a-chip: Mirage, or on the horizon? *Lab Chip* **6**, 1415-1423 (2006)
67. Vega, R.A., et al., Bionanoarrays, in *Nanobiotechnology II* (Eds.: C.A. Mirkin and C.M. Niemeyer). pp. 233-259. Wiley-VCH Verlag GmbH & Co. KGaA, Weinheim (2007)
68. Sastry, M., et al., Biosynthesis of metal nanoparticles using fungi and actinomycete. *Curr. Sci.* **85**, 162-170 (2003)
69. Gericke, M. and A. Pinches, Biological synthesis of metal nanoparticles. *Hydrometallurgy* **83**, 132-140 (2006)
70. Mandal, D., et al., The use of microorganisms for the formation of metal nanoparticles and their application. *Appl. Microbiol. Biotechnol.* **69**, 485-492 (2006)
71. Klaus, T., et al., Silver-based crystalline nanoparticles, microbially fabricated. *Proc. Natl. Acad. Sci.* **96**, 13611-13614 (1999)
72. Zayats, M., et al., Biocatalytic Growth of Au Nanoparticles: From Mechanistic Aspects to Biosensors Design. *Nano Lett.* **5**, 21-25 (2004)
73. Lee, H., et al., Controlled Assembly of Magnetic Nanoparticles from Magnetotactic Bacteria Using Microelectromagnets Arrays. *Nano Lett.* **4**, 995-998 (2004)
74. Wang, J., Nanoparticles for Electrochemical Bioassays, in *Nanobiotechnology II* (Eds.: C.A. Mirkin and C.M. Niemeyer). pp. 123-140. Wiley-VCH Verlag GmbH & Co. KGaA, Weinheim (2007)
75. Rosi, N.L. and C.A. Mirkin, Nanostructures in Biodiagnostics. *Chem. Rev.* **105**, 1547-1562 (2005)
76. Taton, T.A., C.A. Mirkin, and R.L. Letsinger, Scanometric DNA Array Detection with Nanoparticle Probes. *Science* **289**, 1757-1760 (2000)
77. Han, M.Y., et al., Quantum-dot-tagged microbeads for multiplexed optical coding of biomolecules. *Nat. Biotechnol.* **19**, 631-635 (2001)
78. Palecek, E., M. Fojta, and F. Jelen, New approaches in the development of DNA sensors: hybridization and electrochemical detection of DNA and RNA at two different surfaces. *Bioelectrochemistry* **56**, 85-90 (2002)
79. Pons, T., et al., Luminescent Semiconductor Quantum Dots in Biology, in *Nanobiotechnology II* (Eds.: C.A. Mirkin and C.M. Niemeyer). pp. 141-157. Wiley-VCH Verlag GmbH & Co. KGaA, Weinheim (2007)
80. Goldman, E.R., et al., Conjugation of luminescent quantum dots with antibodies using an engineered adaptor protein to provide new reagents for fluoroimmunoassays. *Anal. Chem.* **74**, 841-847 (2002)
81. So, M.-K., et al., Self-illuminating quantum dot conjugates for in vivo imaging. *Nat. Biotech.* **24**, 339-343 (2006)
82. Willets, K.A., et al., Nanoscale Localized Surface Plasmon Resonance Biosensors, in *Nanobiotechnology II* (Eds.: C.A. Mirkin and C.M. Niemeyer). pp. 159-173. Wiley-VCH Verlag GmbH & Co. KGaA, Weinheim (2007)

83. McFarland, A.D. and R.P. Van Duyne, Single Silver Nanoparticles as Real-Time Optical Sensors with Zeptomole Sensitivity. *Nano Lett.* **3**, 1057-1062 (2003)
84. Haes, A.J. and R.P. Van Duyne, A unified view of propagating and localized surface plasmon resonance biosensors. *Anal. Bioanal. Chem.* **379**, 920-930 (2004)
85. Juliano, R., Biological Barriers to Nanocarrier-Mediated Delivery of Therapeutic and Imaging Agents, in *Nanobiotechnology II* (Eds.: C.A. Mirkin and C.M. Niemeyer). pp. 261-284. Wiley-VCH Verlag GmbH & Co. KGaA, Weinheim (2007)
86. Sahoo, S.K. and V. Labhasetwar, Nanotech approaches to drug delivery and imaging. *Drug Discov. Today* **8**, 1112-1120 (2003)
87. LaVan, D.A., T. McGuire, and R. Langer, Small-scale systems for in vivo drug delivery. *Nat. Biotech.* **21**, 1184-1191 (2003)
88. Fukumori, Y. and H. Ichikawa, Nanoparticles for cancer therapy and diagnosis. *Adv. Powder Technol.* **17**, 1-28 (2006)
89. Euliss, L.E., J.A. DuPont, and J.M. DeSimone, Organic Nanoparticles: Adapting Emerging Techniques from the Electronics Industry for the Generation of Shape-Specific, Functionalized Carriers for Applications in Nanomedicine, in *Nanobiotechnology II* (Eds.: C.A. Mirkin and C.M. Niemeyer). pp. 285-303. Wiley-VCH Verlag GmbH & Co. KGaA, Weinheim (2007)
90. Torchilin, V.P., Recent advances with liposomes as pharmaceutical carriers. *Nat. Rev. Drug Discov.* **4**, 145-160 (2005)
91. Bulte, J.W.M. and D.L. Kraitchman, Iron oxide MR contrast agents for molecular and cellular imaging. *NMR Biomed.* **17**, 484-499 (2004)
92. Jun, Y.-W., J.-H. Lee, and J. Cheon, Nanoparticle Contrast Agents for Molecular Magnetic Resonance Imaging, in *Nanobiotechnology II* (Eds.: C.A. Mirkin and C.M. Niemeyer). pp. 321-346. Wiley-VCH Verlag GmbH & Co. KGaA, Weinheim (2007)
93. Jun, Y.-w., et al., Nanoscale Size Effect of Magnetic Nanocrystals and Their Utilization for Cancer Diagnosis via Magnetic Resonance Imaging. *J. Am. Chem. Soc.* **127**, 5732-5733 (2005)
94. Hahn, P.F., et al., First clinical trial of a new superparamagnetic iron oxide for use as an oral gastrointestinal contrast agent in MR imaging. *Radiology* **175**, 695-700 (1990)
95. Akerman, M.E., et al., Nanocrystal targeting in vivo. *Proc. Natl. Acad. Sci. USA* **99**, 12617-12621 (2002)
96. Gao, X.H., et al., In vivo cancer targeting and imaging with semiconductor quantum dots. *Nat. Biotechnol.* **22**, 969-976 (2004)
97. So, M.K., et al., Creating self-illuminating quantum dot conjugates. *Nat. Protoc.* **1**, 1160-1164 (2006)
98. Klostranec, J.M. and W.C.W. Chan, Quantum dots in biological and biomedical research: Recent progress and present challenges. *Adv. Mater.* **18**, 1953-1964 (2006)
99. Josephson, L., et al., Near-Infrared Fluorescent Nanoparticles as Combined MR/Optical Imaging Probes. *Bioconjug. Chem.* **13**, 554-560 (2002)
100. Jaiswal, J.K. and S.M. Simon, Potentials and pitfalls of fluorescent quantum dots for biological imaging. *Trends Cell. Biol.* **14**, 497-504 (2004)
101. Dubertret, B., et al., In Vivo Imaging of Quantum Dots Encapsulated in Phospholipid Micelles. *Science* **298**, 1759-1762 (2002)

102. Xu, H.X., et al., Multiplexed SNP genotyping using the Qbead (TM) system: a quantum dot-encoded microsphere-based assay. *Nucleic Acids Res.* **31**, E43 (2003)
103. Patolsky, F., et al., Lighting-Up the Dynamics of Telomerization and DNA Replication by CdSe-ZnS Quantum Dots. *J. Am. Chem. Soc.* **125**, 13918-13919 (2003)
104. Chan, W.C.W. and S.M. Nie, Quantum dot bioconjugates for ultrasensitive nonisotopic detection. *Science* **281**, 2016-2018 (1998)
105. Xiao, Y. and P.E. Barker, Semiconductor nanocrystal probes for human metaphase chromosomes. *Nucleic Acids Res.* **32**, E28 (2004)
106. Hoshino, A., et al., Applications of T-lymphoma labeled with fluorescent quantum dots to cell tracing markers in mouse body. *Biochem. Bioph. Res. Co.* **314**, 46-53 (2004)
107. Voura, E.B., et al., Tracking metastatic tumor cell extravasation with quantum dot nanocrystals and fluorescence emission-scanning microscopy. *Nat. Med.* **10**, 993-998 (2004)
108. Kim, S., et al., Near-infrared fluorescent type II quantum dots for sentinel lymph node mapping. *Nat. Biotech.* **22**, 93-97 (2004)
109. Levene, M.J., et al., In Vivo Multiphoton Microscopy of Deep Brain Tissue. *J. Neurophys.* **91**, 1908-1912 (2004)
110. Chan, W.C.W., et al., Luminescent quantum dots for multiplexed biological detection and imaging. *Curr. Opin. Biotech.* **13**, 40-46 (2002)
111. Lidke, K., et al., Superresolution by localization of quantum dots using blinking statistics. *Opt. Express* **13**, 7052-7062 (2005)
112. Griep, M., et al., Integration of Optical Protein and Quantum Dot Films for Biosensing. *Proc. IEEE Conf. NANO '08* 657-659 (2008)
113. Griep, M.H., et al., Quantum dot enhancement of bacteriorhodopsin-based electrodes. *Biosens. Bioelectron.* **25**, 1493-1497 (2010)
114. Li, R., et al., Stationary current generated from photocycle of a hybrid bacteriorhodopsin/quantum dot bionanosystem. *Appl. Phys. Lett.* **91**, 223901 (2007)
115. Li, R., et al., Enhancement of photoelectric response of bacteriorhodopsin by multilayered WO₃ x H₂O nanocrystals/PVA membrane. *Chem. Commun.* **46**, 689-91 (2010)
116. Nabiev, I., et al., Fluorescent Quantum Dots as Artificial Antennas for Enhanced Light Harvesting and Energy Transfer to Photosynthetic Reaction Centers. *Angew. Chem. Int. Edit.* **49**, 7217-7221 (2010)
117. Rakovich, A., et al., Resonance Energy Transfer Improves the Biological Function of Bacteriorhodopsin within a Hybrid Material Built from Purple Membranes and Semiconductor Quantum Dots. *Nano Lett.* **10**, 2640-2648 (2010)

2. MATERIALS AND METHODS

This thesis deals with three widely different systems, each of which involved use of different materials and techniques. These materials and techniques are described in later chapters. This chapter deals with the materials and methods that were common to most systems. In particular, this chapter starts by describing the synthesis and characterization of semiconductor quantum dots, since all of the systems contained them as one of the components. This is followed by a discussion of several spectroscopic techniques, with an emphasis on the parameters and conclusions derived from each technique. Finally, protocols and instrumentation for some other experimental methods are presented.

2.1. Quantum Dots preparation and characterization

Two types of quantum dots were used in the work described in this thesis: CdTe and CdSe/ZnS. Because CdSe/ZnS QDs are core-shell in structure, they tend to be of larger diameters when compared to CdTe QDs. Smaller diameters are beneficial for FRET-based applications, so CdTe QDs have an advantage over CdSe QDs in that respect. On the other hand, the surface chemistry of CdSe QDs can easily be changed, while that of CdTe QDs is not very flexible. This ability presents opportunity to change the surface charge of QDs and make them more bio-compatible (i.e. non-toxic). In addition, CdSe/ZnS QDs tend to be more stable when compared to CdTe QDs due to both the core-shell structure and the thicker ligand (stabiliser) shell. Below is a short description of the two types of QDs used, including a synopsis of the synthesis methods and the pre-measurement characterisation of QDs.

2.1.1. Cadmium Telluride Quantum Dots

CdTe QDs are cadmium telluride nanocrystals of 3 – 6 nm in diameter. These nanocrystals are kept in solution by thioglycolic acid (TGA) molecules attached to the surface of the nanocrystals through the sulphur atom to surface cadmium atom bond. Each TGA molecule has a net negative charge, resulting in an overall negatively charged surface of the CdTe QDs.

QDs of this type were synthesised using an aqueous method developed by Rogach *et al.* [1] (Figure 2.1). Typically, this method involves a reaction between a cadmium salt and telluride extracted from the precursor. In particular, a cadmium salt (e.g. $\text{Cd}(\text{ClO}_4)_2 \cdot 6\text{H}_2\text{O}$) is dissolved in water and a stabiliser is added to this solution. The pH of the solution is adjusted with 1 M NaOH and is transferred to a round-bottom flask fitted with a septum and valves. This is then deaerated by N_2 gas for approximately 30 minutes, after which Te precursor (typically Al_2Te_3) is

reacted with acid (H_2SO_4) to produce H_2Te gas which is carried by the nitrogen flow to the reaction flask containing cadmium salt and stabilizer. This causes nucleation/seeding of CdTe nanocrystals. These are then grown to desired size through application of heat. The growth is usually monitored by recording fluorescence spectra of small amounts taken from the flask. Upon completion of synthesis, the volume of the sample is reduced via rotary vacuum evaporator in order to increase the overall concentration of QDs.

Further optimisation of samples usually involves size-selective precipitation/re-dilution of QDs that separates the synthesised sample into fractions that have smaller size-distribution of QDs. Using this method, fractions of QDs that have larger diameters are obtained first, and fractions of smallest QDs are produced last. This is often advantageous as the middle fractions tend to have highest QYs. In addition, sample(s) may be aged – they are stored under direct sunlight for a period of time. This has been shown to increase the QY of CdTe QDs.

CdTe QDs used in this work were synthesised, optimised and supplied by Dr. Vladimir Lesnyak and Dr. Nikolai Gaponik.

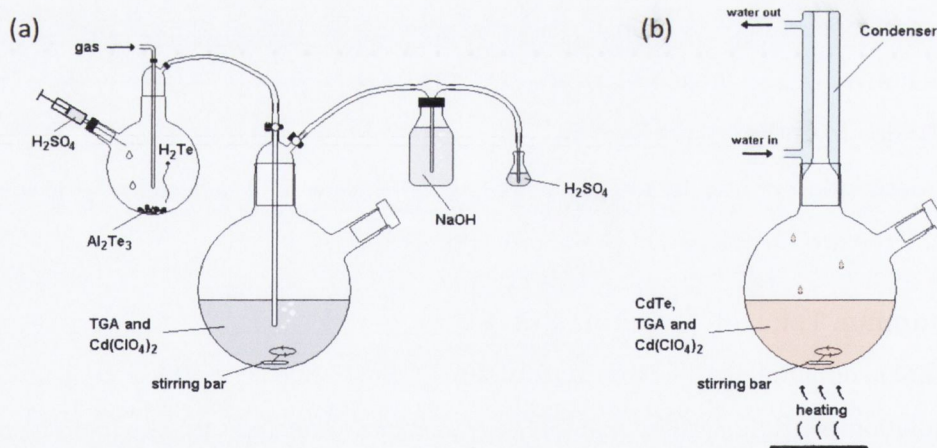


Figure 2.1| Aqueous synthesis of thiol-stabilised Cadmium Telluride quantum dots. (a) After purging of the thioglycolic acid (TGA) and cadmium precursor ($\text{Cd}(\text{ClO}_4)_2$) solution with nitrogen, hydrogen telluride gas is added to the nitrogen flow. Once in solution, hydrogen telluride reacts with cadmium perchlorate and in so doing seeding the CdTe nanocrystals. The nanocrystals are grown to desired size by refluxing **(b)** the solution, while monitoring the growth via photoluminescence measurements.

2.1.2. Cadmium Selenide/Zinc Sulphide Quantum Dots

CdSe/ZnS QDs are nanocrystals of a core-shell structure. The core is composed from Cadmium Selenide and it is covered by a thin shell of Zinc Sulphide. This results in a double-potential well

confinement of excitons, greatly improving their radiative recombination rate or, equivalently, their fluorescence quantum yield. The core diameter is typically 2-6 nm, while only a few monolayers of ZnS are required to improve the QY of QDs.

The CdSe/ZnS QDs were synthesised and functionalised by Dr. Alyona Sukhanova. These QDs were prepared according to a protocol adapted from Hines and Guyot-Sionnest [2]. In this method, the CdSe core is grown first by drying and degassing a solution containing trioctylphosphine oxide (TOPO) and hexadecylamine (HDA) under vacuum at 180 °C, and then heating it to 340 °C under argon flow in a reaction flask. Next, a solution containing elemental Selenium and dimethylcadmium in trioctylphosphine (TOP) is prepared and added to the flask by a fast injection (< 1 sec) using a syringe. This produces CdSe nanocrystals of approximately 2 nm diameter. The CdSe QDs are then grown to the desired size by refluxing the mixture at 280 °C. At this stage, QDs can be precipitated from solution cooled to 50-60 °C by addition of methanol to the solution, followed by repeated washing with methanol and drying. To grow the ZnS shell on top of the CdSe cores, the dried CdSe QDs are first re-dissolved in TOPO/HDA mixture and the purged with argon flow at 180 °C and heated to 220 °C or, alternatively, the CdSe QDs precipitation stage is skipped and replaced by a simple cooling of the reaction mixture to 220 °C. A solution of hexamethyldisilthiane and diethylzinc in TOP is added dropwise, followed by a slow cooling of the mixture containing the QDs to 60 °C. CdSe/ZnS QDs are then precipitated and washed with methanol and dried. QDs synthesised in this manner have CdSe core diameters of 2-6 nm and ZnS shell thickness of a few monolayers, with a narrow size distribution within a sample (< 5%) and a quantum yield of ~ 60% in an organic solvent at room temperature [3].

For experiments with biomolecules, the surface molecules of the QDs have to be changed in order to make QDs soluble in aqueous solvents. The simplest way to do this is to exchange the TOPO-TOP coating of CdSe/ZnS QDs by cysteine (Cys) molecules [4]. This is achieved by first dissolving the dried QDs in chloroform and adding a 10 mg/mL solution of DL-Cys in methanol. Upon this addition, the solution becomes cloudy and QDs can be extracted by centrifugation at 14,000 rpm followed by triple washing of precipitate with methanol. QDs extracted in this way are dried under vacuum and then re-dissolved in water, which is assisted by a drop-wise addition of 1 M NaOH and sonication. QDs are again extracted by centrifugation and re-dissolved in water. This QD solution is then dialyzed against pure water for 8 – 10 hours using the Spectra/Por® Float-A-Lyzer® Dialysis Tubes (Sigma), followed by centrifugation at 8,000 rpm for 10 minutes. The supernatant containing the QDs is removed from the tubes and finally filtrated through the 0.22 µm Ultrafree®-MC microcentrifuge filters (Sigma).

CdSe/ZnS QDs solubilised by Cys molecules in water are highly luminescent (QY>50%) [5], however their stability is considerably diminished. In order to improve the stability of QDs in aqueous solutions a further substitution of ligand molecules on QDs' surface can be performed. The preferred way is to replace the Cys molecules by a polymer shell consisting of PEG-derived polymer molecules. This ensures the biocompatibility of QDs [5]. In order to do this, a solution of PEG-derived polymer, for example ~50 mg/mL of PEG acid thiol (Polypure), is added to 1 mg/mL solution of cysteine solubilised QDs. Sample is incubated overnight at +4 °C and filtered by centrifugation in Amicon Ultra-15 filter units with 10 kDa cut-off (Millipore). Excess ligands are removed by gel exclusion chromatography through home-made Sephadex-25 (Sigma) column.

2.1.3. Initial characterisation of QDs samples

Preliminary characterisation of QD samples involved determination of their absorption (ABS) and PL peaks' positions, determination of the quantum yield (QY) of their emission, concentration of stock solution and their physical and hydrodynamic size.

The concentration and the average core diameter of QDs in the sample were determined according to Yu *et al.* [6]. First of all, the stock solution was diluted by approximately 50 times and its absorption spectrum was recorded. Based on the absorption value (A_{exc}) at the position of the excitonic peak (λ_{exc}), the concentration of this solution was adjusted to give A_{exc} between 0.15 and 0.25. The total dilution of the stock solution to achieve this was noted. Next, the PL spectrum of the diluted solution was recorded and the maximum (PL_{MAX}) and the FWHM (PL_{FWHM}) of the emission peak were determined (Figure 2.2). From that point on, the QD sample was usually referred to by its composition and PL_{MAX} , e.g. CdTe600.

The average core diameters of QDs in the sample (in *nm*) were calculated from λ_{exc} (also in *nm*) according to the following empirical equations [6]:

$$\text{CdTe: } D(\text{nm}) = (9.8127 \times 10^{-7})\lambda_{exc}^3 - (1.7147 \times 10^{-3})\lambda_{exc}^2 + (1.0064)\lambda_{exc} - (194.84) \quad (2.1)$$

$$\text{CdSe: } D = (1.6122 \times 10^{-9})\lambda_{exc}^4 - (2.6575 \times 10^{-4})\lambda_{exc}^3 + (1.6242 \times 10^{-3})\lambda_{exc}^2 - (0.4277)\lambda_{exc} + (41.57) \quad (2.2)$$

It is important to note that these diameters correspond to core diameters only. The actual physical size of the nanocrystals is always larger than this value. For CdTe QDs, which do not have an inorganic shell, the difference is the size of the stabilising molecules, so the physical diameter of TGA-stabilised CdTe QDs is ~1 nm larger than the core diameter as calculated

above. For CdSe/ZnS QDs, the thickness of the ZnS shell as well as the size of the ligand molecules must be accounted for.

The extinction coefficient of a QD sample can be calculated from the value of the average physical diameter (D , in nm) of QDs obtained in equation 2.1 or 2.2 and the transition energy (ΔE , in eV) corresponding to the first absorption peak [6] using another set of empirical equations:

$$\text{CdTe: } \varepsilon(M^{-1}cm^{-1}) = 3450 \Delta E D^{2.4} \quad (2.3)$$

$$\text{CdSe: } \varepsilon(M^{-1}cm^{-1}) = 1600 \Delta E D^3 \quad (2.4)$$

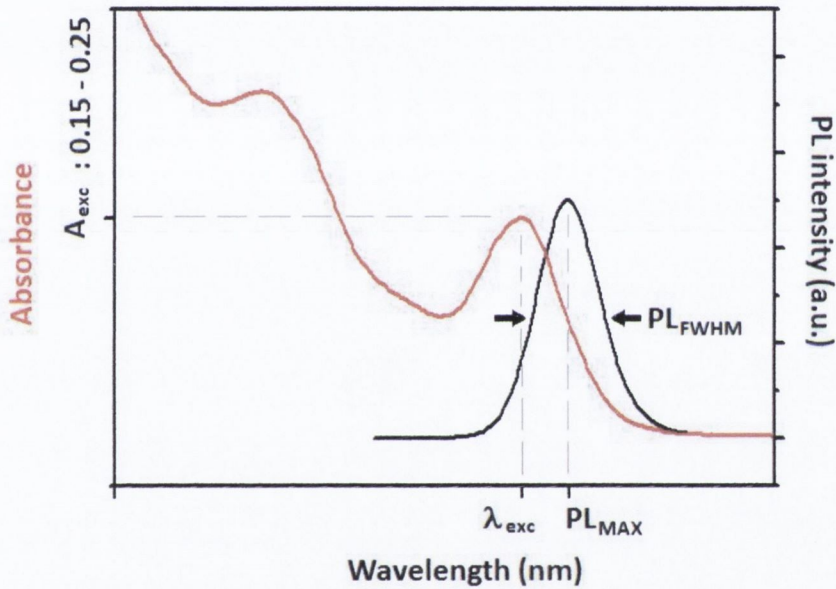


Figure 2.2| Preliminary spectroscopic characterisation of QDs. For each QD sample, the position of the excitonic peak (λ_{exc}) and the centre of the emission peak (PL_{MAX}) were determined. These values, together with the value of the FWHM of the emission peak (PL_{FWHM}), were then used to calculate the concentration of the QD stock. For accurate determination of the concentration, the absorbance at the excitonic peak was kept between 0.15 and 0.25, in accordance with [6].

Using the measured value of absorbance at the first excitonic peak (λ_{exc}) and the extinction coefficient as calculated above, the concentration of the diluted QD solution can be easily determined through the Beer-Lambert law ($A = \varepsilon CL$), with a small correction to account for the size distribution of QDs in the sample, determined by the value of the PL_{FWHM} :

$$C = \frac{A_{exc} \times (PL_{FWHM} / K)}{\varepsilon \times L} \quad (2.5)$$

Here, K is the correction constant which is equal to 29 and 25 for CdTe and CdSe QDs respectively.

The next step in the characterization of a QD sample was the determination of its QY (QY_{QD}) by comparing the intensity of its emission to that of a solution of a standard fluorophore of known QY (QY_{st}). The fluorophore was chosen so as to have emission over a similar wavelength range as the QD sample being analyzed. Both the QD sample and standard fluorophore were diluted until their absorption spectra intersected close to the absorption peak of the QDs, and the wavelength at which they intersected was used as the excitation wavelength when measuring the photoluminescence spectra of these two solutions. The QY of the QD sample was calculated by integrating the PL peaks of the QDs and the standard fluorophore and then comparing them according to the following equation:

$$QY_{QD} = \frac{PL_{int,QD}}{PL_{int,st}} QY_{st} \quad (2.6)$$

Finally, the average hydrodynamic size and the surface charge of QDs were determined by the dynamic light-scattering technique. These measurements are described in detail in section 2.3.

2.2. Spectroscopic measurements

The three model systems were studied using a variety of different techniques, some of which were common to all systems. The most important ones for initial characterization were absorption and photoluminescence spectroscopies. Further investigations usually involved the use of time-resolved fluorescence measurements. The experimental procedures, instrumentation and possible outcomes of these techniques are described in this section.

2.2.1. Steady-state spectroscopic measurements

Absorption Spectroscopy (UV-vis)

UV-vis spectroscopy was primarily used to determine the concentration of sample components using Beer-Lambert Law:

$$A(\lambda) = \varepsilon_{\lambda} \cdot C \cdot L \quad (2.7)$$

where A and ε_{λ} ($M^{-1} \text{ cm}^{-1}$) are sample absorbance and extinction coefficient at wavelength λ , usually at the absorbance peak. L is sample length in cm , and it corresponds to sample thickness for thin films and to the length of the cuvette cavity for liquids. C is the concentration of the sample in M (mol L^{-1}). Absorbance measurements were also useful in determining the molar ratio of components in a sample by deconvoluting the spectra of the hybrid sample into contributions from constituent components, as described below.

Varian Cary50Conc UV-visible spectrophotometer was used to record absorption spectra. Samples being analyzed were diluted until their concentration was of the order of $1 \mu\text{M}$ to avoid re-absorption effects.

Photoluminescence (PL) spectroscopy

Apart from the determination of QDs' QY, the most important application of PL measurements was to monitor the energy/charge transfer within the model system studied. As discussed previously, charge and energy transfer from donor to acceptor typically results in a decrease of donor's emission. An increase of acceptor's emission is expected for energy transfer, although this does not always occur. In the absence of any other mechanisms of fluorescence quenching, the efficiency of the energy transfer (E) is directly proportional to the relative decrease of PL intensity of the donor (PL_D) in the presence of acceptor (PL_{DA}):

$$E = 1 - \frac{PL_{DA}}{PL_D} \quad (2.8)$$

Steady-state PL measurements in the UV and visible wavelength ranges were carried out using a Varian CaryEclipse Fluorescence Spectrophotometer. Near-infrared (NIR) photoluminescence spectra were recorded on a FLS920 Fluorescence Spectrometer (Edinburgh Instruments) with a Hamamatsu R5509 NIR photomultiplier tube, which was cooled to -70°C and equilibrated at this temperature for at least 1 hour prior to measurements.

After the measurements, the raw PL data was corrected for inner filter and re-absorption effects, both of which can cause a decrease in emission intensity, unrelated to the quenching effects caused by charge or energy transfer [7]. The correction was achieved by introducing a correction factor k , such that

$$PL_{normalized,corrected} = k \frac{PL_{DA}}{PL_D} \quad (2.9)$$

Here PL_{DA} and PL_D are the PL intensities of a donor-acceptor (DA) mixture and a pure donor (D) solution respectively. The correction coefficient k was calculated according to the following equation:

$$k = \frac{(1 - 10^{-A_D^{exc}})(1 - 10^{-A_D^{emiss}})}{A_D^{exc} \cdot A_D^{emiss}} \frac{A_{DA}^{exc} \cdot A_{DA}^{emiss}}{(1 - 10^{-A_{DA}^{exc}})(1 - 10^{-A_{DA}^{emiss}})} \quad (2.10)$$

Where the absorbances of the DA and D solutions and those of donor-acceptor mixtures are defined as usual:

$$\begin{aligned} A_D^{exc} &= \varepsilon_D(\lambda_{exc}) \cdot C_D \cdot L \\ A_D^{emiss} &= \varepsilon_D(\lambda_{emiss}) \cdot C_D \cdot l \\ A_{DA}^{exc} &= [\varepsilon_D(\lambda_{exc}) \cdot C_D + \varepsilon_A(\lambda_{exc}) \cdot C_A] \cdot L \\ A_{DA}^{emiss} &= [\varepsilon_D(\lambda_{emiss}) \cdot C_D + \varepsilon_A(\lambda_{emiss}) \cdot C_A] \cdot l \end{aligned} \quad (2.11)$$

where ε_D and ε_A , and C_D and C_A are the extinction coefficients and concentrations of donor and acceptor solutions respectively. λ_{exc} is the excitation wavelength at which the PL spectrum was measured and λ_{emiss} is the wavelength at the PL peak.

Deconvolution of spectra into contributions from constituents

Due to the overlap of the spectral bands it was found that, in some cases, it is necessary to decompose a spectrum of the donor-acceptor mixture into contributions from the

constituents. In particular, it was found useful to determine the donor to acceptor molar ratio from the UV-vis measurements and also to evaluate the degree of quenching of donor's fluorescence and enhancement of acceptor's PL.

In order to achieve this, it was assumed that the spectrum of the DA solution ($I_{DA}(\lambda)$) can be represented as a linear sum of contributions from the donors ($I_D(\lambda)$) and acceptors ($I_A(\lambda)$):

$$I_{DA}(\lambda) = k_D \cdot I_D(\lambda) + k_A \cdot I_A(\lambda) + k_{BGR} \quad (2.12)$$

where k_D and k_A are the weighing coefficients and k_{BGR} is the background constant. The spectrum of the DA solution was fitted to this equation by least-squares analysis [8] using Matlab or by a linear regression analysis in Origin.

2.2.2. Time-resolved PL measurements

Fluorescence Lifetime Measurements

Fluorescence lifetime measurements are a very powerful tool for monitoring and determining the mechanisms of interactions between the different components. For example, changes in radiative lifetime provide a way to quantify the efficiency of energy transfer from donor to acceptor entities in a hybrid complex [9]:

$$E = 1 - \frac{\tau_{DA}}{\tau_D} \quad (2.13)$$

Fluorescence lifetimes are usually measured by Time-Correlated Single Photon Counting (TCSPC). This technique works on a single photon level [10], which is achieved by controlling both the concentration of the sample and the excitation intensity. The sample is excited by a pulsed laser, and the time delay between the excitation and the arrival of the emitted photon to the detector is measured. This is repeated over millions of cycles and the time delay for each emitted photon is recorded (Figure 2.3, panel A). The time delays are then binned into time intervals to build up a histogram that corresponds to the decay of the excited state of the fluorophore (Figure 2.3, panel B). The histogram is then fitted to a multiple-exponential equation using least-squares analysis to extract the values of the lifetimes:

$$I(t) = N \sum_i \alpha_i \exp\left(-\frac{t}{\tau_i}\right) \quad (2.14)$$

where N is the normalization constant, τ_i are the PL decay lifetimes and α_i are the corresponding weighing coefficients. In some cases, it is beneficial to calculate the intensity-averaged lifetime (τ_{av}):

$$\tau_{av} = \frac{\sum \alpha_i \tau_i^2}{\sum \alpha_i \tau_i} \quad (2.15)$$

In particular, the average lifetime is used to calculate the efficiency of the energy transfer from donors to acceptors (using equation 2.13).

Fluorescence decays were measured using PicoQuant MicroTime200 system (Figure 2.3, panel C) equipped with time-correlated single photon counters (Micro-Photon-Devices). Samples were excited with 480 nm pulses of ~50 ps duration generated by a LDH-480 or LDH-P-C-405B diode laser, controlled by a PDL-800B driver. The frequency was adjusted between 20 and 80 MHz to accommodate the time window over which the fluorescence decays fully, while providing maximum resolution. The time response of the whole system was ~100 ps. Data were fitted to equation 2.14 using FluoFit software (PicoQuant).

Fluorescence Correlation Spectroscopy (FCS)

Fluorescence Correlation Spectroscopy is a widely used technique that measures fluctuations in fluorescence intensities of single molecules/particles. Information about any type of associative and/or physical interactions that result in temporal intensity fluctuations can be extracted using FCS [11]. One of the more established applications of FCS is the determination of concentrations and diffusion coefficients of molecules/particles at pico- to nano-molar concentrations.

In a standard FCS measurement, laser light is focused by a high-numerical aperture objective, which excites a small number of molecules/particles which emit photons (Figure 2.4, panel A). A confocal pinhole, placed between the objective and the detector, reduces the detection volume from which the photons are collected along the Z-axis. The arrival of photons is recorded at a single photon level resulting in a time-tagged time-resolved (TTTR) trace. In the case of a simple diffusion, the passing of fluorophores through the detection volume causes the intensity fluctuations which are reflected in the TTTR trace. The strength and temporal length of these fluorescence fluctuations are quantified by correlating the TTTR trace [11].

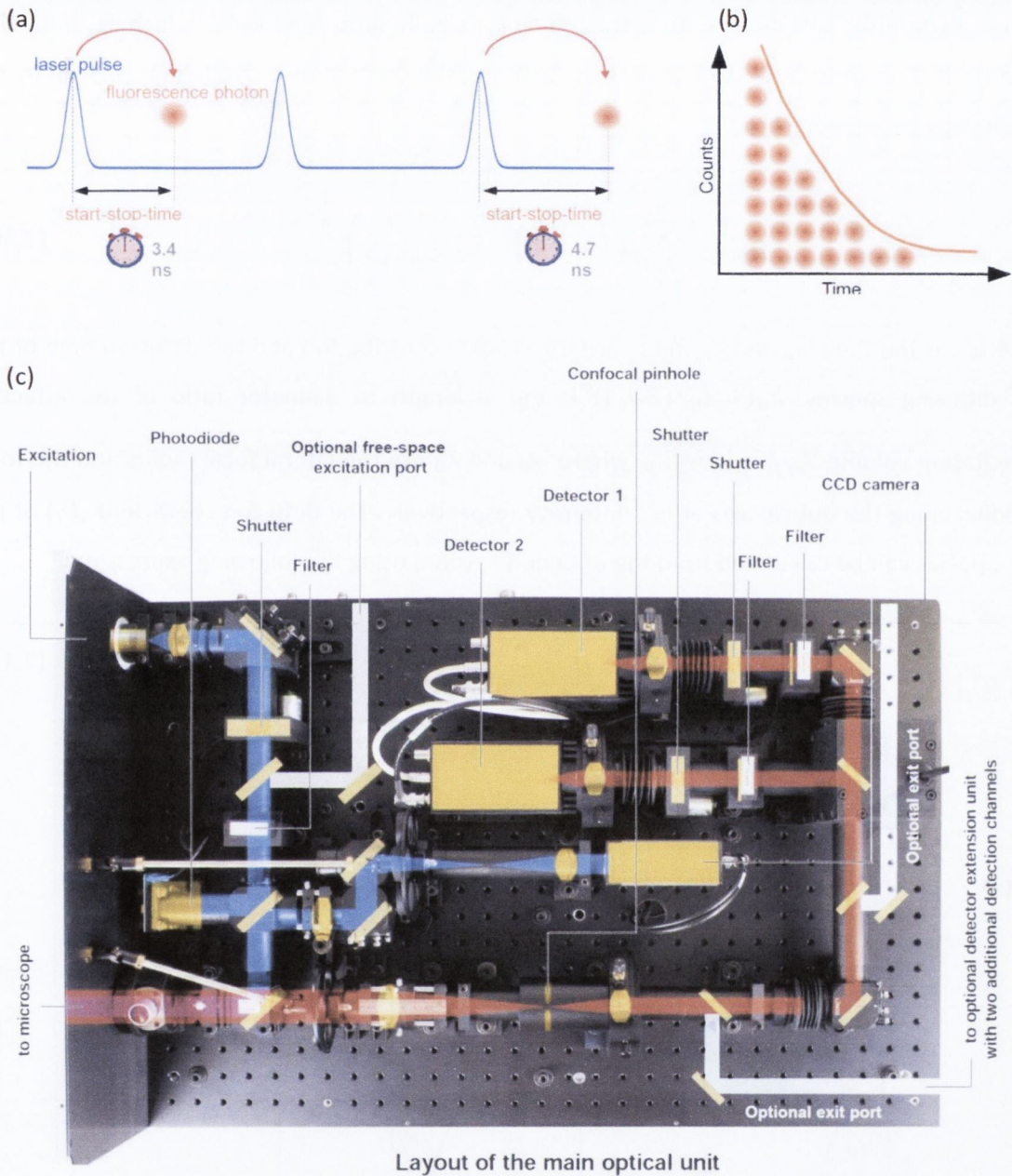


Figure 2.3| Fluorescence Lifetime measurements by Time-Correlated Single Photon Counting (TCSPC). (a) TCSPC records the time-delay between the excitation of the fluorophore and the arrival of emitted photon to a detector. (b) The time delays are recorded over many cycles and are combined to build-up a histogram that represents the decay of the fluorescence. (c) The main optical unit of the MicroTime200 system includes guiding optics for the excitation and emission beams, two avalanche single-photon detectors and a pinhole. Figure was adapted from the MicroTime200 product brochures.

The correlation is a mathematical procedure that evaluates the temporal self-similarity of the trace(s) through calculations of the overlap integral at different time lag values (Figure 2.4, panel B). The correlation curve is then fitted to a theoretical curve from which the values of the sought-after parameters are extracted. For a simple diffusion model, which assumes that only diffusion contributes to intensity fluctuations, the correlation curve ($G(\tau)$) is given by the following expression [12]:

$$G(t) = \sum_i^n \rho_i \left(1 + \frac{t}{\tau_i}\right)^{-1} \left(1 + \frac{t}{\tau_i k_v^2}\right)^{-\frac{1}{2}} \quad (2.16)$$

Here, t is the time lag and ρ_i and τ_i are the relative contribution and the diffusion time of the i^{th} diffusing species. $k_v (= Z_0/(2w_0))$ is the is length to diameter ratio of the effective excitation volume $V_{eff} = \pi^{\frac{3}{2}} w_0^2 Z_0$, where w_0 and Z_0 are the lateral focal radius and the focal radius along the optical axis at e^{-2} intensity respectively. The diffusion coefficient (D_i) of the i^{th} species can be calculated from the obtained τ_i value using the following expression:

$$D_i = \frac{w_0^2}{4\tau_i} \quad (2.17)$$

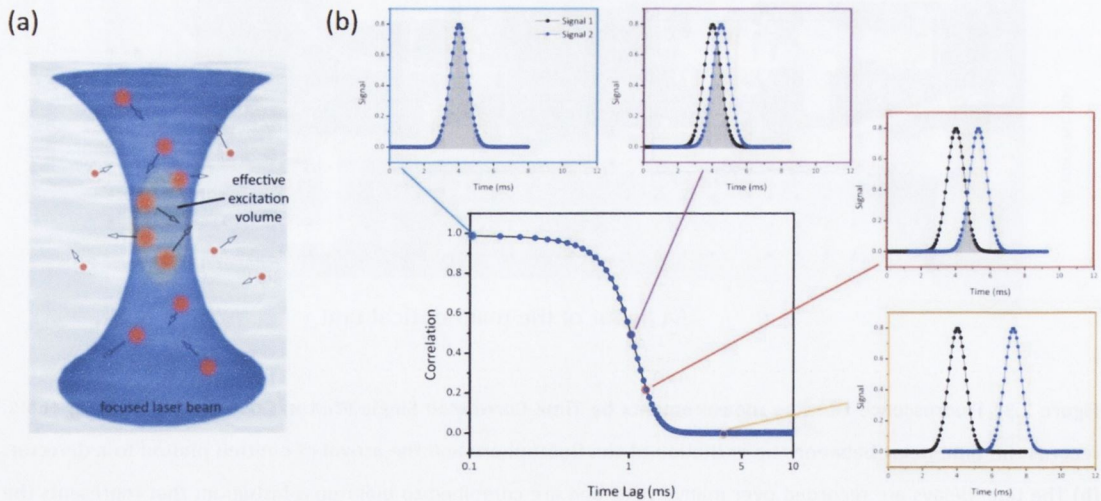


Figure 2.4] Principles of Fluorescence Correlation Spectroscopy. (a) As fluorophores diffuse into and out of the effective excitation volume, the intensity of the detected fluorescence signal fluctuates. These fluctuations are recorded as a function of time to develop the time-tagged time-resolved (TTTR) curve. **(b)** The evaluation of the self-similarity of the TTTR curve at different time lags (smaller graphs) results in the auto-correlation curve (main graph), which can be fitted to a diffusion model to extract the diffusion coefficient of the fluorophore.

The accuracy of the results obtained by the FCS is sensitive to a number of different parameters, including the excitation wavelength, the refractive index of the solvent and the photophysics of the fluorophore, among others. It also relies heavily on the precise knowledge of the dimensions of the effective volume which, for best accuracy of results, must be determined at experimental conditions as the FCS measurements themselves. The three most used methods of determination of V_{eff} are:

1. FCS measurements on a dilution series of a dye.
2. Fitting FCS curve for a standard dye of known diffusion coefficient.
3. Direct measurement by raster scanning of a sub-resolution fluorescent bead.

The advantage of method 1 is that this method can be used with any dye that is readily available in the laboratory, as long as its concentration in the chosen solvent can be accurately determined. The advantage of using a standard dye of known diffusion coefficient (method 2) is that the concentration of the dye does not need to be known precisely. The main advantage of the third method of the determination of the effective volume is that it is a direct measurement, requiring no additional treatment of data.

FCS measurements were performed using a 100x oil-immersion objective on the MicroTime200 described above. The calibration of FCS was performed using methods 1 and 3, as described in Appendix A.

2.3. Other techniques

2.3.1. Zeta potential and nanoparticle size measurements

The determination of the hydrodynamic size of the nanocrystals and their zeta potential (surface charge) are vital factors in the initial characterization of quantum dots – both of these determine the minimal achievable distance between the QDs and the acceptors of energy in solution, a key parameter for the energy transfer efficiency.

Both the size and the surface charge of particles in solution can easily be measured by Dynamic Light Scattering (DLS) measurements. DLS technique is similar in principle to the FCS measurements in that both involve temporal correlation of signal fluctuations caused by movement of particles. However, in the case of DLS, the signal comes from scattering of light by particles compared to emission of photons for FCS. The light scattered by particles interferes constructively and destructively resulting in formation of a 2-D pattern at the detector, consisting of bright and dark patches [13]. As the particles move, the area of these patches increases and decreases and it is these fluctuations that are correlated in time.

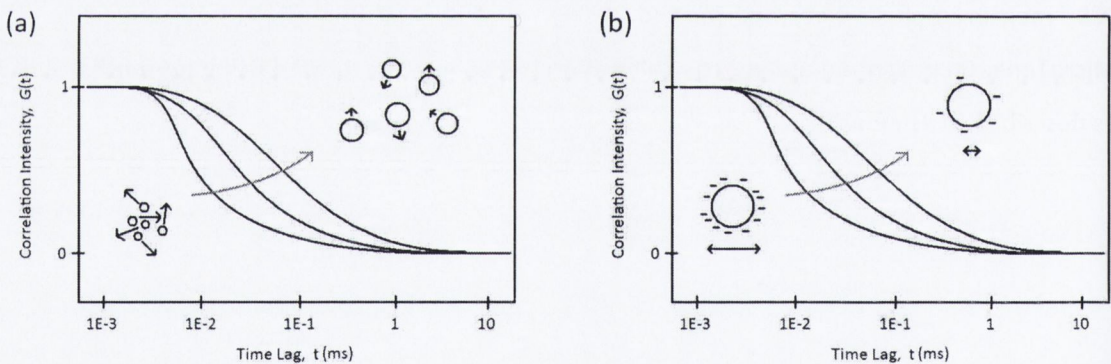


Figure 2.5| Determination of particle size and surface charge by DLS measurements. (a) The correlation intensity of the light scattered by particles undergoing Brownian motion is strongly dependent on the particles' diameter. The bigger they are, the slower they move and hence correlation remains strong for longer periods of time. **(b)** Particles with smaller surface charge move slower, and so correlation is stronger at higher time lag values.

For size measurements, the movement of the particles is due to the Brownian motion. The larger the particles, the slower they move and so the correlation remains large for longer time lag periods (Figure 2.5, panel A). In zeta potential measurements, an alternating voltage is applied across the liquid, causing the position of the charged particles to oscillate. The higher the charge, the faster the particles move thereby decreasing the correlation at higher time lag

periods (Figure 2.5, panel B). In both cases, the sought-after parameters are determined by fitting the correlation curve to a theoretical model.

Zeta potential and hydrodynamic diameter of quantum dots or QD-containing complexes were measured using a NanoZS ZetaSizer (Malvern). Disposable polystyrene cuvettes (DTS0012) and Folded Capillary cells (DTS1060) were utilized for size and zeta potential measurements respectively. Prior to measurements, samples were filtrated through the 0.22 μm Ultrafree[®]-MC microcentrifuge filters (Sigma), diluted to $\sim 10^{-5} M$ with deionised water and then sonicated for 60 seconds. Measurements were performed at 20°C, the duration of each measurement was determined automatically by the Malvern software. For each sample, three measurements with 20 repeats were performed and the results were averaged.

References

1. Rogach, A.L., et al., *Synthesis and characterization of thiol-stabilized CdTe nanocrystals*. Ber Bunsen Phys Chem **100**, 1772-1778 (1996)
2. Hines, M.A. and P. Guyot-Sionnest, *Synthesis and characterization of strongly luminescing ZnS-Capped CdSe nanocrystals*. J. Phys. Chem. **100**, 468-471 (1996)
3. Sukhanova, A., et al., *Lab-in-a-drop: controlled self-assembly of CdSe/ZnS quantum dots and quantum rods into polycrystalline nanostructures with desired optical properties*. Nanotechnology **18**, 185602 (2007)
4. Nabiev, I., et al., *Fluorescent Colloidal Particles as Detection Tools in Biotechnology Systems*. John Wiley & Sons, Inc. (2007)
5. Sukhanova, A., et al., *Highly Stable Fluorescent Nanocrystals as a Novel Class of Labels for Immunohistochemical Analysis of Paraffin-Embedded Tissue Sections*. **82**, 1259-1261 (2002)
6. Yu, W.W., et al., *Experimental determination of the extinction coefficient of CdTe, CdSe, and CdS nanocrystals*. Chem. Mater. **15**, 2854-2860 (2003)
7. Kubista, M., et al., *Experimental correction for the inner-filter effect in fluorescence spectra*. Analyst **119**, 417-419 (1994)
8. Wolberg, J., *Data analysis using the method of least squares: extracting the most information from experiments*. 1st ed. Springer (2005)
9. Lakowicz, J.R., *Principles of Fluorescence Spectroscopy*, (Eds.). pp. 331-352. Springer, New York (2006)
10. Lakowicz, J.R., *Principles of Fluorescence Spectroscopy*, (Eds.). pp. 98-157. Springer, New York (2006)
11. Hausteil, E. and P. Schwille, *Fluorescence Correlation Spectroscopy: Novel Variations of an Established Technique*. Annu. Rev. Bioph. Biom. **36**, 151-169 (2007)
12. Buschmann, V., et al. (2009) *Quantitative FCS: determination of the confocal volume by FCS and bead scanning with the MicroTime 200*. PicoQuant, Application Notes: <http://www.picoquant.de/getfs.htm?appnotes.htm>
13. Malvern Instruments (2004) *ZetaSizer NanoSeries: User Manual*. <http://www.nbtc.cornell.edu/facilities/downloads/Zetasizer%20Manual.pdf>

3. PHOTSENSITISER/QUANTUM DOT SYSTEM

On average, about 1.5 million people are diagnosed with cancer and approximately 550 thousand people die from it every year in USA alone [1]. It is the second most likely disease to cause death and, statistically, every second man and every third woman will be diagnosed with some type of cancer during their lifetime. Hence, the need for the development of new, more advanced and/or more efficient treatments has never been more evident.

Several types of cancer treatments are in common use today. Of these, chemotherapy, radiotherapy and surgery have received the most attention in research. The lesser known cancer treatment techniques include biological therapy, antiogenesis inhibitors therapy, bone marrow and peripheral blood stem cell transplantations, hypothermia treatments, gene therapy and photodynamic therapy [1]. While these treatments are based on different principles, all of them have the same functional goal – the specific death of cancerous cells. Here “specific” refers to an ideal situation where only cancer cells are affected by the treatment, minimising the side effects of the treatment. Of all the above mentioned therapies, photodynamic therapy offers perhaps the best potential in this regard. In this chapter the investigations into the enhancement of photodynamic properties of a photosensitiser using colloidal semiconductor quantum dots are reported.

3.1. Introduction

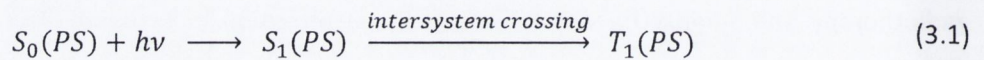
3.1.1. Photodynamic Therapy (PDT)

Photodynamic therapy is a type of cancer treatment. It is similar to chemotherapy in that it involves an injection of a chemical into a body – the photosensitiser (PS). However, unlike the chemotherapy drugs, the photosensitiser only becomes harmful to cancer cells once it is illuminated by light of a certain wavelength [2]. Hence the treatment limits the number of healthy cells affected by the treatment and avoids the many detrimental side-effects typically associated with chemotherapy.

The photosensitiser is the key element of the photodynamic therapy. Upon illumination with light of specific wavelength, the photosensitiser produces reactive oxygen species (ROS) – singlet oxygen molecules, free radicals or highly reactive charged species – which attack the

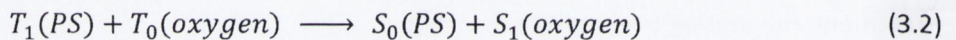
lipid membrane of the cells by lipid peroxidation, ultimately leading to cell death [3]. Among the above mentioned ROS, the production of singlet oxygen is of particular importance since it has been linked to apoptosis – a more favourable type of cell death that includes a safe disposal of cellular debris [4]. The production of other reactive oxygen species, such as free oxygen radicals, is more likely to cause necrosis – a form of traumatic cell death that often leads to inflammation and other complications [4].

The production of singlet oxygen by a photosensitizer involves several steps [5]. The first is the formation of the excited triplet state of the PS ($T_1(PS)$) by intersystem crossing from the singlet excited state ($S_1(PS)$):



where $S_0(PS)$ is the singlet ground state of the photosensitiser.

This is followed by a transfer of energy to the ground triplet state of oxygen ($T_0(oxygen)$) to produce the highly reactive singlet excited state ($S_1(oxygen)$):



3.1.1. Use of QDs in medicine

The majority of the investigations involving the application of semiconductor quantum dots in medicine have been in the field of bio-imaging and bio-labelling. This is due to the advantages that QDs possess over conventional dyes used for these applications. In particular, QDs have tunable and relatively narrow emission spectra, high photostability and the possibility of exciting QDs of different emission colours at the same wavelength [6]. As a consequence, and despite concerns over toxicity issues, attempts have been made to utilize QDs for the imaging of cellular and sub-cellular structures, imaging of the cell surface receptor dynamics and even real-time cell imaging in live animals [3]. It should be noted that, while several studies have shown that QDs are cytotoxic in vitro [7-9], the toxicity of QDs in vivo is still a hotly debated topic. For example, recently Hauck *et al.* [10] have shown that medium doses of CdSe/ZnS QDs with three different surface functionalities do not cause any appreciable toxicity in Sprague-Dawley rats, even after breakdown in vivo. The general consensus today is that the toxicity of QDs strongly depends on their composition, stability and coating materials [9, 11-13] and future developments in QDs' fabrication are expected to improve on all of these. Thus, the

issue of QDs' toxicity does not inhibit investigations into their use of QDs for medical applications.

In cancer therapies, quantum dots have been investigated both as a diagnostic tool and as a drug delivery system. The first of these is based on the excellent potential of using QDs for imaging *in vivo*, but also on the possibility of specifically targeting particular tumours via functionalization of the QDs' surface [14]. Also, it is known that macromolecules and nanoparticles can accumulate in tumours due to the hypervascularity and the enhanced permeability and retention (EPR) effect [15]. Such passive uptake of QDs has been reported for *in-vivo* studies of different cell populations in syngeneic mice [16]. The EPR effect can thus be exploited for the delivery of drugs attached to the QDs' surface – this would reduce the non-specificity of the drug action and lessen the side-effects of the treatment.

In addition, QDs themselves can act as therapeutics against cancer cells. Various studies have shown that, in response to light in the presence of oxygen, QDs can produce reactive oxygen species [3] – that is, they themselves can act as photosensitisers in PDT although with much lower efficiencies than the PS that are already in use. A recent direction in this research is the addition of QDs to already existing photosensitizers with the aim of enhancing the photodynamic properties of the PDT drugs [17, 18]. We test this hypothesis by examining the photodynamic properties of a model PS (methylene blue) in the presence of colloidal QDs.

3.1.2. Methylene Blue as a Photosensitizer

Methylene Blue is a well-known phenothiazinium dye that has been extensively used for a variety of photochemical [19] and medical [4] applications. Medical uses of MB include the treatment of methemoglobinemia [20], as well as its use as a mild antiseptic [21] and as a tissue stain for diagnostic detection [22] and delineation of body tissues during surgery [23, 24]. By itself, it has very little toxicity and rarely results in side-effects.

The intersystem crossing of excited MB from singlet to a triplet state has a high quantum yield (~ 0.5), and the triplet state has a long intrinsic lifetime [25]. Both of these are important properties of a photosensitizer. However, the use of methylene blue as a photosensitizer in PDT has been limited by the formation of MB dimers [26] and the reduction of MB to the photochemically inactive leuco-MB [27] under physiological conditions. Both of these result in a decrease of its efficiency for singlet oxygen production [4].

The concentration of methylene blue is solution can be determined from its absorption spectrum utilizing extinction coefficient of $73,000 \text{ cm}^{-1} \text{ M}^{-1}$ at 664 nm:

$$C(\text{diluted stock}) = \frac{A_{664 \text{ nm}}}{73,000 \text{ cm}^{-1} \text{ M}^{-1} * 1 \text{ cm}} \quad (3.3)$$

It should be noted, however, that the absorption spectrum of a MB solution depends on its concentration due to dimerization. MB dimers absorb at lower wavelengths ($\sim 590 \text{ nm}$) compared to MB monomers [28], and their distinct absorbance spectra allows the calculation of the monomer to dimer ratio. The dimerization increases in the presence of charged surfaces and with increasing ionic strength of the solution [26, 28]. MB fluoresces weakly in water ($QY \sim 0.04$) with a characteristic PL peak centred at 680 nm.

3.2. Interactions in MB/QD complexes

Investigations of the interactions between semiconductor QDs and a model photosensitiser Methylene blue involved spectroscopic measurements on a series of aqueous solutions containing increasing molar ratios of MB to QDs. Two QD samples were used, with emissions centred at 545 nm and 645 nm, corresponding to average QD diameters of 2.8 nm and 3.3 nm respectively (Figure 3.1, panels A and B respectively). These two samples were chosen because their emissions have widely different spectral overlaps with the absorption band of the Methylene blue dye, shown diagrammatically in Figure 3.1, panel C.

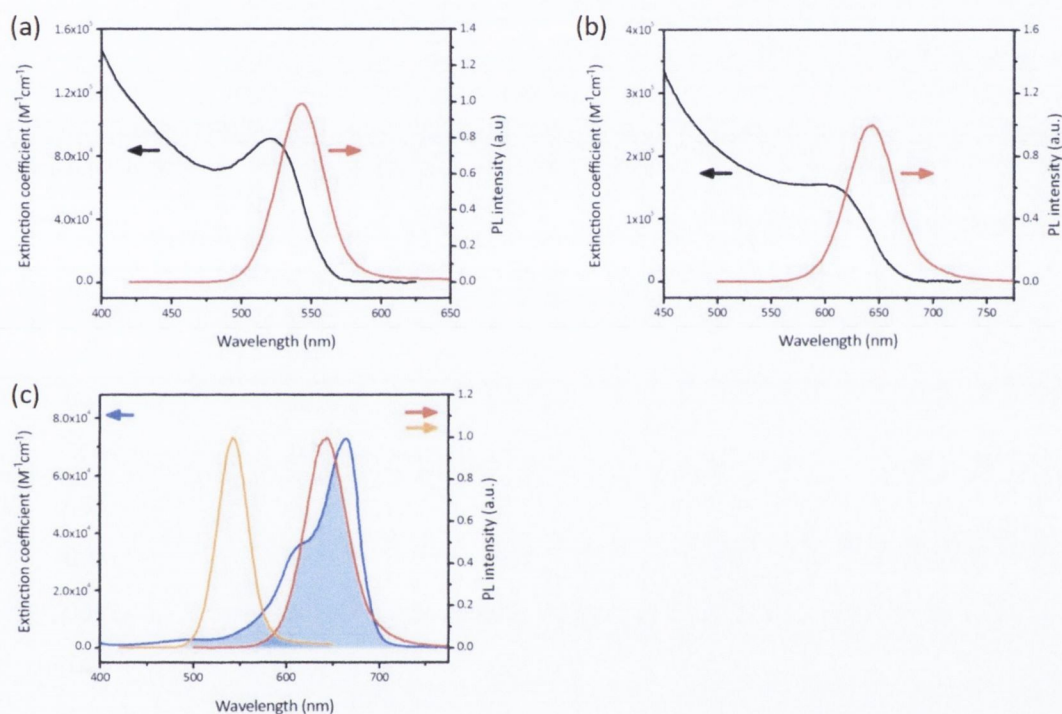


Figure 3.1| Optical characteristics of MB and QD samples. Photoluminescence (red curves, right axes) and absorption (black curves, left axes) spectra of **(a)** QD2.8 and **(b)** QD3.3 samples. **(c)** The 2.8 nm and 3.3 nm QD samples were chosen based on the degree of spectral overlap of their PL bands (orange and red respectively, right axis) with the absorption band of the Methylene blue dye (blue curve, left axis). The spectral overlap integrand for each sample is shaded in blue.

3.2.1. Sample preparation and labelling

Methylene Blue dye powder was purchased from Sigma-Aldrich. A small amount of the dye, of unknown mass, was dissolved in ~ 5 mL of water. Prepared solution was sonicated for ~ 30 seconds to make sure that the dye dissolved fully. This solution was diluted by 20 to 50 times, and the concentration of this diluted solution was determined from the absorption

measurements. The concentrations of the QDs' stock solutions were determined as described in previous chapter (section 2.1.3).

Methylene blue stock solution and QDs' stock solutions were dissolved to give new stocks of 50 μM concentrations. All newly prepared stock solutions were sonicated for ~ 1 min to ensure homogeneity of samples. Increasing amounts of MB stock were then mixed with equal volumes of each of the QDs stocks, resulting in a set of MB-QD mixtures of increasing MB concentrations for each of the QD samples (summarised in Table 3.1). To aid the reference of the samples, each sample was referred to by the QD size (2.8 or 3.3) and letters "a" through "g" corresponding to increasing concentrations of MB (Table 3.1). Prior to measurements, samples were left to equilibrate for ~ 30 min.

Table 3.1 | MB-QD sample composition for spectroscopic measurements. The total volume of prepared samples was 2 mL. CdTe QDs concentrations were kept equal for samples "a" through "f". Sample "a" did not contain any MB, and sample "f" was the MB only control.

Sample label	QD to MB ratio	V (QD stock)	V (MB stock)	V (water)
		μL	μL	μL
a	∞	100	0	1900
b	10:1	100	10	1890
c	5:1	100	20	1880
d	1:1	100	100	1800
e	1:5	100	500	1400
f	1:10	100	1000	900
g	0	0	1000	1000

3.2.2. Assembly of MB/QD complexes

After the preparation of MB/QDs solutions, spectroscopic measurements were performed to identify any interactions and/or associations between the QDs and the MB. The first step in the characterization of samples was to examine their absorption spectra for the occurrence of chemical reactions and/or degradation (Figure 3.2). A degradation of the sample, in the form of the aggregation of QDs, would result in formation of rather large particles which settle to the bottom of the cuvette. An appearance of random peaks and very large noise in the absorbance spectrum is a typical indicator of this process. On the other hand, chemical reactions between components give rise to new absorbance peaks corresponding to newly

formed bonds. As can be seen from Figure 3.2, the absorbance of mixtures containing 2.8 nm QDs (panel A) and 3.3 nm QDs (panel B) show very little noise and have no new absorbance peaks. In fact, the absorption spectra of QD2.8/MB samples appear to be linear combinations of the QD and dye absorptions (panel A of Figure 3.2), indicating a lack of any major chemical changes and degradation of the samples upon mixing of MB and QD solutions.

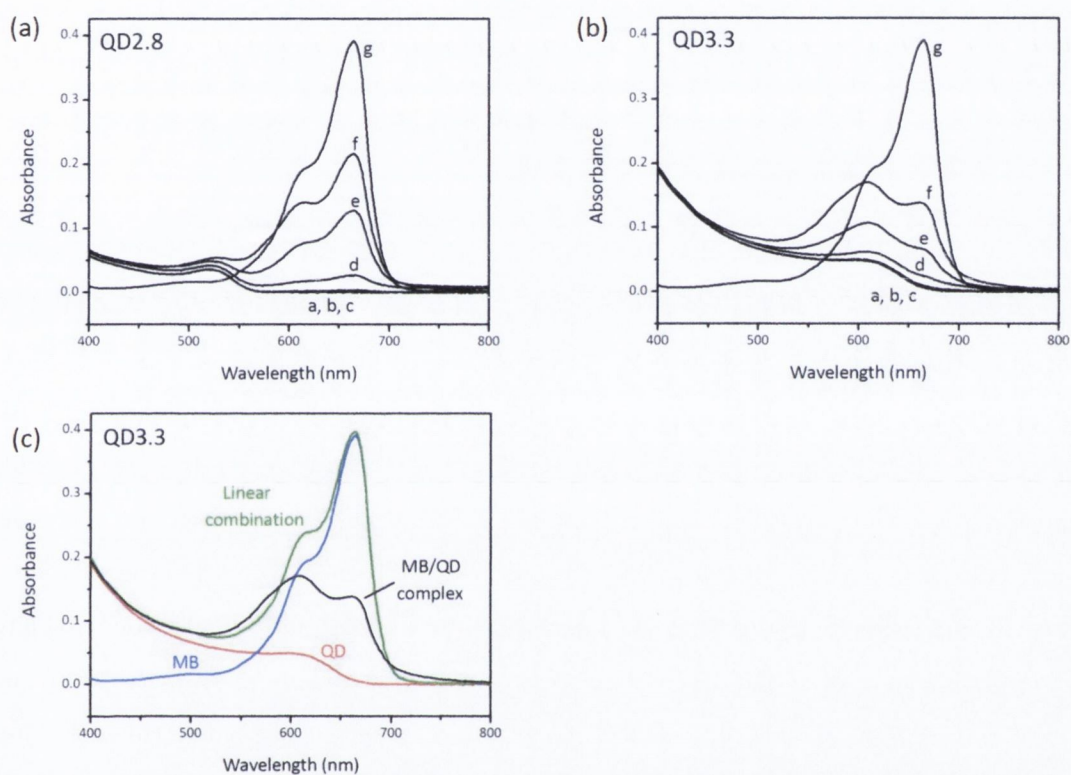


Figure 3.2| Absorbance spectra of MB/QD complexes. The absorbance spectra of MB/QD complexes assembled with (a) 2.8 nm QDs and (b) 3.3 nm QDs have a pronounced decrease at 664 nm, signifying a decrease of MB monomers in solution. A corresponding relative increase of absorbance at and below 613 nm (c) indicates the aggregation of the dye in the presence of QDs, pointing towards the adsorption of MB molecules on QDs' surfaces.

Upon a more careful examination of the absorbance data, some changes in the absorption spectra became apparent. In particular, the reference here is to the absorbance peak centered at 644 nm, corresponding to the monomeric form of methylene blue dye. A pronounced decrease in this peak was observed for samples "f" of both the 2.8 nm QDs and 3.3 nm QDs sets when compared to the absorption of samples "g" (Figure 3.2). Samples "f" and "g" had equal amount of MB dye in their composition (Figure 3.2) and were therefore expected to have similar absorption at 644 nm (Figure 3.2, panel C). The observed decrease of absorption is equivalent to a reduction of methylene blue monomers present in solution when QDs are

added. This suggests that some dimerization of dye molecules occurs. This conclusion is backed up by an increase in the absorption at and below 613 nm, corresponding to the absorption by MB dimers and trimers. This is consistent with previous findings that the presence of interfaces (surfaces) causes partial dimerization of methylene blue [26]. Furthermore, drawing a parallel to the work of Sykora *et al* [29] who observed the adsorption of the positively-charged Ru-Polypyridine complexes onto the negatively-charged CdSe QDs, an *adsorption* of MB molecules onto the QDs' surface can be postulated. The existence of an electrostatic attraction between the positively-charged MB and negatively-charged TGA-capped CdTe QDs re-enforces this hypothesis. Additional measurements were necessitated to validate the adsorption of MB molecules onto QDs.

Due to the relatively high fluorescence quantum yields of QDs, photoluminescence measurements can provide much useful information about the system being studied. It was found that QDs' fluorescence is quenched upon assembly with MB molecules, in a manner that is dependent on both the MB to QD molar ratio and the pH of the solution (Figure 3.3, panel A). The molar ratio dependence of the PL quenching does not provide any decisive insights into the MB-QD association process and is therefore discussed in the next section. On the other hand, the changing of the pH of a sample directly affects the ionic strength of the solution and therefore the solubility of the QDs. For a pure QD solution, both the solubility and stability of nanocrystals improves as the pH of solution is raised, with a subsequent increase of the PL intensity. Once the MB dye is introduced, the QDs fluorescence is quenched. However, due to an increased ionic strength of the solution the association/attraction between the MB molecules and QDs is reduced resulting in lesser adsorption of MB molecules onto QDs and incomplete PL quenching for pH values above 11 (Figure 3.3, panel A).

A more direct confirmation for the adsorption of MB molecules onto QD's surface was obtained from the FCS measurements of a 3.3 nm QD set (Figure 3.5, panel B). The basis of this technique is the recording of the emission of a fluorophore, in our case a QD, as it diffuses through a small excitation volume (see inset of panel B, Figure 3.5). The temporal correlation of this record yields an FCS curve, and a simple theoretical fit to this curve allows the calculation of the diffusion coefficient of the fluorophore. An adsorption of MB molecules onto QDs would increase the average mass of QDs and would therefore result in a decrease of the QDs' diffusion coefficient. For samples 3.3a through 3.3d this was found to be the case (Table 3.2).

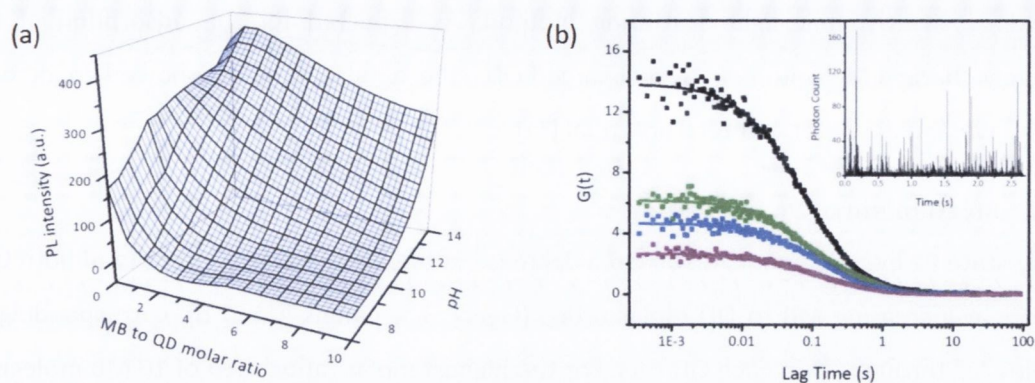


Figure 3.3| Adsorption of Methylene blue onto QDs. (a) pH-dependence of the PL quenching of 3.3 nm QDs is indicative of the adsorption of MB molecules onto QDs' surface. (b) Fluorescence Correlation Spectroscopy curves of a (■), b (■), c (■) and d (■) MB-QD3.3 complexes diffusing through an excitation volume were calculated by temporal correlation of the corresponding TTR traces (inset). The decrease of the correlation value at short lag times ($G(0)$) is due to the quenching of QDs' fluorescence by MB. Fitting of the FCS curves revealed a decrease of QDs' diffusion coefficient at increasing MB to QD ratios (Table 3.2).

Table 3.2| FCS and ZetaSizer results for QD3.3/MB complexes. The diffusion coefficients of complexes were calculated from the FCS correlation curves (Figure 3.3, panel A) and were found to increase for high MB to QD molar ratios, suggesting the adsorption of MB molecules onto QDs' surface. The fluorescence signal of e and f samples was too low to obtain accurate fits to correlation curves, and so hydrodynamic size and zeta potential measurements were performed instead. In accordance with other results, these measurements showed an increasing particle size and a decrease in the zeta potential of QDs as positively charged MB adsorbed onto the negatively charged QDs.

Sample	Diffusion Coefficient ($\mu\text{m}^2/\text{s}$)	Hydrodynamic Size (nm)	Zeta Potential (mV)
3.3a	259.6	4.33	-39.1
3.3b	183.3		
3.3c	160.9		
3.3d	158.3		
3.3e	Fluorescence signal too low: zeta potential	4.53	-34.1
3.3f	and size measurements were taken instead	4.85	-31.3

The intensity of PL emission of samples 3.3e and 3.3f was too low to obtain accurate results from the fitting of the FCS curves, and so zeta potential and size of the QDs were measured instead by the dynamic light scattering method. As expected for the adsorption of the positively-charged MB onto negatively-charged QDs, these measurements showed an increase of QDs' average diameter and zeta-potential (Table 3.2).

3.2.3. Mechanism of PL quenching

Steady-state PL measurements disclosed a decrease in the luminescence intensity of both QDs samples at increasing MB to QD molar ratios (Figure 3.5, panels A and B), corresponding to samples "a" through "f" in each QD sets. For the highest molar ratios used of 10 MB molecules per QD (samples "f"), complete quenching of QDs' PL was achieved. The 3.3 nm QDs were quenched more efficiently (Figure 3.5, panel B), that is, less MB molecules were required to quench the luminescence of this sample by the same amount. Assuming that in this system quenching occurs through Förster Resonance Energy Transfer (FRET), this difference could be attributed to the lesser overlap of 2.8 nm NC emission band and MB absorption band compared to 3.3 nm NCs (Figure 3.1, panel C). However, the similarity of the quenching curves was in contrast to the large difference of the spectral overlap for the two QDs samples. Furthermore, in absence of other effects, a typical result of FRET is an enhanced emission from the fluorescent acceptor [30], which in this case is the MB dye. However, no such enhancement was observed for either of the samples. In fact, at 400 nm excitation, the photoluminescence of MB was also fully quenched (inset of panel A of Figure 3.5).

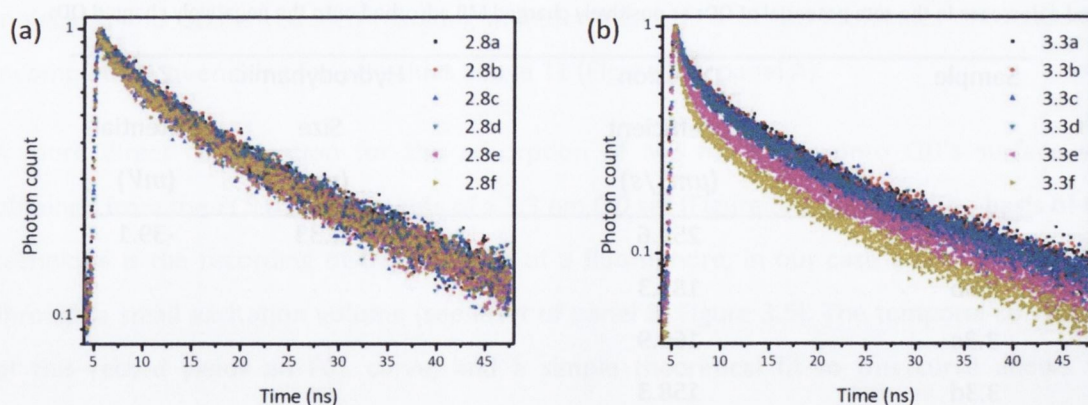


Figure 3.4 | Time-resolved photoluminescence measurements. (a) The photoluminescence decay of the 2.8 nm QDs remained unchanged upon addition of MB to QDs solution. (b) A small increase in the rate of the PL decay was observed for the 3.3 nm QDs, corresponding to a small contribution of FRET to the slightly more efficient quenching of QD3.3 fluorescence when compared to that of the 2.8 nm QDs.

Lifetime measurements are often conducted in order to confirm the occurrence of energy transfer in a system – a decrease of the average lifetime of a donor is expected [31]. As seen in Figure 3.4, no change in the lifetime of 2.8 nm QDs was detected and a very small decrease in the lifetime of the 3.3 nm QDs was observed. Taking into account the large difference in the spectral overlap between MB absorption and QD emission spectra for the two samples, we expected a much larger difference in the behavior of PL decays for the two series. Thus, PL decay measurements confirm that FRET cannot be fully responsible for the observed effect, but may contribute to the quenching of luminescence for the 3.3 nm QD sample.

The inspection of band off-sets for MB dye and QDs samples [32] (Figure 3.5, panel C), pointed towards a possibility of a charge transfer as a more likely mechanism of photoluminescence quenching. The adsorption of methylene blue dye onto the QDs' surface provides the close proximity of the two moieties necessary for the charge transfer between them [33]. In this case, the similarity of the quenching curves is due to the fact that charge transfer occurs in similar measures for both QD samples. The slightly more effective quenching of 3.3 nm QDs emission is due to the FRET, which is aided by the large spectral overlap between QD3.3's photoluminescence and MB's absorption bands.

More detailed investigations of the PL changes in MB/QD complexes suggest a *photoinduced* charge transfer (PCT) is the most likely mechanism of luminescence quenching. The evidence for the *photoinduction* can be derived from the comparison of the PL spectra of the 2.8 nm QD set 633 nm excitation (Figure 3.5, panel D). As discussed above, when QD/MB mixtures were excited at 400 nm, complete quenching of the MB dye luminescence was observed. However, at 633 nm, the excitation of the 2.8 nm QDs is minimal (see panel A of Figure 3.1) and a PL signal due to the MB dye (~680 nm) was detected. The signal increased in proportion to the absorption value of the samples at the excitation wavelength. The inset panel C (Figure 3.5) shows PL spectra normalized to the absorption of two MB/QD samples of equal methylene blue concentrations (2.8f and 2.8g) at 633 nm. The intensity of the normalized PL was found to be same for both samples, indicating a lack of quenching at this excitation wavelength. Therefore, PL quenching of the 2.8 nm QDs and MB only occurs when QDs are excited, hence the charge transfer is induced by the excitation of QDs.

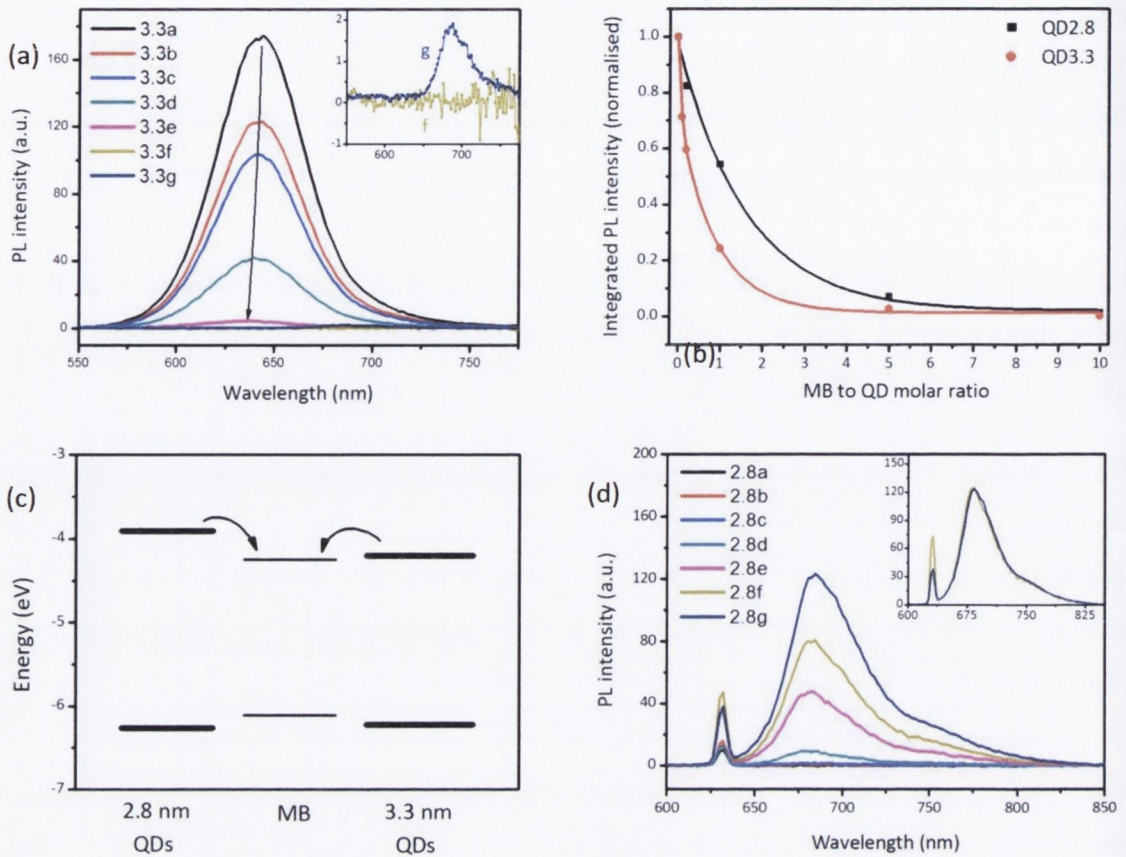


Figure 3.5] Quenching of QDs' fluorescence by Methylene blue. (a) Complete quenching of 3.3 nm QDs' photoluminescence was observed for complex 3.3f, which has largest MB to QD molar ratio. However, complete quenching of MB's fluorescence was also observed (inset), suggesting a quenching mechanism other than energy transfer to be responsible for quenching, most likely charge transfer. The energy band off-set diagram of Methylene blue and the two QD samples, shown in panel (c), indicates that such a mechanism of quenching is possible. (b) Comparison of PL curves for 2.8 nm (black squares) and 3.3 nm (red circles) QD samples shows that the photoluminescence of the 3.3 nm QDs is quenched more efficiently by the same number of MB molecules. The difference can be attributed to the energy transfer from the 3.3 nm QDs, which have a larger spectral overlap with MB's absorption band. (d) Photoluminescence spectra of QD2.8/MB complexes at 633 nm excitation. At this wavelength, QDs are not excited and only MB's emission at 680 nm is observed. The emission was found to be proportional to the absorption value at the excitation wavelength as can be seen in the inset, which shows the PL spectra of 2.8f and 2.8g samples normalised to absorption at 633 nm.

3.3. Photodynamic properties of MB/QD complexes

In photodynamic therapy, the excitation of a photosensitiser results in production of reactive oxygen species, be that oxygen radicals or singlet oxygen. These species then damage the cells thereby decreasing their rate of proliferation. An improvement of the photodynamic properties of a PS should therefore be accompanied by both of these. The following sections relay the measurements of the singlet oxygen production by the MB/QD complexes and cell proliferation studies of cancerous cell lines in MB/QD – containing solutions.

3.3.1. Production of Singlet Oxygen

Both the energy and the charge transfer discussed above suggest an increased excitation of MB molecules at wavelengths where the QDs absorb. In terms of the reactive species produced, we expect charge transfer to result in the production of charged molecules and/or radicals. On the other hand, FRET is likely to increase the yield of singlet-MB to triplet-MB transition, and thus may increase the efficiency of singlet oxygen production by MB. We have attempted to detect the increase in $^1\text{O}_2$ production by NIR PL measurements.

For these measurements, the QD/MB complexes were assembled in heavy water (D_2O). Replacing normal water (H_2O) by heavy water lengthens the lifetime of the singlet oxygen [34] and allows its detection by direct spectroscopic measurements [35]. Only the 3.3 nm QDs sample was used since no FRET was observed for the 2.8 nm QD set. Samples with the highest methylene blue concentration were used to minimize the error in the measurements.

The spectra of 3.3f (MB and QDs) and 3.3g (MB only) samples had a peak centred at 1268 nm (Figure 3.6, top graph). This peak is due to the singlet oxygen molecules in heavy water [35]. The singlet oxygen peak was slightly higher for the 3.3f sample and, after background subtraction, the differential PL intensity showed that this is indeed the case (Figure 3.6, bottom graph). There was a slight increase ($\sim 14\%$) in the integrated PL intensity of singlet oxygen produced by MB when a small amount of QDs was added⁴. Therefore, the efficiency of singlet oxygen production by a photosensitiser can indeed be increased by utilizing QDs as a source of additional excitation of the PS molecule.

⁴ Due to their high QY, QDs have detectable emissions in the NIR. As a result, when larger amounts of QDs were added to MB, the emission peak due to the singlet oxygen was no longer resolvable.

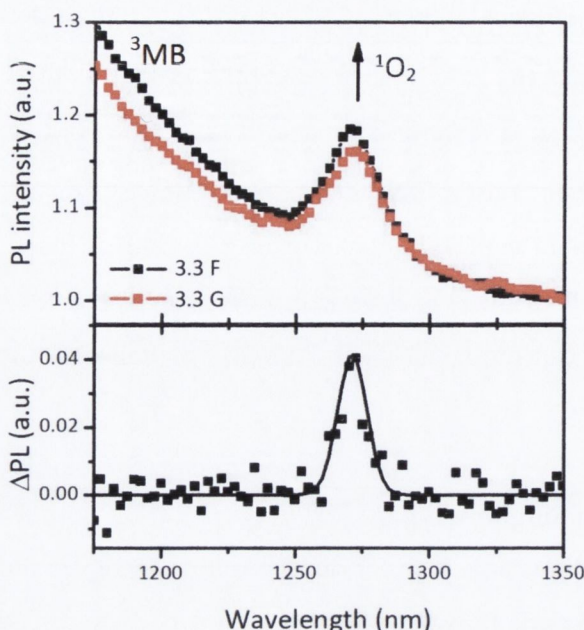


Figure 3.6] Direct spectroscopic observation of singlet oxygen. Top panel shows the evolution of the NIR PL spectra of a Methylene blue solution (sample 3.3g, -■-) upon addition of a small amount of 3.3 nm QDs (sample 3.3f, -■-). A slight increase of the singlet oxygen peak at 1268 nm, indicated by the arrow, suggests an increase in the production of $^1\text{O}_2$ upon assembly of MB and QDs. The increasing PL signal at the lower wavelengths is a tail of emission of the triplet MB state (^3MB). Bottom panel: difference in the spectra of 3.3f and 3.3g samples, after correction for ^3MB contribution by least squares analysis. The increase of the singlet oxygen peak at ~ 1270 nm is clearly distinguishable above the noise. The solid line is for guiding purposes only.

3.3.2. Cell growth in the presence of PS/QD complexes

Both singlet oxygen and oxygen radicals have been linked to cell death [36]. Hence, an increased production of singlet oxygen and the existence of charge transfer from QDs to MB suggest that addition of the QDs can increase the cell kill efficiency of MB. In the final set of experiments, the effect of adding MB/QD complexes to the growth medium on the proliferation of cancerous cell lines was studied. Two cell lines commonly used in cancer research were chosen for this purpose.

HeLa and HepG2 cancerous cell lines were bought from the European Collection of Cell Cultures. Cells were received frozen in growth medium supplemented with 5% (v/v) DMSO. Cells were stored at -82 °C until needed. Before use they were defrosted and subcultured by first removing and discarding the culture medium and then rinsing the cell layers with a 0.25 % w/v Trypsin in 0.53 mM EDTA solution. 3 mL of Trypsin/EDTA solution was then added to flask and cells were monitored using an inverted microscope until complete dispersion was obtained. To the flask, 8 mL of growth medium was added, consisting of a 10% fetal bovine

serum in a serum-free medium ultraculture (Lonza). Cells were gently aspirated using a pipette and distributed to new culture flasks. Subcultures were incubated at 37 °C in a 5% CO₂ humidified atmosphere. For all proliferation studies, a subcultivation ratio of 1:2 to 1:6 was used, and growth medium was replaced 2-3 times a week.

To study the effect of the MB-QD solutions on the growth statistics of cell lines, the following protocol was used:

1. 5 μM stock solution of 3.3 nm QDs was prepared.
2. A series of MB stock solutions were prepared with concentrations ranging from 5 to 150 μM, corresponding to the MB to QD molar ratio range of 1:1 to 30:1 (see Table 3.3).
3. Either HeLa or HepG2 cancerous cells were seeded onto 96 wells of a 96-well plate (average of 5000 – 1000 cells per well)
4. To each well of the plate, 5 μL of QDs stock solution and 5 μL of one of the MB stock solution were added, as summarised in Table 3.3 and Figure 3.7.
5. The plate was placed under a standard UV lamp, at a distance of approximately 10 cm for 30 or 60 seconds.
6. The cells were then washed with fresh growth medium and incubated for 24-32 hours.
7. At the end of the incubation period, cells were counted using either a CyQuant Cell Proliferation Assay Kit or a haemocytometer. The description of the latter technique can be found in Appendix B.

Table 3.3| PS-QD sample composition for cell proliferation studies. To each well of a 96-well plate containing cancerous cells, 5 μL of QD and MB stock were added. Depending on the concentration of the stock solutions used, the MB to QD molar ratio in the sample was varied from 1:1 to 30:1.

C(QD stock)	C(MB stock)	MB to QD ratio
μM	μM	
5	5	1:1
5	25	5:1
5	50	10:1
5	100	20:1
5	150	30:1

The first cell proliferation experiments were performed with HepG2 cell line. However, very large variations in the number of cells remaining alive after 24 hour incubation were observed from well to well, which made it impossible to make any conclusions in regards to the cell kill efficiency of the QD/MB hybrid system. The cause of these variations was the fact the HepG2 cells have a tendency to grow in clusters. As a result, the MB and QD solutions did not have equal access to all cells. In contrast, HeLa cells preferentially grow in monolayers. This resulted in much smaller variations in counts for the repeats of any one sample.

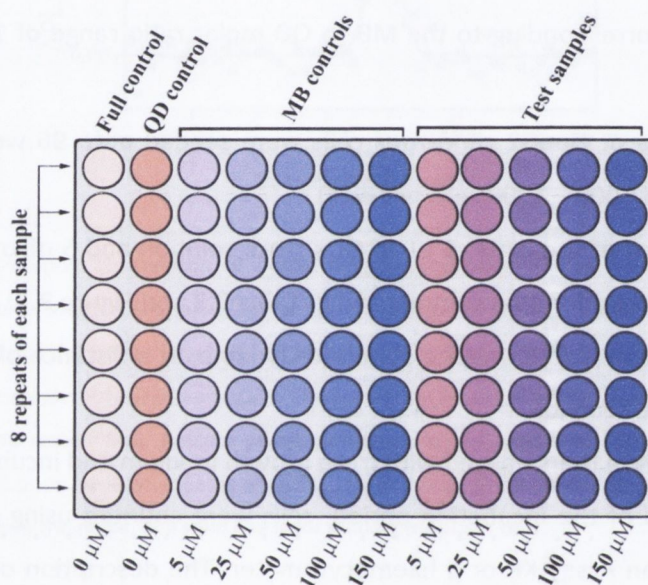


Figure 3.7| Contents of the 96-well plate used for proliferation studies. HeLa or HepG2 cells in a growth medium were seeded into each well. 5 μL of 5 μM QD solution was added to lines labelled “QD control” and “test samples”. No Methylene blue or QD solution was added to wells in line labelled “full control”. To all other lines, 5 μL of one of MB stocks was added. The concentration of MB stock added to each line is given at the bottom of figure. Each sample was reproduced 8 times.

The growth of HeLa cells after 30 seconds of illumination under a UV lamp depended on the contents of the growth solution. Cells proliferation was most efficient for the “full control” samples which contained no MB or QD solutions in their culture mediums. The presence of both QDs and MB on their own inhibited the growth of the HeLa cells, resulting in smaller number of cells being counted after 24 hour incubation period (black and grey bars in Figure 3.8). The reduction of cell growth by QD/MB mixtures was only slightly bigger, with a more pronounced effect for smaller MB to QD molar ratios (Figure 3.8, panel A). Smaller MB to QD ratios correspond to a larger amount of QDs available to transfer energy or charge to MB molecules, and hence the effect is largest for these samples.

Next, the time of illumination of QD/MB complexes by a UV lamp was doubled from 30 to 60 seconds. It is reasonable to assume that a prolonged excitation of MB/QD solutions would result in an increased production of ROS, therefore leading to increased cell kill efficiency. Comparison of cell proliferation measurements for 30 and 60 seconds illumination of HeLa cells in the presence of 1:1 MB:QD complexes revealed that this is indeed the case – the number of cells counted after the incubation was ~15% smaller than the product of the “MB only” and “QD only” controls (lower graph of panel B, Figure 3.8).

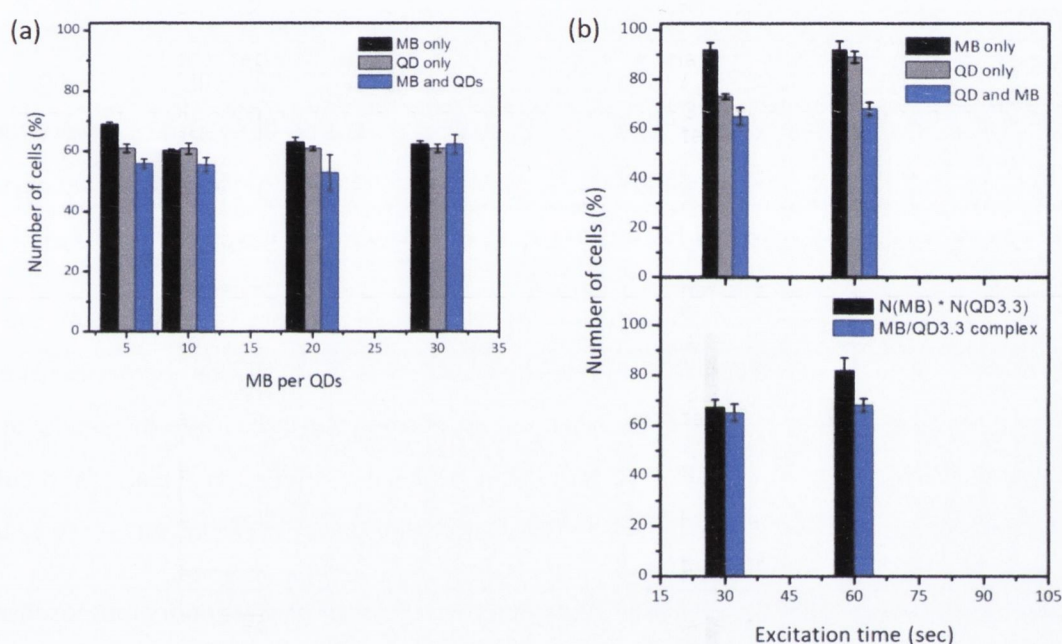


Figure 3.8 | Proliferation studies of HeLa cell line in the presence of PS/QD complexes. (a) HeLa cells were grown in solutions containing MB/QD complexes of different MB to QD molar ratios. Samples were excited for 30 seconds under a UV lamp before 24 hour incubation, after which the number of cells in each sample was counted. A strong dependency on the molar ratio was observed when cell counts were normalised to the “no QD, no MB” control. When compared to the “MB only” (black bars) and “QD only” (grey bars) controls, the maximum effect of MB/QD complexes (blue bars) was observed for those with smaller MB to QD ratios. Results for the 1:1 MB to QD sample were omitted for clarity and it can be found in the top graph of panel (b). **(b)** A decrease in the number of cells remaining alive after 24 hour incubation was found to become more pronounced at longer excitation times. The top graph shows the original cell count data for “QD only” control (grey bars), “MB only” control (black bars) and 1:1 MB/QD complex (blue bars). The bottom graph compares the number of cell for the same MB/QD complex to the combined effect of the control samples, i.e. the product of the “MB only” and “QD only” controls shown in top graph.

3.4. Conclusions

In this study a hypothesis that colloidal quantum dots can be used to increase the photodynamic efficiency of a photosensitizer is tested. Methylene blue dye, which possesses reasonable photodynamic properties, was employed as the model photosensitizer.

MB was assembled with CdTe QDs in aqueous solutions at increasing MB to QD molar ratios. A series of spectroscopic measurements revealed that methylene blue molecules adsorb onto the QDs' surface followed by a partial dimerization of the dye. Subsequently, the fluorescence of QDs was quenched, presumably by charge transfer from QDs to MB, aided by Förster Resonance Energy Transfer provided there was sufficient spectral overlap between QDs' PL and MB absorption bands. It should be noted that while charge transfer is commonly observed in QD-based systems, there are several obstacles to this mechanism. One of the main factors that can affect this process is the presence of negative charges on QD's surface. Investigations into the effect of QDs' surface charge on the quenching efficiency of their PL should certainly provide an insight into the nature of the interactions between the QDs and the MB dye.

Both of the charge and energy transfer processes imply increased excitation of the dye molecules, advocating an increase in the efficiency of MB to produce reactive oxygen species. Near-infrared photoluminescence measurements confirmed the increase in the production of singlet oxygen by MB in heavy water, while proliferation studies of HeLa cells in culture mediums containing MB/QD complexes demonstrated an increase in cell kill efficiency of MB.

These results suggest the possibility of improving the efficiency of any generic photosensitizer utilizing colloidal semiconductor quantum dots as light-harvesting elements. The broad absorption bands of quantum dots mean that the necessity of the expensive monochromatic light sources for PDT can be reduced.

References

1. American Cancer Society: Probability (%) of Developing Invasive Cancers Over Selected Age Intervals by Sex, US, 2004-2006. Available from: <http://www.cancer.org/Research/CancerFactsFigures/>
2. Prasad, P.N., Light-Activated Therapy: Photodynamic Therapy, in Introduction to Biophotonics (Eds.: P.N. Prasad). pp. 433-463. John Wiley & Sons, Inc. (2004)
3. Choi, A.O. and D. Maysinger, Applications of quantum dots in biomedicine, in Semiconductor Nanocrystal Quantum Dots (Eds.: A.L. Rogach). pp. 349-365. Springer, Vienna (2008)
4. Tardivo, J.P., et al., Methylene blue in photodynamic therapy: From basic mechanisms to clinical applications. *Photodiagn. and Photodyn.* 2, 175-191 (2005)
5. Niemz, M.H., *Laser-Tissue Interactions: Fundamentals and Applications*. 3rd ed. Springer, Berlin (2004)
6. Prasad, P.N., Nanophotonics for Biotechnology and Nanomedicine, in Nanophotonics (Eds.: P.N. Prasad). pp. 355-379. John Wiley & Sons, Inc., New Jersey (2004)
7. Zhang, Y.B., et al., In vitro and in vivo toxicity of CdTe nanoparticles. *J. Nanosci. Nanotechnol.* 7, 497-503 (2007)
8. Shiohara, A., et al., On the cyto-toxicity caused by quantum dots. *Microbiol. Immunol.* 48, 669-675 (2004)
9. Hoshino, A., et al., Physicochemical Properties and Cellular Toxicity of Nanocrystal Quantum Dots Depend on Their Surface Modification. *Nano Lett.* 4, 2163-2169 (2004)
10. Hauck, T.S., et al., In vivo Quantum-Dot Toxicity Assessment. *Small* 6, 138-144 (2010)
11. Aillon, K.L., et al., Effects of nanomaterial physicochemical properties on in vivo toxicity. *Adv. Drug Deliv. Rev.* 61, 457-466 (2009)
12. Derfus, A.M., W.C.W. Chan, and S.N. Bhatia, Probing the cytotoxicity of semiconductor quantum dots. *Nano Lett.* 4, 11-18 (2004)
13. Kirchner, C., et al., Cytotoxicity of Colloidal CdSe and CdSe/ZnS Nanoparticles. *Nano Lett.* 5, 331-338 (2004)
14. Gao, X.H., et al., In vivo cancer targeting and imaging with semiconductor quantum dots. *Nat. Biotechnol.* 22, 969-976 (2004)
15. Matsumura, Y. and H. Maeda, A new concept for macromolecular therapeutics in cancer chemotherapy: mechanism of tumorotropic accumulation of proteins and the antitumor agent smancs. *Cancer Res.* 46, 6387-6392 (1986)
16. Voura, E.B., et al., Tracking metastatic tumor cell extravasation with quantum dot nanocrystals and fluorescence emission-scanning microscopy. *Nat Med* 10, 993-998 (2004)
17. Samia, A.C., S. Dayal, and C. Burda, Quantum dot-based energy transfer: perspectives and potential for applications in photodynamic therapy. *Photochem. Photobiol.* 82, 617-625 (2006)
18. Samia, A.C.S., X. Chen, and C. Burda, Semiconductor Quantum Dots for Photodynamic Therapy. *J. Am. Chem. Soc.* 125, 15736-15737 (2003)
19. Pecci, L., et al., Methylene blue photosensitized oxidation of hypotaurine in the presence of azide generates reactive nitrogen species: formation of nitrotyrosine. *Biochem. Biophys. Res. Commun.* 301, 411-416 (2003)
20. Bodansky, O., Mechanism of action of methylene blue in treatment of methemoglobinemia. *J. Am. Med. Assoc.* 142, 923 (1950)
21. Perni, S., et al., Antibacterial Activity of Light-Activated Silicone Containing Methylene Blue and Gold Nanoparticles of Different Sizes. *J. Clust. Sci.* 21, 427-438 (2010)
22. Amendola, M.A., et al., Detection of occult colovesical fistula by the Bourne test. *Am. J. Roentgenol.* 142, 715-718 (1984)

23. Niveloni, S., et al., Usefulness of videoduodenoscopy and vital dye staining as indicators of mucosal atrophy of celiac disease: assessment of interobserver agreement. *Gastrointest. Endosc.* 47, 223-229 (1998)
24. Tannous, Z., et al., Delineating melanoma using multimodal polarized light imaging. *Laser Surg. Med.* 41, 10-16 (2009)
25. Wilkinson, F., W.P. Helman, and A.B. Ross, Quantum Yields for the Photosensitized Formation of the Lowest Electronically Excited Singlet State of Molecular Oxygen in Solution. *J. Phys. Chem. Ref. Data* 22, 113-262 (1993)
26. Severino, D., et al., Influence of Negatively Charged Interfaces on the Ground and Excited State Properties of Methylene Blue ¶. *Photochem. Photobiol.* 77, 459-468 (2003)
27. Lee, S.-K. and A. Mills, Luminescence of Leuco-Thiazine Dyes. *J. Fluoresc.* 13, 375-377 (2003)
28. Junqueira, H.C., et al., Modulation of methylene blue photochemical properties based on adsorption at aqueous micelle interfaces. *Phys. Chem. Chem. Phys.* 4, 2320-2328 (2002)
29. Sykora, M., et al., Photoinduced Charge Transfer between CdSe Nanocrystal Quantum Dots and Ru-Polypyridine Complexes. *J. Am. Chem. Soc.* 128, 9984-9985 (2006)
30. Alphandery, E., et al., Highly efficient Forster resonance energy transfer between CdTe nanocrystals and Rhodamine B in mixed solid films. *Chem. Phys. Lett.* 388, 100-104 (2004)
31. Clapp, A.R., I.L. Medintz, and H. Mattoussi, Forster resonance energy transfer investigations using quantum-dot fluorophores. *Chemphyschem.* 7, 47-57 (2006)
32. Ramadurai, D., et al., Electrical and optical properties of colloidal semiconductor nanocrystals in aqueous environments. *Superlattice Microst.* 40, 38-44 (2006)
33. Artemyev, M.V., et al., Optical Properties of Dense and Diluted Ensembles of Semiconductor Quantum Dots. *Phys. Stat. Sol. (B)* 224, 393-396 (2001)
34. Zang, L.Y., Z.Y. Zhang, and H.P. Misra, EPR studies of trapped singlet oxygen (1O_2) generated during photoirradiation of hypocrellin A. *Photochem. Photobiol.* 52, 677-683 (1990)
35. Khan, A.U. and M. Kasha, Direct spectroscopic observation of singlet oxygen emission at 1268 nm excited by sensitizing dyes of biological interest in liquid solution. *Proc. Natl. Acad. Sci. USA* 76, 6047-6049 (1979)
36. Valencia, A. and J. Morán, Reactive oxygen species induce different cell death mechanisms in cultured neurons. *Free Radical Bio. Med.* 36, 1112-1125 (2004)

4. QUANTUM DOTS AS LIGHT-HARVESTING ANTENNAE

The use of fossil fuels has had many social and environmental ramifications. The start of the “petroleum era” instigated the rapid technological development of many countries. In fact, the discovery of fossil fuels has impacted our lives so much that the economic well-being of a nation is often judged on the basis of its energy use per capita. However, it has been suggested that we are rapidly approaching the end of this “petroleum era”. There are several reasons for this. The first and most fundamental one is that fossil fuels are a finite resource.

There exists a common consensus that the peak of oil production has already happened, or it will occur within the next few decades [1, 2]. As this happens, the oil will become more and more expensive while its availability will decline sharply, in contrast to increasing energy demands. This would have a dramatic impact not only on the well-established economies but also on the developing countries that require increasing amounts of energy to ensure even the most basic of services, such as clean drinking water, food supply and adequate shelter.

Secondly, the political ramifications of the country’s dependency on the oil, imported mainly from the Middle East, must not be ignored [3].

Finally, an important reason for the inevitability of the termination of the “petroleum era” is the environmental damage that the use of fossil fuels had caused. Some technological advances have been made to improve the air quality of the major metropolitan areas. However, more than likely, these improvements were counteracted by the increasing vehicle use and energy demands [3]. In fact, in 2001, the scientific opinion was that the content of the carbon dioxide gas in the atmosphere needed to be reduced by ~60% for the natural systems to be able to deal with it [4].

In recent years, several countries have introduced sustainability programs into their economic agendas, including funding for green energy initiatives. While this is an important step in addressing many of the environmental and political issues, it has been suggested that the environmental impact of the fossil fuels use is likely to remain a problem for another century.

The development of the energy production technology that is not only able to deal with the energy demands, but also can aid in the reversal of the environmental damage caused, would certainly have benefits bridging all areas of nation's well-being.

One example of such a technology is artificial photosynthesis. As mimicry of the natural photosynthesis, it has the potential to convert solar energy into electrical energy, produce hydrogen gas for fuel and high-energy organic molecules for food and plastics, while fixing the atmospheric CO₂ gas in the process. The straightforward way to construct an artificial photosynthetic device for practical solar fuel production is to mimic the structural and functional organization of the natural photosynthetic machinery. In naturally occurring photosynthetic systems, light is first absorbed by light-harvesting (LH) antennae and the absorbed energy, in the form of an exciton, is transferred to a reaction centre (RC) via Förster Resonance Energy Transfer (FRET). In the RC, the exciton is split into an electron and a hole by a dimer molecule called the "special pair". The electron is later used in chemical reactions to produce high-energy molecules that fuel the organism [5]. Mimicry of this process for artificial solar energy conversion should include, among other components, an efficient LH antenna capable of transferring the excitation energy to the RC.

This chapter describes the first attempts to replace the natural antennae of a bacterial photosynthetic system by semiconductor QDs [6]. RCs, extracted from the purple bacteria *Rhodobacter sphaeroides* and purified from the majority of naturally present LH complexes, were assembled with QDs of carefully chosen emission colours. The QD/RC complexes were then spectroscopically examined for the occurrence of energy transfer from QDs to the "special pair" of RCs. Finally, the enhancement of the photosynthetic efficiency of RCs in the presence of QDs was ascertained from the fluorescence intensity of the special pair. A three-fold increase in the rate of generation of excitons at special pair of the RC was observed experimentally, and theoretical estimates predict even stronger enhancements, paving the way for further optimization. This proposed approach to enhanced light harvesting and efficient energy transfer from QD to RC paves the way for the application of QD in artificial photosynthetic systems.

4.1. Mimicking natural photosynthesis

The development of artificial photosynthetic systems that utilize solar energy is one of the most challenging goals of chemistry and material sciences [7]. In short, the goal of artificial photosynthesis is to mimic the photosynthetic machinery and processes that nature had perfected over millions of years. This section gives a short introduction to the natural photosynthetic systems, in particular those used by bacteria, and to the strategies used to mimic these systems. The possible implications of integration of QDs with a bacterial reaction centre are also discussed.

4.1.1. Bacterial photosynthesis

In general terms, photosynthesis can be defined as a process used by organisms to convert solar energy into high-energy molecules that fuel the cellular processes necessary for organism's survival. The type and the number of photosynthetic systems used depends on the organism – plants and algae for example usually have two coupled photosynthetic systems (PSI and PSII). Anoxygenic organisms, which do not evolve oxygen, only have one photosynthetic system [8]. Purple bacteria *Rb. sphaeroides* is one of such organisms. In purple bacteria, the conversion of solar energy into high-energy molecules via photosynthesis involves the following steps [9]:

- 1) The absorption of solar photons by antennae composed of pigment-protein complexes called the light-harvesting (LH) complexes (Figure 4.1).
- 2) The transfer of the absorbed energy, in the form of an exciton, from the LH complexes to a reaction centre (RC) via FRET (Figure 4.1). The transfer usually occurs within tens of picoseconds after absorption of a solar photon [8].
- 3) The exciton is split into constituent charges (an electron and a hole) by a dimer of two bacteriochlorophyll (B) molecules – the so-called special pair (P).
- 4) The charges are spatially separated through a series of photoinduced charge transfers along the chains of the reaction centre to prevent immediate recombination [10].
- 5) The electrons are used in chemical transformations by a Cytochrome bc_1 complex and ATP-synthase to produce high-energy adenosine triphosphate (ATP) molecules that fuel the organism (Figure 4.1).

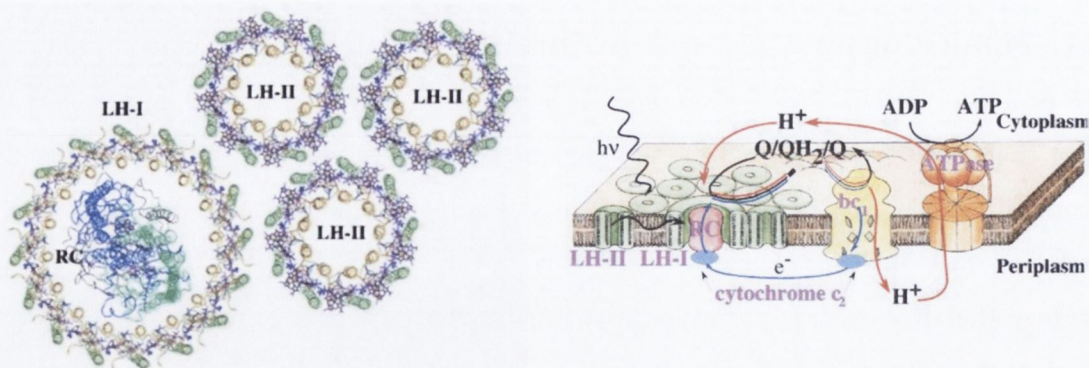


Figure 4.1| Structural composition and functionality of a bacterial photosynthetic system. The light is absorbed by the light-harvesting (LH) complexes and is transferred to the reaction centre, located inside the LH-I complex. The exciton transferred to the reaction centre is split, and the electron is transferred to the opposite side of the membrane while at the other side of the membrane the quinone (Q) is reduced to hydroquinone (QH₂). It is then used by the cytochrome bc₁ complex to oxidise the hydroquinone back to quinone and the energy released upon this reaction is used to transport a proton across the membrane, thus creating a proton concentration gradient. When the proton travels down this gradient through the ATP synthase (ATPase) enzyme, the energy released is in turn used to convert adenosine diphosphate (ADP) into adenosine triphosphate (ATP). Adapted from [9].

4.1.2. Bacterial Reaction Centres

The structure of the reaction centre of an organism is optimised for the specific environmental conditions that the organism lives in; as a result, different organisms often have structurally different reaction centres. However, all reaction centres are complexes of pigments and proteins. The reaction centre of the purple bacteria *Rb. sphaeroides* is the simplest and therefore most studied and best understood RC. It is generally accepted to be a good model for all photosynthetic reaction centres [9, 11].

In its natural environment, each RC of the purple bacteria has two membrane-spanning branches – the active branch (A) and the inactive branch (B) [12]. Each branch consists of one quinone (Q_{A/B}), one bacteriopheophytin (H_{A/B}) and one molecule of bacteriochlorophyll (B_{A/B}). The two branches are connected by two coupled bacteriochlorophyll molecules – the special pair (P or P870) (panel A of Figure 4.2). Each of the cofactors of the reaction centre (the quinone, bacteriopheophytin, bacteriochlorophyll and the special pair molecules) can be identified from the absorption spectra of a solution containing the RCs (Figure 4.2).

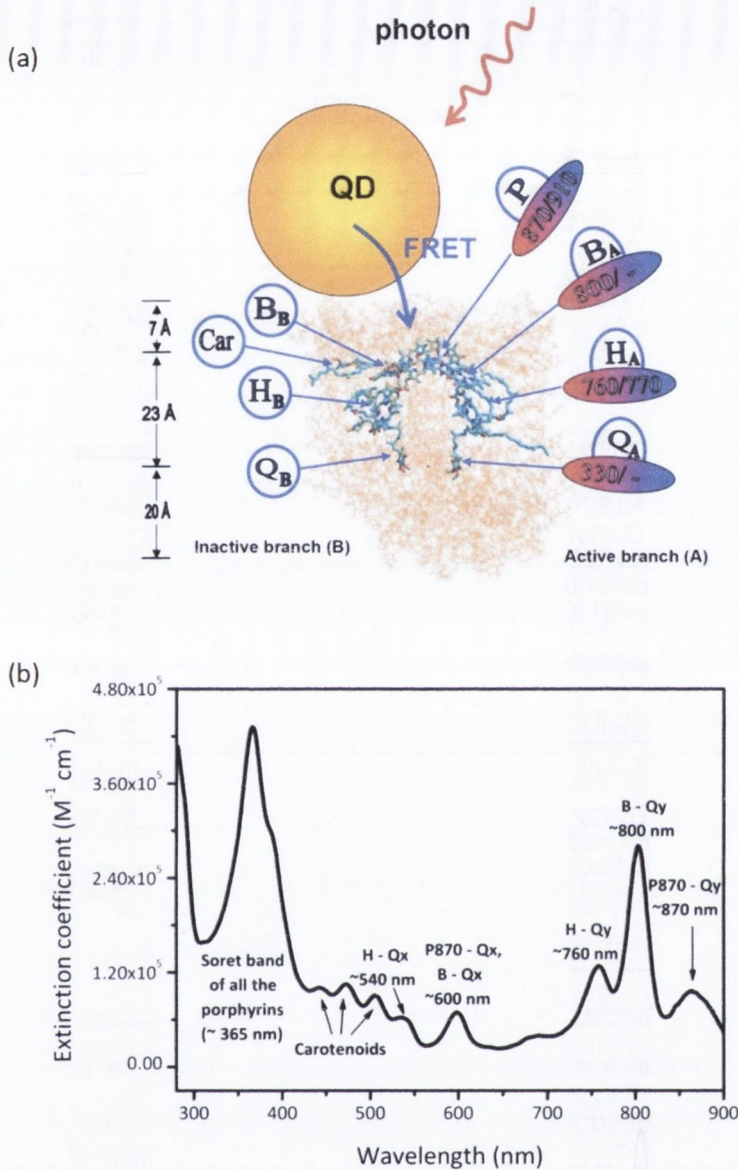


Figure 4.2] Reaction Centre/Quantum Dot system. (a) A RC purified from *Rb. Sphaeroides* is composed from the quinone ($Q_{A/B}$), bacteriopheophytin ($H_{A/B}$) and bacteriochlorophyll ($B_{A/B}$) cofactors arranged in two branches – the inactive branch B and the active branch A. The two branches are connected by a dimer of bacteriochlorophyll molecules – the special pair (P or P870). The positions of the absorption and photoluminescence bands of the cofactors (P, B, H and Q) are indicated for the active branch only. A quantum dot is assembled with the reaction centre and it transfers the energy it collects as photons to the reaction centre via Förster Resonance Energy Transfer. **(b)** The absorption bands of each cofactor are clearly distinguishable in the extinction spectra of the RC. Note that the position of the bands for the same cofactors is different for the active and inactive branch. For example, bacteriochlorophyll molecule belonging to the active branch (B-Qy) absorbs at 800 nm, while bacteriochlorophyll of the inactive branch (B-Qx) absorbs at 600 nm.

When an exciton is transferred from the LH complexes to the RC, it quickly moves towards the special pair, where it is split into an electron and a hole within 2-3 ps [13, 14]. Afterwards, the electron moves along the active branch of the reaction centre towards Q_A by a series of electron transfers. The transfer of the electron must occur in several steps as a direct transfer of the electron from the special pair to Q_A would be too energetically demanding to be able to prevent the recombination of the charges. The electron is later used by different photosynthetic machinery, eventually resulting in the synthesis of ATP [9].

4.1.3. Artificial photosynthesis

It could be imagined that the best artificial PS systems can be developed on the basis of the already well-established semiconductor photovoltaic (PV) technology. However, artificial photosynthetic (APS) devices differ greatly from the p-n junction-based PV devices. The most important difference between them is the photon absorption and charge separation processes – the fundamental properties of any solar cell. In PV devices, both of these processes occur at the same point in space – the depletion region. In APS devices, however, the two processes are decoupled and performed by different entities: photons are collected by the LH antennae and the separation of charges occurs at the reaction centre. This property of the artificial PS allows the integration of a large number of the light-absorbing elements for each reaction centre, potentially resulting in a superior collection of solar energy [15].

Many approaches to the development of APS systems are being pursued, all of which require an efficient built-in antennae for the harvesting of solar energy. To date, the best light-harvesting antennae developed are based on the arrays of porphyrin complexes of ruthenium and osmium, such as $N3^1$ and ruthenium black² complexes [16-20]. Attempts have also been made to employ organic chromophores that mimic one or more aspects of the natural light-harvesting processes, including melanin-like biomolecules [15, 21, 22] and carotenoid-porphyrin systems [23-25]. In many of above-mentioned cases efficient collection and transfer of energy was achieved. However, the use of these systems is inhibited by the lack of long-term stability and narrow light-collecting spectral windows [16, 26]. Recently, it has been suggested that inorganic nanocrystals can be used to improve the light harvesting in the APS systems [27].

Advances in inorganic synthesis enabled the production of monodispersed and highly luminescent QDs, such as CdSe/ZnS and CdTe QDs nanocrystals [28, 29]. The extinction

¹ Cis- $RuL_2(NCS)_2$, where L is 2,2'-bipyridyl-4,4'-dicarboxylic acid.

² Tri(cyanato)-2,2',2''-terpyridyl-4,4',4''-tricarboxylate Rull.

coefficients and the photostability of these QDs are significantly larger than those of organic molecules [30]. QDs have wide absorption bands resulting in very broad light-collecting windows. The spectral width and position of QDs' emission bands can be tailored to ensure best coupling with the acceptor of the energy transfer process [31]. Finally, the surface functionality of some QDs can be modified to requirements, allowing covalent attachment of these QDs to the acceptor with the aim of achieving minimum donor-acceptor separation distances [31-33].

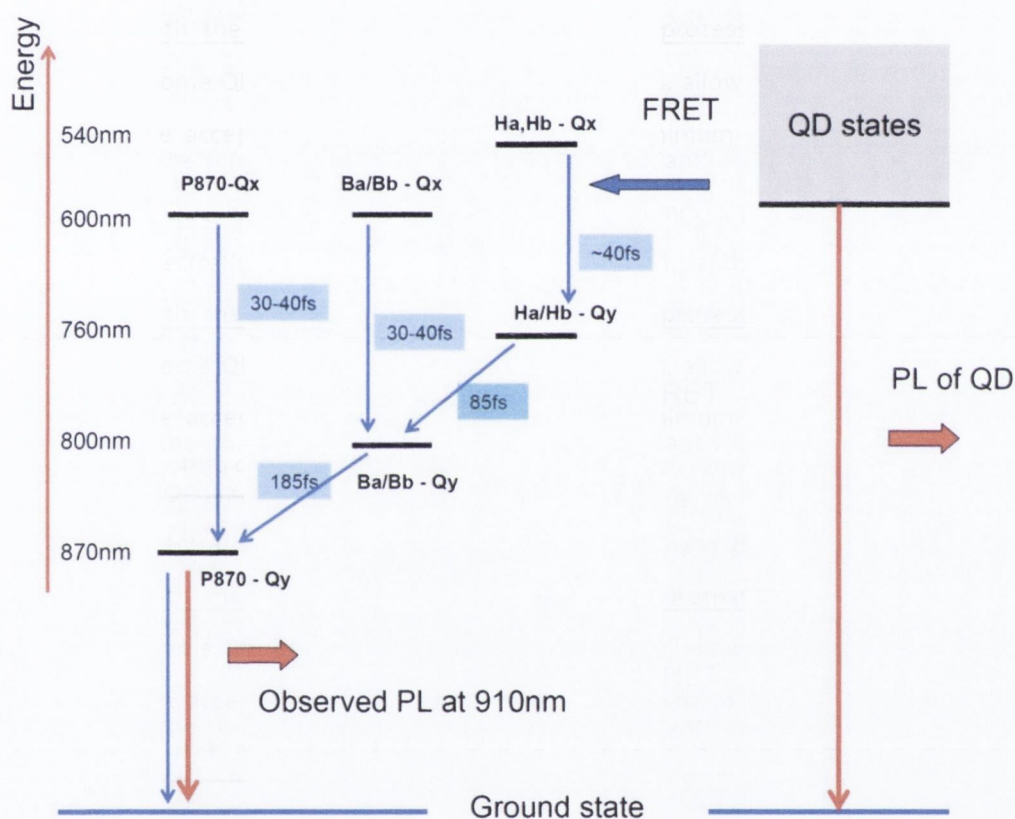


Figure 4.3 | Energy flow in Reaction Centre/Quantum Dot complexes. QDs transfers collected photon energy to any of the RC cofactors by FRET. The excitation quickly relaxes to the P870-Qy level, where the exciton is split into constituent carriers (in natural environment) or it decays with a characteristic emission at ~920 nm. The relaxation times between different levels of the RC were taken from [9].

In this study, we experimentally demonstrate the potential of semiconductor QDs to act as a light-harvesting antenna for bacterial reaction centres [6]. In order to develop an efficient FRET-based nano-bio hybrid material, the diameters (or equivalently PL colours) of QDs were carefully chosen to be optically coupled to the pigment chromophores of the RCs.

The diagram of energy relaxation (Figure 4.3) for one such nano-bio hybrid illustrates the proposed mode of action in this system. Photon energy is absorbed by QDs and is donated to one of the cofactors of RC complex by FRET. The excitation within the RC quickly decays to the lowest excited level, P870, which corresponds to exciton arriving at the special pair. Here, in its natural environment, the exciton is split into an electron and a hole. However, under the experimental conditions used, this does not occur. Instead, the exciton decays with a characteristic emission at ~ 920 nm, the intensity of which can be used to judge the potential photosynthetic efficiency of our nano-bio complexes.

4.2. Sample preparation

Sample preparation involved the extraction of the reaction centres from the *Rb. Sphaeroides* and purification of the extracted complexes from the natural light-harvesting complexes¹. The properties of extracted reaction centres differ from those observed in their natural environment, requiring an addition of a strong anti-oxidant to prevent the photooxidation of the RCs under experimental light fluxes used. CdSe/ZnS, with emissions at 530, 570 and 600 nm, and CdTe QDs emitting at 530 and 570 nm were either electrostatically assembled with or covalently attached to the extracted reaction centres.

4.2.1. Extraction and purification of RCs

The cells of wild-type nonsulfur purple bacterium *Rhodobacter sphaeroides* were grown in liquid Ormerod culture medium under anaerobic conditions in a luminostat at ~30°C for 4-6 days. Chromatophores (membranes containing photosynthetic apparatus) were isolated from sonicated cells by centrifugation and were incubated in the dark for 30 min at 4°C in 0.01 M sodium phosphate buffer (pH 7.0) containing 0.5% zwitterion detergent lauryl dimethylamine oxide (LDAO). After this, the chromatophore suspension was centrifuged (144,000g, 60 min, 4°C). The supernatant was brought to 22% saturation with a solution of ammonium sulphate. The precipitate containing RC was dissolved in 0.01 M sodium phosphate buffer (pH 7.2) containing 0.05% LDAO and subjected to chromatography on a hydroxyapatite column. These procedures were described in more detail elsewhere [34].

-The resulting RC preparation was suspended in 0.01 M sodium phosphate buffer (pH 7.2) containing 0.05% LDAO and dialyzed against 0.01 M Tris-HCl buffer (pH 7.8) containing 0.1% anionic detergent sodium cholate. Following this procedure, RC preparations were more tolerant to long-term storage at a temperature of -80°C. It should be mentioned that the detergent LDAO induced precipitation of QD from aqueous solutions and was never used in our experiments.

The purity of RC pigment-protein complexes was characterized by the ratio of intensities of UV-absorption bands of the protein at 280 nm to the absorption of bacteriochlorophyll at 800 nm. This ratio was found to vary from 1.3 to 1.4 for different RC preparations (Figure 4.2, panel B), which is only slightly higher than the value of 1.2 for absolutely pure RC [35]. This means that a small quantity of pigment impurity was present in the extracted RCs. The major

¹ The extraction and purification of RCs was performed at a laboratory of Prof. E. Lukashev at the Department of Biophysics, Lomonosov Moscow State University, Moscow, Russia. The protocols for the procedures described here were provided by E. Lukashev.

constituent of this impurity was the LH-2 complex, which absorbs at 600 nm, 800 nm and 850 nm and provides a contribution in the 400 nm to 500 nm wavelength range, where carotenoids absorb (panel B of Figure 4.3).

4.2.2. Properties of extracted RCs

The experimental conditions of the extracted RCs are very different to their natural environment. The isolated RCs suspended in water are not protected by the membrane or the pigment-protein complexes that usually surround them in the fully operational photosynthetic system. Without this natural protection, they are easily photooxidized even under illumination as weak as 0.02 mW/cm^2 [36], leading to the oxidation of the special pair dimer ($\text{P870} \rightarrow \text{P870}^+$). An addition of an antioxidant, which acts as a source of electrons, can prevent the photooxidation of the RCs.

Sodium (Na) ascorbate is a common antioxidant used for this purpose [37-39]. When added to RCs, it supplies electrons to the oxidised special pair dimer ($\text{P870}^+ \rightarrow \text{P870}$) thus creating the so-called 'closed state' of the RC ($\text{P870}/\text{Q}_\text{A}^-\text{Q}_\text{B}^-$), in which the quinones are fully reduced. The closed state of the RC is stable against photooxidation at experimental light fluxes (up to $\sim 12.5 \text{ mW/cm}^2$) and, most notably, its energy structure is very similar to the natural state of $\text{P870}/\text{Q}_\text{A}\text{Q}_\text{B}$ of the bacterial reaction centre [36]. Furthermore, the full reduction of the quinones means that no additional electrons can be accepted by these molecules. As a result, the electrons and holes are not separated at the special pair. Instead they recombine from the $\text{P870}-\text{Q}_\text{y}$ level, giving rise to an emission band centred at $\sim 920 \text{ nm}$ (Figure 4.4).

The reversal of the photooxidation of the RCs by Na-ascorbate can easily be monitored spectroscopically (Figure 4.4). As the concentration of Na-ascorbate is increased, an increase of the 870 nm absorbance peak is observed (panel A of Figure 4.4), corresponding to the reduction of the oxidised special pair dimer ($\text{P870}^+ \rightarrow \text{P870}$). Consequently, the emission of P870 at 920 nm also increases (panel B of Figure 4.4). Both processes achieve saturation at 10 mM concentration of Na-ascorbate in the RCs-containing solution.

The PL peak centred at $\sim 860 \text{ nm}$ (Figure 4.4, panel B) belongs to the residual amounts of the LH-II complexes, left over after the RC purification procedure. The intensity of this peak is comparable to that of the P870 PL peak. However, the quantum yield of the LH-II complex is much higher than that of the P870 emission, even in the closed-state of RCs. So the amount of LH-II complexes left over is actually very small and is of the order of 1 in 1000 RCs. The emission of LH-II complexes decreases upon the addition of Na-ascorbate because the

formation of the RCs' closed state permits the energy transfer from LH-II complexes to the RC and consequently allows for an addition pathway of exciton decay within LH-II complexes.

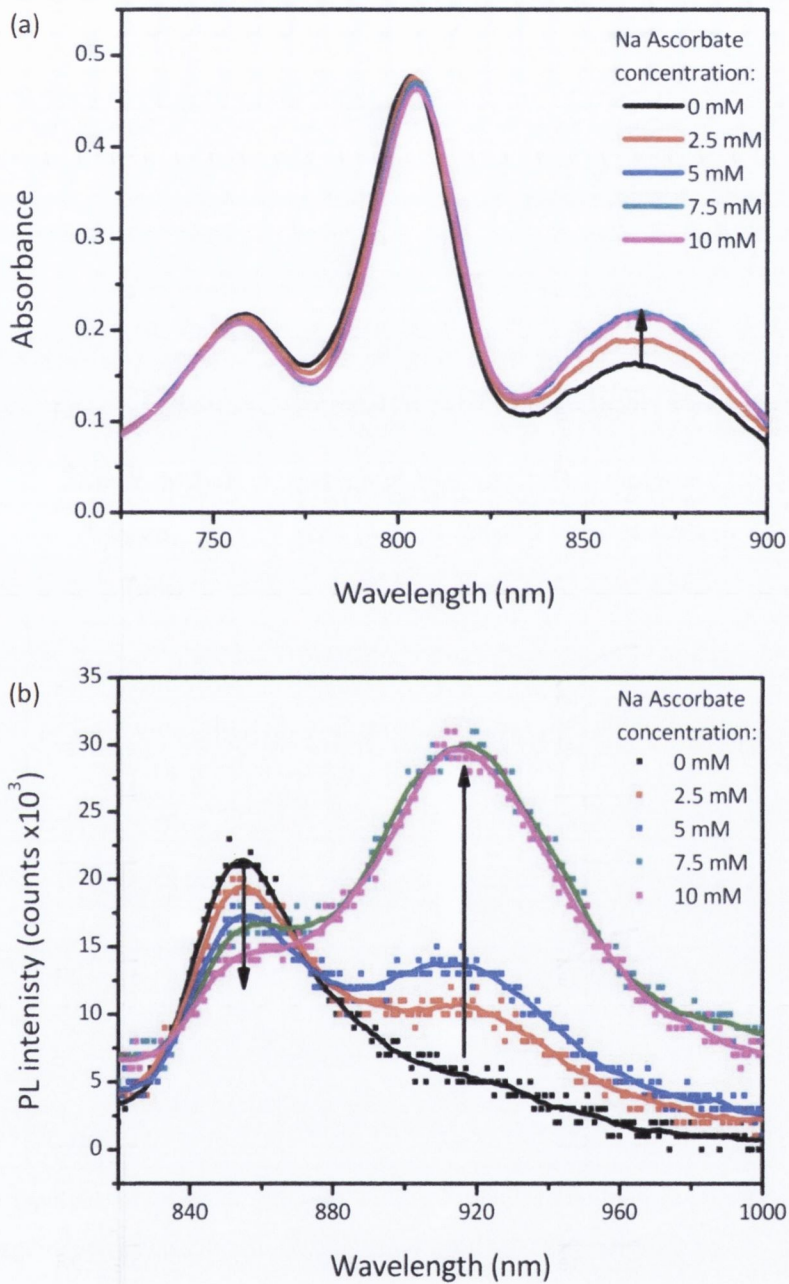


Figure 4.4| Reversal of Reaction Centres' photooxidation by sodium (Na) ascorbate. Na-ascorbate was added to a solution of photooxidised RCs. As the concentration of Na-ascorbate was increased, corresponding increases in **(a)** the absorbance peak (870 nm) and **(b)** the photoluminescence peak (~ 920 nm) of the reduced P870 were observed. The PL peak at ~ 860 nm is due to the residual amount of LH-II complexes in the extracted RCs.

4.2.3. RC/QD assembly

Two types of QDs were used to form the QD/RC complexes: TGA-stabilised CdTe QDs, which have a very thin ligand layer and no inorganic shell, and core-shell CdSe/ZnS QDs treated with DL-cystein (Cys) or, in some cases, solubilised in aqueous solutions using a mixture of tri-functional thiol-containing polyethylglycol (PEG) molecules terminated by carboxylic, hydroxyl and amino groups. The main QDs utilised were TGA-CdTe QDs and Cys-CdSe/ZnS QDs as these QDs had the smallest diameters, which is a valuable property for a FRET-based system. These QD samples and some of their primary characteristics are summarised in Table 4.1 and Figure 4.5.

Table 4.1| Physicochemical properties of the main Quantum Dots used in the nano-bio hybrids: CdSe/ZnS QDs treated with DL-Cystein (Cys) and CdTe QDs stabilised by Thioglycolic Acid (TGA).

QD sample	PL emission maximum (nm)	Quantum Yield (%)	Diameter* (nm)	Hydrodynamic Diameter** (nm)	Zeta Potential (mV)
Cys-QD530 (CdSe/ZnS)	533	41	2.5	4.6 ± 1.4	-29.2
Cys-QD570 (CdSe/ZnS)	570	49	3.1	5.8 ± 1.8	-33.4
Cys-QD600 (CdSe/ZnS)	599	32	4.6	9.1 ± 2.3	-37.5
QD530 (CdTe)	535	28	2.0	4.2 ± 1.2	-38.0
QD570 (CdTe)	569	30	2.7	5.1 ± 1.6	-44.0

* Diameters refer only to the inorganic core of the CdTe QDs, and include the inner CdSe core and the ZnS shell (0.5 nm) for CdSe QDs. For both types of QDs, the thickness of the ligand shell is not included.

** Hydrodynamic diameters were measured using Dynamic Light Scattering technique (NanoZS, Malvern).

RC/QD complexes were prepared either by a covalent attachment of QDs to the end-groups of the RC complex or via self-assembly of RCs and QDs in aqueous solution. The covalent

attachment was accomplished using carbodiimide chemistry¹, in which COOH-groups of QDs react with the NH₂-groups of RCs thus forming a peptide bond. The self-assembly of RC/QD complexes involved addition of varying amounts of RCs to 0.5 μ M solutions of QD diluted in 10 mM Na-ascorbate buffer (pH6.8). The amount of RCs added determined the final RC to QD molar ratio of the formed complexes. After addition of RCs to QD solutions, the mixtures were allowed to self-assemble under gentle agitation for 30 minutes at ambient conditions.

Both covalent and self-assembled RC/QD complexes were purified by gel filtration through a Superdex 200 resin (GE Healthcare) columns equilibrated with 10 mM Na-ascorbate buffer. All collected fractions were analysed by UV-vis spectroscopy with the aim of accurately determining the RC to QD molar ratios of the samples utilising the least-squares deconvolution of the absorption spectra of RC/QD complexes into constituent (RC and QD) contributions (as described in Chapter 2). Only samples containing RC-QD complexes (i.e. non-zero RC to QD molar ratios) were used for further experiments.

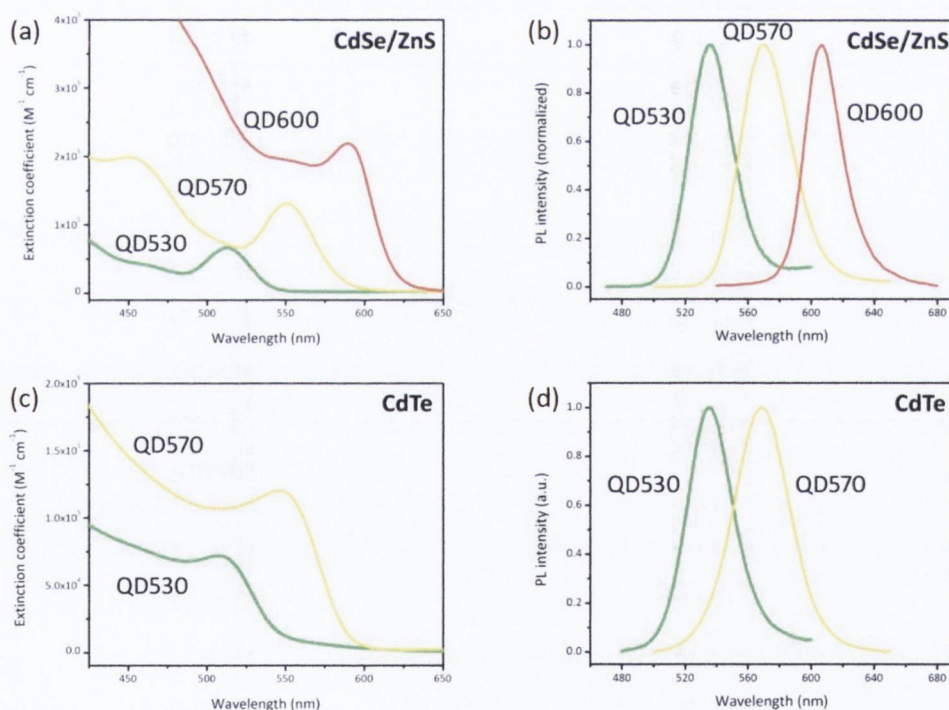


Figure 4.5| Optical spectra of QDs utilized in RC/QD complexes. Figure shows the absorption (a, c) and fluorescence (b, d) spectra of the main QD samples used for formation of RC/QD complexes: Cys-stabilised CdSe/ZnS QDs (top row) and TGA-stabilised CdTe QDs (bottom row).

¹ Covalent attachment of QDs to RCs was performed by Dr. A. Sukhanova (Université de Reims Champagne-Ardenne, France).

4.3. Energy transfer in QD/RC complexes

In a hybrid RC/QD material operating in the FRET regime, any QDs samples emitting in the 530 – 600 nm range can be used. However, as can be seen from the diagram of energy relaxation within RC (Figure 4.3), QDs of certain sizes, which have strong coupling to RC cofactors, will perform best. In particular, we selected CdTe QDs samples with emission bands centred at ~530 nm and ~570 nm and CdSe QDs with emissions at ~530 nm, ~570 nm and ~600 nm (Table 4.1). Once assembled, RC/QD complexes were characterised in terms of the energy transfer efficiency from QDs and RCs by a series of spectroscopic measurements. The investigations show that although the RC have their own chromophores with a significant absorption cross section, properly designed QD can easily dominate over the intrinsic absorption of the RC (Figure 4.6).

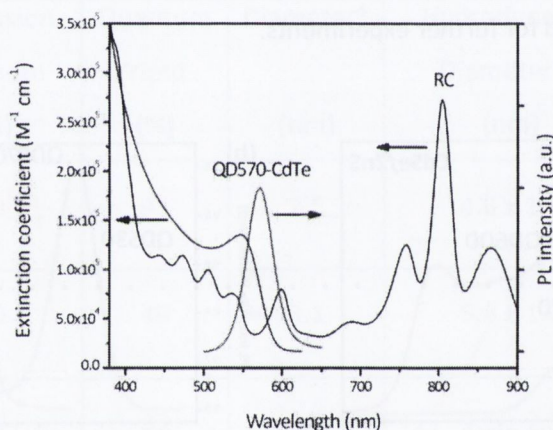


Figure 4.6] Comparison of optical properties of RCs and QD570-CdTe. The extinction coefficient of QD570 dominates over the intrinsic absorption of RCs in the 400 – 570 nm spectral region. The high extinction coefficient of RCs ensures sufficient coupling between QD570 PL band and RC absorption for efficient energy transfer to occur. Both of these facts suggest that optical enhancement of RC excitation is possible in RC/QD complexes.

4.3.1. Photoluminescence of self-assembled complexes

Self-assembly with different CdSe/ZnS and CdTe QDs was performed at increasing RC concentrations to provide variations of the RC to QD ratio in the final complexes. As a result of complex formation, the intensity of QDs' emission was significantly decreased (Figure 4.7). Such quenching of QDs' fluorescence was found to be dependent on the RC-QD ratio, as is expected in the case of a FRET-based system – the increased number of RCs in a complex is equivalent to a larger number of FRET-acceptors being available to accept the energy from excited QDs.

It was found that quenching was more efficient for CdTe QDs compared to CdSe QDs, since smaller numbers of RCs were necessary to quench QDs' PL by the same amount. Similar deduction can be applied to the emission of QD600-CdSe QDs, which is least efficiently quenched by RCs. Both of these facts can be attributed to the distance-dependence of the FRET process. Within the standard theory, the FRET efficiency (E) for a complex consisting of one QD and one RC ("QD₁-RC₁") is strongly dependent on the RC-QD separation:

$$E = \frac{1}{1 + (R/R_0)^6} \quad (4.1)$$

where R_0 is a Förster radius for a specific RC/QD complex. One can see that FRET is efficient if $R \leq R_0$. The minimum separation distances of the RCs and QDs in the self-assembled complexes can be estimated as $(D_{RC} + D_{QD})/2$, where D_{RC} was taken to be the X-ray diameter of the RCs (=5 nm, [35]). The minimum separation distances and the Förster radii of the RC/QD complexes described here are summarised in Table 4.2. In short, CdTe QDs have smaller radii (Table 4.1) and thinner ligand shells than CdSe/ZnS QDs, so smaller RC-QD separations are achievable (Table 4.2). Similarly, QD600-CdSe QDs are much larger than QD530 and QD570 QDs, and have significantly larger thickness of the stabilising cystein shell, resulting larger separation distances and significantly decreased the efficiency of PL quenching.

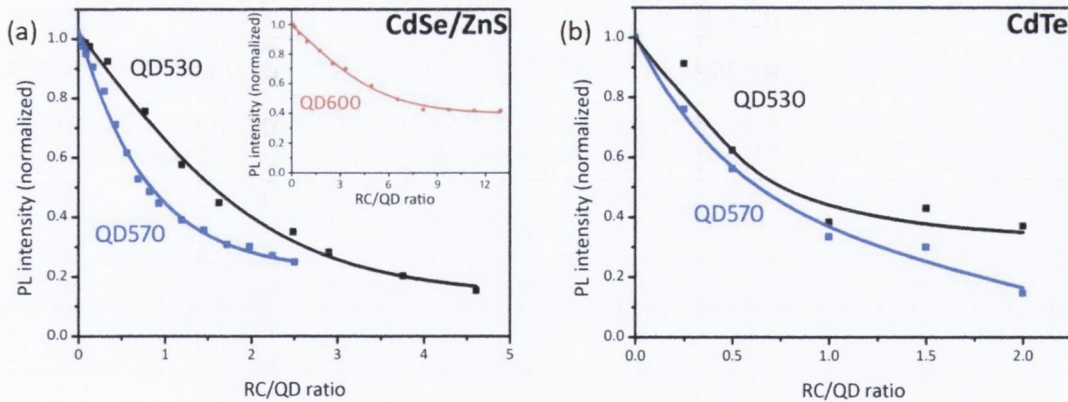


Figure 4.7 | Photoluminescence titration curves for (a) CdSe/ZnS and (b) CdTe QDs. QDs photoluminescence is quenched by RCs. The efficiency of PL quenching is greater for CdTe QDs than for CdSe QDs. The PL of QD600-CdSe was found to be least efficiently quenched (inset of panel (a)), attributed to the large QD diameter and thickness of the polymer shell resulting in large RC-QD separation distance.

It was also interesting to see whether the charge of the QDs' surface affects the self-assembly of the RC-QD complexes and the resulting FRET efficiency¹. In order to do this, QDs of similar sizes (or emission wavelengths) were encapsulated with mixtures of PEG-derived molecules – the ratio of these molecules in the reaction determined the resulting surface charge (Table 4.3). These QDs were self-assembled with equal amounts of RCs (2.8 RCs per QD). At the end of the assembly process, the quenching of QDs PL was measured and found to be most efficient for QDs samples with most negative surface charge (Table 4.3). Most likely this is due to the stronger electrostatic attraction between the QDs and the positive groups of the RCs. Note that, although the surface charge of these QDs was in some cases similar to that of the Cys-stabilised CdSe/ZnS QDs and TGA-stabilised CdTe QDs, the quenching efficiency of these QDs was never more than 35%, compared to the quenching efficiency of ~90% for QD570-cys-CdSe and QD570-CdTe. This is because PEG molecules are much larger than Cys or TGA molecules, resulting in much thicker polymeric shells surrounding the QDs.

Table 4.2] Comparison of Förster Radii (R_0) and minimum RC-QD separation distances of RC/QD complexes. The R_0 values are larger for CdSe QDs than for CdTe QDs because they have larger QYs (Table 4.1). The minimum separation distances were calculated using $(D_{QD} + D_{RC})/2$, where D_{RC} is 5 nm [35]. The QD diameters (D_{QD}), taken from Table 4.1, did not include the thickness of the ligand shell. However, $R_{min} < R_0$ for all QD samples, making it possible to achieve efficient energy transfer from QDs to RCs.

QD sample	Förster Radius*, R_0 (nm)	Minimum Separation, R_{min} (nm)	QD sample	Förster Radius*, R_0 (nm)	Minimum Separation, R_{min} (nm)
QD530-CdSe	5.8	3.75	QD530-CdTe	5.4	3.5
QD570-CdSe	5.9	4.05	QD570-CdTe	5.3	3.85
QD600-CdSe	6.0	4.8			

* The Förster radii were calculated according to equations 1.2 and 1.3 (Chapter 1).

¹ Surface functionalization of these QDs and corresponding PL quenching measurements were performed by A. Sukhanova (Université de Reims Champagne-Ardenne, France).

Table 4.3| Physicochemical properties and efficiency of PL quenching by RCs for PEG-encapsulated CdSe/ZnS QDs.

QD surface functionality	PL emission maximum (nm)	Zeta potential (mV)	Quenching efficiency by RCs (%)
90%PEG-OH + 10%PEG-COOH	568	-18.0	20
90%PEG-OH + 40%PEG-COOH	568	-20.4	24
30%PEG-OH + 70%PEG-COOH	567	-28.1	25
100%PEG-COOH	566	-36.0	35
100%-PEG-NH ₂	573	+32.0	NA*
50%-PEG-NH ₂ + 50%PEG-OH	571	+18.4	NA*
30%-PEG-NH ₂ + 70%PEG-OH	570	+3.6	NA*

* Addition of RCs to positively charged QDs provoked irreversible QD aggregation.

4.3.2. Covalently linked complexes

PEG-COOH encapsulated CdSe/ZnS QDs, emitting at 530 nm or 570 nm, were conjugated with RCs using carbodiimide chemistry¹. The absorption spectra of the two resulting RC-QD conjugates were deconvoluted into contributions from QDs and RCs utilizing the least-squares fitting technique (Panel c, Figure 4.8). The deconvolution yielded the approximate concentrations of QDs and RCs in these conjugates (Table 4.4). Using these concentrations, self-assembled complexes containing QD530 and QD570 were also prepared. The absorption spectra of the self-assembled complexes were found to be very similar to the corresponding spectra of chemical conjugates (panels A and B of Figure 4.8 respectively) confirming similar compositions of the two types of samples. Only a small deviation was observed in the region of the P870-Qy peak, which relates only to the oxidation state of the RCs, and not to the concentration of RCs in the RC/QD complexes.

The chemical conjugation of QDs to RCs achieves the minimal possible RC/QD separation distances, since the electrostatic repulsion between negatively-charged QDs and the negative groups of the RCs is by-passed. Therefore, even though the RC to QD ratios are same, a difference in the efficiency of FRET is expected for the two types of complexes. This was found to be indeed the case – an increase in the efficiency of the fluorescence quenching was observed when QDs PL intensities within the self-assembled and chemically-conjugated complexes were compared to emission intensities of pure QDs solutions of appropriate

¹ Chemical conjugation was performed by Dr. A. Sukhanova.

concentrations. ~35 and ~18 fold enhancements in PL quenching efficiency were obtained for QD530/RC and QD570/RC conjugates respectively (panel D of Figure 4.8, Table 4.4).

Table 4.4| Composition of QDs/RCs conjugates and corresponding photoluminescence quenching efficiencies. The concentration of QDs and RCs in the RC/QD conjugates were determined by least squares deconvolution of the corresponding absorption spectra.

Conjugate	QDs concentration (μM)	RCs concentration (μM)	RC/QD ratio	Quenching efficiency (%)		
				SA*	CC**	SA/CC factor
QD530/RC	0.60	0.22	0.37	1.0	34.8	34.8
QD570/RC	0.12	0.18	1.5	1.2	21.7	18.0

* SA = Self-Assembled complexes; ** CC = Chemical Conjugates

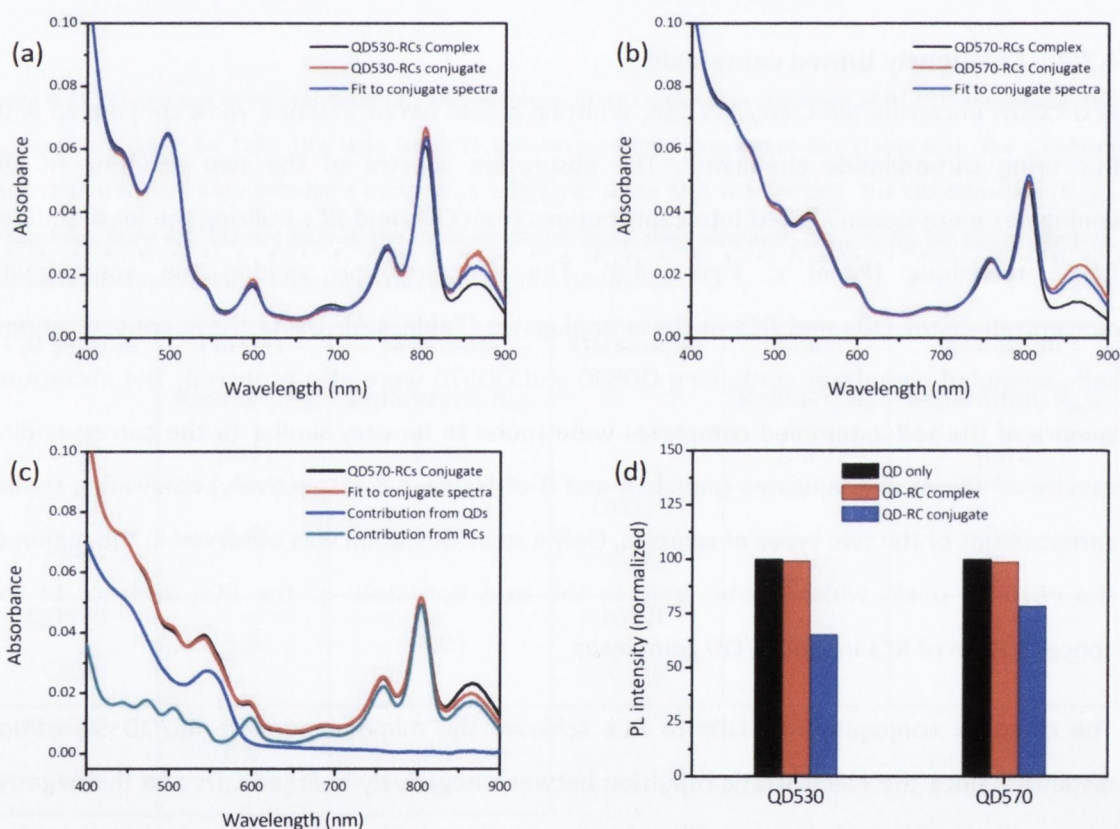


Figure 4.8| Comparison of self-assembly and chemical conjugation as methods of preparation of RC/QD complexes. The absorption spectra of self-assembled and conjugated complexes of RCs with (a) QD530 and (b) QD570 only differ around the P870-Qy peak, indicating that the overall QD and RC concentrations within these complexes are equal. (c) The concentrations of RC and QDs in the conjugated complexes were determined by deconvolution of absorption spectra into RC and QD contribution using least-squares analysis. (d) For both QD samples, the quenching of QDs' fluorescence by RCs was much more significant for RC/QD conjugates.

4.3.3. Time-resolved PL measurements

In all of above discussions, it was assumed that the assembled RC/QD complexes operated in FRET regime, i.e. the observed quenching of fluorescence was due to the transfer of energy from QDs (donors) to RCs (acceptors). Such an assumption can easily be corroborated experimentally since a key signature of FRET is a decrease of donor's (QDs') lifetime.

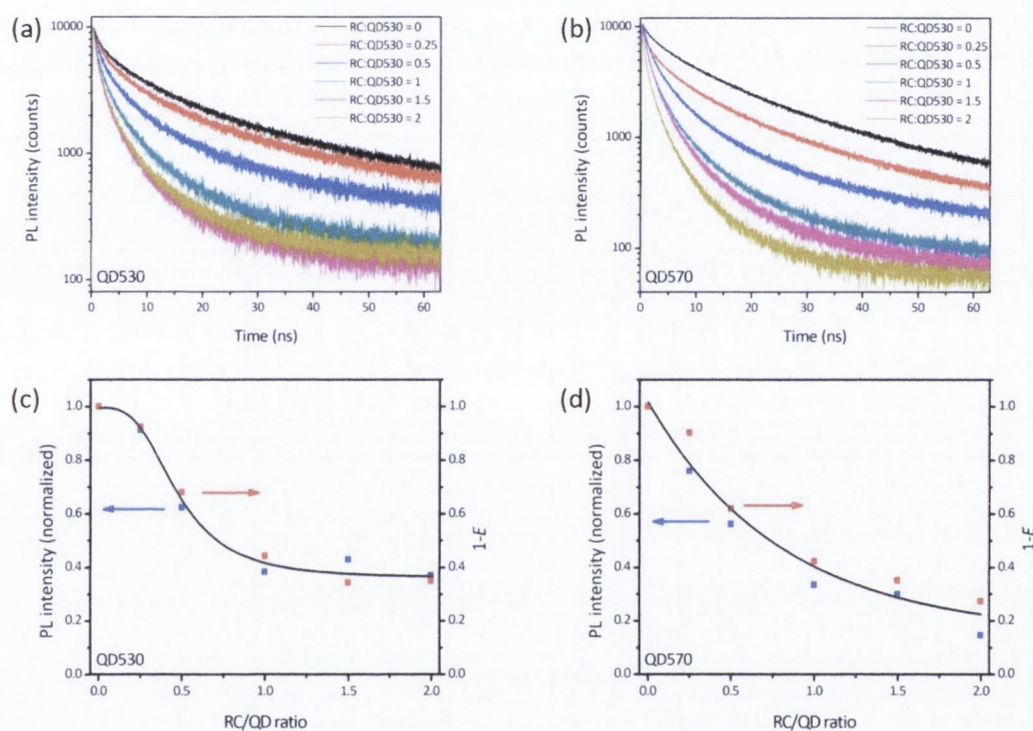


Figure 4.9| Time-resolved measurements of CdTe QDs' fluorescence in RC/QD complexes. Fluorescence decay kinetics of (a) QD530 and (b) QD570 were measured until 10,000 photons were detected. A shortening of the average lifetime, calculated from fits to data, was observed for both QDs as increasing RC/QD ratios. The relative decrease in lifetime was used to calculate the expected decrease of (c) QD530 and (d) QD570 emission due to FRET ($= 1 - E = \tau_{RC+QDs}/\tau_{QD}$). Very good correlation was observed between $1 - E$ values (blue squares) and the experimentally observed quenching of QDs' fluorescence (red squares).

Time-resolved measurements of QDs' fluorescence decays showed such a shortening of the lifetime for both TGA-CdTe QDs (Figure 4.9, panels A and B) and Cys-CdSe QDs (data not shown). Multi-exponential fits¹ to the PL decay curves yielded the average lifetimes of QDs as a

¹ The energy transfer process represents an additional term in the kinetic rate equation of the decay of donor's excitation ($\exp(-t^{1/2})$ dependence for 3D random system). It should be noted that the energy transfer rates are similar to donor's decay rates in QD-based systems (see equation 1.1), and so the change of the donor's average lifetime provides a measure of the efficiency of the energy transfer process. As a result, fitting of the decay data with simple double-exponential curves was sufficient.

function of RC/QD ratio. The efficiency of FRET in these complexes can be expressed in terms of the relative decrease of QDs' lifetime:

$$E = 1 - \frac{\tau_{QD+RC}}{\tau_{QD}} \quad (4.2)$$

where τ_{QD+RC} and τ_{QD} are the lifetimes of the QDs in complexes and in a pure QD solution respectively.

Once the efficiency of FRET in a given complex is known, it is possible to calculate the expected relative decrease of QDs' fluorescence (I_{RC+QD}/I_{QD}) due to the energy transfer process:

$$\frac{I_{RC+QD}}{I_{QD}} = 1 - E = \frac{\tau_{RC+QD}}{\tau_{QD}} \quad (4.3)$$

Significantly, a very good agreement existed between the experimental and calculated values of I_{RC+QD}/I_{QD} . For example, upon formation of a complex containing ~0.5 RCs per CdSe QD, the fluorescence of QD570 decreased by ~0.53, while the corresponding lifetime decreased by ~0.49. Similarly, the experimental quenching factors for CdTe QDs were in good agreement with the calculated values (panels C and D of Figure 4.9). These data indicate that FRET is the main mechanism of QDs' PL quenching, thereby validating the assumption made above.

4.3.4. Special pair emission in QD/RC complexes

The final set of experiments on this system involved evaluation of the most important causal effect of the energy transfer from QDs to RCs – the enhancement of the special pair emission. As discussed previously, under the experimental conditions used, emission from P870-Qy can be directly related to the potential photosynthetic efficiency of the system. Special pair fluorescence has a characteristic peak centred at ~920 nm in the near infra-red (NIR). The enhancement of P870 emission can be defined as

$$A_{920\text{ nm}}(\lambda_{exc}) = \frac{I_{QD+RC}(920\text{ nm})}{I_{RC}(920\text{ nm})} = \frac{n_{QD+RC}}{n_{RC}} \quad (4.4)$$

where λ_{exc} is the excitation wavelength, I_{QD+RC} and I_{RC} are the integrated intensities of the 920nm PL peak for the RC/QD complex and individual RCs, and n_{RC} and n_{QD+RC} are the numbers of electron-hole pairs generated at the special pair in RCs and in the RC/QD complexes, respectively. It was found that direct evaluation of $A_{920\text{ nm}}(\lambda_{exc})$ was not possible since the NIR PL spectra of RC/QD complexes contained contributions from both RCs and QDs (panel A of Figure 4.10). In fact, in some cases, the QDs' contribution far outweighed that of

the RCs. It was therefore necessary to deconvolute the NIR PL spectrum of each complex into QD and RC contributions. QD contribution was then subtracted from the RC/QD spectrum and the integrated area under the resulting peak ($\int (PL_{RC+QD} - PL_{QD}) d\lambda$) was compared to the integrated NIR PL spectra of a RC solution ($\int PL_{RC} d\lambda$) of corresponding concentration (panel B of Figure 4.10):

$$A_{920\text{ nm}} = \frac{I_{RC+QD}}{I_{RC}} = \frac{\int (PL_{RC+QD} - PL_{QD}) d\lambda}{\int PL_{RC} d\lambda} \quad (4.5)$$

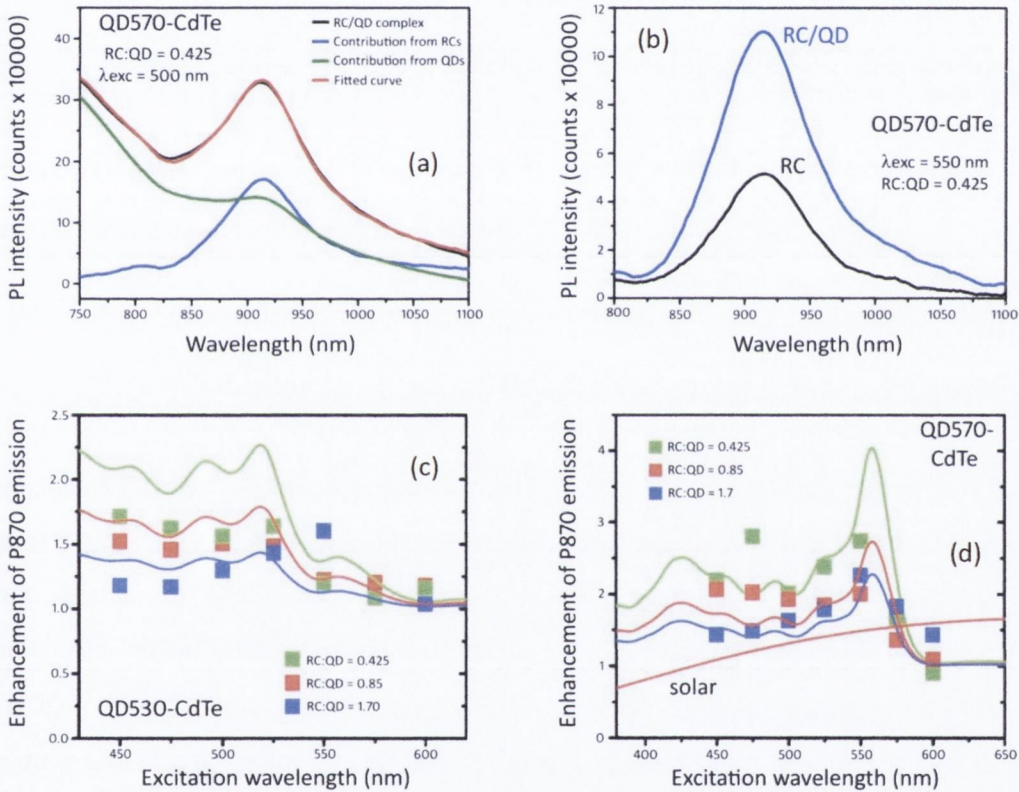


Figure 4.10| Enhancement of P870 emission in RC/QD complexes. (a) An example of Near Infra-Red (NIR) PL spectrum deconvolution of 0.425 RC/QD70-CdTe complex (black line) into contributions from RCs (blue line) and QDs (green line) using least-squares analysis. The fitted curve is shown in red. (b) Enhancement of RCs' emission upon assembly with QD570-CdTe. The ratio of the integrated areas under these peaks is the enhancement factor A (see main text). (c) and (d) Enhancement of P870 emission as a function of excitation wavelength and RC to QD ratio for complexes containing QD530-CdTe and QD570-CdTe respectively. Scatter points are the experimentally-determined values of $A_{920\text{ nm}}$, and solid lines are values calculated according to equation 4.6.

As can be seen from the scatter points in panels C and D of Figure 4.10, the experimentally determined factors $A_{920\text{ nm}}(\lambda_{exc})$ were larger than unity for wavelengths below the first excitonic absorption peak of QDs (i.e. $\lambda_{exc} \leq \lambda_{QD,exciton}$). Therefore, the number of electron-hole pairs arriving to the special pair of the RC is increased upon addition of QDs to the system due to FRET coupling. The complex QD570-RC shows stronger enhancement (up to 3 fold at $\lambda_{exc} = 550\text{ nm}$) than QD530-RC (panels D and C of Figure 4.10 respectively), which is attributed to the larger absorption of QD570 (Figure 4.5, panel C). The highest $A_{920\text{ nm}}$ values were obtained at smallest RC/QD molar ratio ($RC:QD = 0.425$) because largest number of QDs can interact with a single RC and, therefore, more energy can be transferred from QDs to a single RC. Kinetically, energy transfer interactions between multiple QDs and a single RC are possible because the lifetime of the exciton at the special pair (P870) is very short (few hundred picoseconds).

To support the above explanations and as a consistency check, the enhancement factor $A_{920\text{ nm}}$ was calculated using experimental extinctions and FRET efficiencies from a simple rate model proposed by Prof. A. Govorov¹:

$$A_{920\text{ nm}}(\lambda_{exc}) = 1 + E \cdot \frac{A_{QD}(\lambda_{exc})}{A_{RC}(\lambda_{exc})} = 1 + E \cdot x \cdot \frac{\varepsilon_{QD}(\lambda_{exc})}{\varepsilon_{RC}(\lambda_{exc})} \quad (4.6)$$

where A_{QD} and A_{RC} are the absorbances of QD and RC, ε_{QD} and ε_{RC} are the corresponding extinction coefficients, and x is the QD/RC molar ratio. The solid lines in panels C and D (Figure 4.10) are the results of theoretical calculations of $A_{920\text{ nm}}$ according to equation 4.6. The experimentally observed trends in $A_{920\text{ nm}}$ were reproduced well by these calculations, in particular, the $A_{920\text{ nm}}$ increase for $\lambda_{exc} \leq \lambda_{QD,exciton}$ and for smaller RC to QD ratios. Theoretical calculations predict even higher enhancement values than those observed experimentally.

¹ The derivation of the expression for $A_{920\text{ nm}}$ values was performed by Prof. A. O. Govorov (Department of Physics and Astronomy, Ohio University Athens, USA) and can be found in the supplementary information of [6].

4.4. Conclusions

This study represents the first successful demonstration of the energy transfer from semiconductor quantum dots to a complex biological system – the bacterial reaction centre. This opens new possibilities for the utilization of QDs as light-harvesting antennae in artificial photosynthetic systems, which can have a significant impact on the energy-related technologies. Further optimization of this nano-bio photosynthetic system can increase the potential impact of these findings.

For example, in QD/RC complexes, the emission of the special pair (P870) molecule in a RC was enhanced for excitations across the visible wavelength range. While some of the available solar photons are within this range, a significant portion of the solar energy falls within the near infra-red region. In addition, QDs used in this study had relatively small radii, which is advantageous in achieving smallest possible donor-acceptor separations. However, small QDs have moderate absorptions and little spectral overlap with the available solar energy. The utilization of semiconductor nanowires or nanorods, which have significantly larger extinction coefficients across much broader wavelength ranges, presents an opportunity for the necessary optimization of the nano-bio hybrid system described here.

References

1. Deffeyes, K.S., *Hubbert's Peak: The Impending World Oil Shortage*. Princeton University Press, New Jersey (2001)
2. Holmes, B. and N. Jones, *Brace yourself for the end of cheap oil*. New Scientist **179**, 9-11 (2003)
3. Lowe, I., *Artificial Photosynthesis: Social and Political Issues*, in *Artificial Photosynthesis* (Eds.: A.F. Collings and C. Critchley). pp. 1-12. Wiley-VCH Verlag GmbH & Co. KGaA (2006)
4. *Intergovernmental panel on climate change: third assesment report* (2001)
5. Blankenship, R.E., *Molecular mechanisms of photosynthesis*. Blackwell Science, Oxford (2002)
6. Nabiev, I., et al., *Fluorescent Quantum Dots as Artificial Antennas for Enhanced Light Harvesting and Energy Transfer to Photosynthetic Reaction Centers*. Angew. Chem. Int. Edit. **49**, 7217-7221 (2010)
7. Collings, A.F. and C. Critchley, eds. *Artificial photosynthesis: from basic biology to industrial application*. WILEY-VCH, Weinheim, (2005)
8. Prasad, P.N., *Photobiology*, in *Introduction to Biophotonics* (Eds.: P.N. Prasad). pp. 159-202. John Wiley & Sons, Inc., Hoboken, NJ, USA (2004)
9. Hu, X., et al., *Architecture and mechanism of the light-harvesting apparatus of purple bacteria*. Proc. Natl. Acad. Sci. USA **95**, 5935-5941 (1998)
10. Gust, D., T.A. Moore, and A.L. Moore, *Mimicking Bacterial Photosynthesis*, in *Artificial Photosynthesis* (Eds.: A.F. Collings and C. Critchley). pp. 187-210. Wiley-VCH Verlag GmbH & Co. KGaA, Weinheim (2006)
11. Heathcote, P., P.K. Fyfe, and M.R. Jones, *Reaction centres: the structure and evolution of biological solar power*. Trends Biochem. Sci. **27**, 79-87 (2002)
12. Allen, J.P., et al., *Structure of the reaction center from Rhodobacter sphaeroides R-26: the cofactors*. Proc. Natl. Acad. Sci. USA **84**, 5730-5734 (1987)
13. Kirmaier, C. and D. Holten, *Primary photochemistry of reaction centers from the photosynthetic purple bacteria*. Photosynth. Res. **13**, 225-260 (1987)
14. Du, M., et al., *Femtosecond spontaneous-emission studies of reaction centers from photosynthetic bacteria*. Proc. Natl. Acad. Sci. USA **89**, 8517-8521 (1992)
15. Meredith, P., et al., *Broadband Photon-harvesting Biomolecules for Photovoltaics*, in *Artificial Photosynthesis* (Eds.: A.F. Collings and C. Critchley). pp. 35-65. Wiley-VCH Verlag GmbH & Co. KGaA, Weinheim (2006)
16. Gust, D., T.A. Moore, and A.L. Moore, *Mimicking Photosynthetic Solar Energy Transduction*. Acc. Chem. Res. **34**, 40-48 (2000)
17. Balzani, V., A. Credi, and M. Venturi, *Photochemical Conversion of Solar Energy*. ChemSusChem **1**, 26-58 (2008)
18. Péchy, P., et al., *Engineering of Efficient Panchromatic Sensitizers for Nanocrystalline TiO₂-Based Solar Cells*. J. Am. Chem. Soc. **123**, 1613-1624 (2001)
19. Kodis, G., et al., *Efficient Energy Transfer and Electron Transfer in an Artificial Photosynthetic Antenna-Reaction Center Complex†*. J. Phys. Chem. A **106**, 2036-2048 (2002)
20. Odobel, F., et al., *Porphyrim dyes for TiO₂ sensitization*. J. Mater. Chem. **13**, 502-510 (2003)
21. Prota, G., *Melanins and melanogenesis* Academic Press, San Diego (1992)
22. Lawrie, K.J., P. Meredith, and R.P. McGeary, *Synthesis and Polymerization Studies of Organic-Soluble Eumelanins*. Photochem. Photobiol. **84**, 632-638 (2008)

23. Gust, D., et al., *Triplet and singlet energy transfer in carotene-porphyrin dyads: role of the linkage bonds*. J. Am. Chem. Soc. **114**, 3590-3603 (1992)
24. Ishizaki, K., O. Nikaido, and H. Takebe, *Photoreactivation of ultraviolet light-induced sister chromatid exchanges in potorous cells*. Photochem. Photobiol. **31**, 277-279 (1980)
25. Bensasson, R.V., et al., *Mimicry of antenna and photo-protective carotenoid functions by a synthetic carotenoporphyrin*. Nature **290**, 329-332 (1981)
26. Alstrum-Acevedo, J.H., M.K. Brennaman, and T.J. Meyer, *Chemical approaches to artificial photosynthesis*. Inorg. Chem. **44**, 6802-6827 (2005)
27. Govorov, A.O., *Enhanced Optical Properties of a Photosynthetic System Conjugated with Semiconductor Nanoparticles: The Role of Förster Transfer*. Adv. Mater. **20**, 4330-4335 (2008)
28. Murray, C.B., C.R. Kagan, and M.G. Bawendi, *Synthesis and characterization of monodisperse nanocrystals and close-packed nanocrystal assemblies*. Annu. Rev. Mater. Sci. **30**, 545-610 (2000)
29. Rogach, A.L., et al., *Aqueous synthesis of thiol-capped CdTe nanocrystals: State-of-the-art*. J. Phys. Chem. C **111**, 14628-14637 (2007)
30. Resch-Genger, U., et al., *Quantum dots versus organic dyes as fluorescent labels*. Nat. Meth. **5**, 763-775 (2008)
31. Medintz, I.L., et al., *Quantum dot bioconjugates for imaging, labelling and sensing*. Nat. Mater. **4**, 435-446 (2005)
32. Sukhanova, A., et al., *Highly Stable Fluorescent Nanocrystals as a Novel Class of Labels for Immunohistochemical Analysis of Paraffin-Embedded Tissue Sections*. Lab. Invest. **82**, 1259-1261 (2002)
33. Nabiev, I., et al., *Fluorescent Colloidal Particles as Detection Tools in Biotechnology Systems*, in *Colloidal Nanoparticles in Biotechnology* (Eds.: A. Elaissari). pp. 133-168. John Wiley & Sons, Inc., New Jersey (2007)
34. Zakharova, N.I. and I.Y. Churbanova, *Methods of Isolation of Reaction Center Preparations from Photosynthetic Purple Bacteria*. Biochemistry (Moscow) **65**, 149-159 (1999)
35. Feher, G. and M.Y. Okamura, in *The Photosynthetic Bacteria* (Eds.: R.K. Clayton and W.R. Sistrom). pp. 349-386. Plenum Press, New York (1978)
36. Zankel, K.L., D.W. Reed, and R.K. Clayton, *Fluorescence and photochemical quenching in photosynthetic reaction centers*. Proc. Natl. Acad. Sci. USA **61**, 1243-1249 (1968)
37. Collins, A.M., et al., *Kinetics and energetics of electron transfer in reaction centers of the photosynthetic bacterium Roseiflexus castenholzii*. Biochim. Biophys. Acta. Bioenerg. **1807**, 262-269 (2011)
38. Garcia, D., P. Parot, and A. Verméglio, *Purification and characterization of the photochemical reaction center of the thermophilic purple sulfur bacterium Chromatium tepidum*. Biochim. Biophys. Acta. Bioenerg. **894**, 379-385 (1987)
39. Taremi, S.S., C.A. Violette, and H.A. Frank, *Transient optical spectroscopy of single crystals of the reaction center from Rhodobacter sphaeroides wild-type 2.4.1*. Biochim. Biophys. Acta. Bioenerg. **973**, 86-92 (1989)

5. PROTEIN-BASED PHOTOCHROMIC MATERIAL

Bioelectronics is an established multidisciplinary field that deals with the implementation of biological molecules in electronic and photonic devices. In recent years, however, the progress made in emerging areas such as nanophotonics and nanobiotechnology has opened new frontiers in bioelectronics. The integration of the above-mentioned disciplines has excellent near-term potential to supply the state-of-the-art systems through the development of novel sensors and electronic and optical device components with improved sensitivity, stability and performance efficiency.

In bioelectronics, much of the research effort is concentrated on self-assembled monolayers, thin films and protein-based devices [1]. By far the most researched protein for device applications is bacteriorhodopsin (bR), both because of its photochromic and photoelectric properties, and also its chemical, thermal and photo-stability [2]. The next two chapters explore the possibility of optical manipulation of bR's properties through nano-scale interactions between bR and semiconductor quantum dots (QDs) when assembled to form a nano-bio hybrid material. In this chapter, energy transfer processes and resulting biofunctionality improvements in the bR/QD material [3] are dealt with, while in Chapter 6 the initial studies of the non-linear optical properties of the bR in these hybrid complexes are described.

5.1. Bacteriorhodopsin protein

Bacteriorhodopsin is the only protein found in the purple membranes (PMs) that are grown by *Halobacterium salinarum*, also known as *Halobacterium halobium*. These bacteria live in salt lakes and marshes and use respirative phosphorylation as the main method of energy supply. However, oxygen levels in salt waters are often very low, and when the concentration of the dissolved oxygen falls below what is needed for normal respiration, the bacteria switches to alternative means of energy conversion. One of these means is a system consisting of the bacteriorhodopsin protein coupled to ATP synthase (Figure 5.1); together, these form the simplest photosynthetic system known. The bR protein acts as a photoinduced proton pump that establishes a proton gradient, which is then used by ATPase to convert ADP into ATP, thus satisfying the energetic requirements of the bacteria.

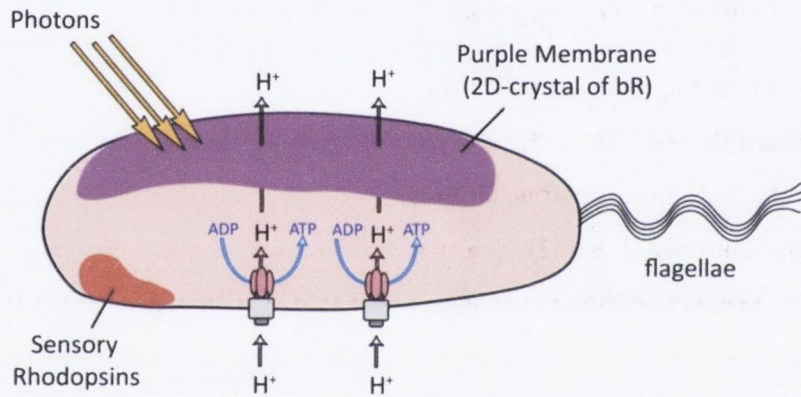


Figure 5.1| Schematic model of a halobacterial cell. A portion of the cell membrane is covered by a 2-D crystal of bacteriorhodopsin protein – the purple membrane. The bacteriorhodopsin protein, which acts as a light-activated proton pump, is coupled to the ATP synthase to form the simplest known photosynthetic system. Other components, such as sensory rhodopsins and flagellae, are used to locate the best environmental conditions for bacterial growth.

5.1.1. Purple membranes

The purple membranes of *Halobacterium salinarum* consist of bR protein spanning across a lipid bilayer membrane [2]. In PMs, the bacteriorhodopsin is in the form of trimers that are arranged in a two-dimensional hexagonal array (Figure 5.2). This crystalline structure protects the functional part of the protein from outside influences, such as high temperatures, pH values and salt concentrations [4]. Purple membrane patches can be extracted from

Halobacteria by utilising the lysis¹ of the bacterium cells in pure water [2, 5, 6]. Purple membranes used in this study were either bought from MIB GmbH or they were isolated² using a standard protocol first introduced by Oesterhelt and Stoeckenius in 1974 [7] and later optimized by Lorber and DeLucas [8]. To summarise, this method involves the lysis of the bacterial cell resulting in the release of different cell fragments, including patches of the purple membranes, which have the highest buoyant density [2]. The PMs are removed from this mixture by centrifugation and re-suspension in water, followed by a purification of the membranes by centrifugation on a sucrose gradient. After final re-suspension in a sodium phosphate buffer and centrifugation to remove any left-over insoluble material, the protein is dialysed against an aqueous solution [8]. The extracted PMs were several hundreds of nanometers in diameter and ~5 nm in thickness (Figure 5.3).

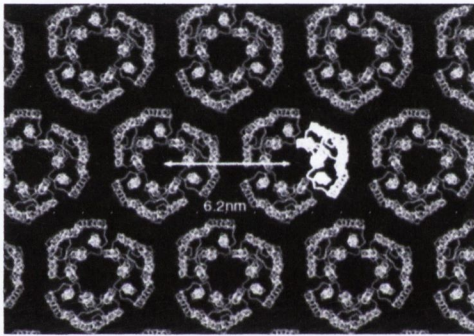


Figure 5.2 | Purple membrane structure. Purple membranes contain 2-D hexagonal array of bR trimers, shown in white, with 6.2 nm unit cell dimension. A single bR unit is highlighted. Adapted from [4].

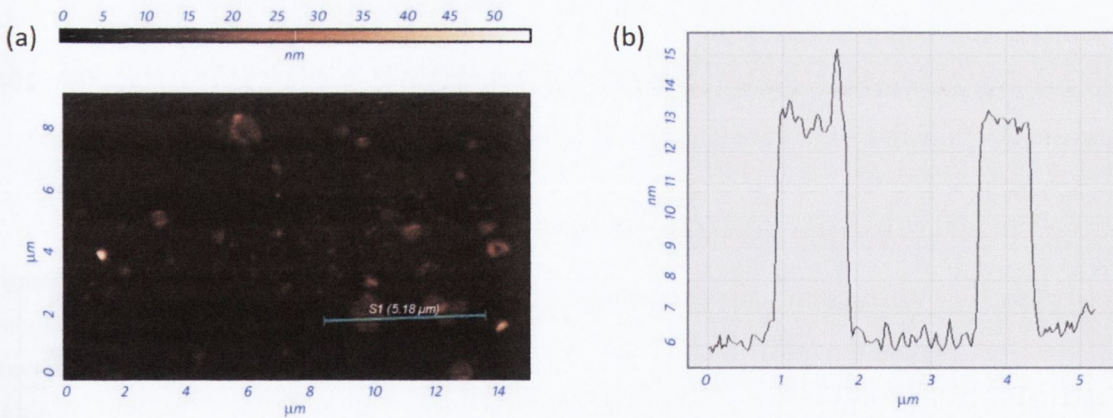


Figure 5.3 | Purple Membrane patches. (a) AFM image of extracted PMs deposited onto glass/ITO substrate using electrophoresis in an aqueous solution. The diameter of PM patches varied from 200 nm to 1 μm . PMs bought from MIB GmbH were found to be of similar sizes (not shown). (b) Line cross-section across two PM patches (indicated by blue line in panel a). The thickness of PMs was $\sim 6 \pm 1$ nm, similar reported literature values [9].

¹ Lysis is the disintegration of the cell membrane, with a subsequent release of cell components.

² Isolation of PM preparations were performed by Vladimir A. Oleinikov (Shemyakin-Ovchinnikov Institute of Bioorganic Chemistry, Russian Academy of Sciences, 117977 Moscow)

5.1.2. Bacteriorhodopsin – structure and function

Bacteriorhodopsin has seven trans-membrane α -helices, arranged in two arcs (Figure 5.4 , [2]). The light-absorbing element of the protein – the chromophore – is a retinal (vitamin A aldehyde) molecule in *all-trans* conformation. It is covalently bound to the Lys-216 amino acid of one of the helices (helix G) by a protonated Schiff base. In a free state, the retinal molecule is easily photooxidised. However, in the protein it is protected from being attacked by reactive chemical species (singlet oxygen and free-radicals) by the secondary and tertiary structure of the protein – the α -helices and other amino acids [1, 2].

Upon absorption of light, the bacteriorhodopsin transports a proton from the intracellular to the extracellular side of the membrane. The transport of the proton occurs through a series of steps, or intermediate states, involving changes in electronic density and molecular conformations of the retinal molecule, some amino acids and a few water molecules. The initial event (the primary photochemical event) after chromophore excitation is a large shift of electron density along the retinal molecule, towards the protonated Schiff base making this side of the retinal molecule more negative [1]. This creates a repulsive interaction between the $C^{14}C^{15}H=NH$ -Lys group of retinal and the nearby aspartic acid residues Asp-85 and Asp-212 (Figure 5.4), which triggers a rotation of the retinal around the $C^{14}C^{15}$ bond – the so-called *all-trans* to *13-cis* photoisomerization. This primary process occurs in less than a picosecond after the initial excitation [10-13] to form the first trappable intermediate state *K* [4, 14]. The rest of the proton transport occurs through a series of dark reactions involving the aspartic acid residues 38, 85 and 96, arginine residue 82 (Arg-82), glutamic residues 194 and 204 (Glu-194 and Glu-204) and the Schiff base (Figure 5.4) [2, 4].

Table 5.1| Properties of the main intermediate states of bacteriorhodopsin.

State	Absorption maximum (nm)	Extinction coefficient ($M^{-1} cm^{-1}$)	Retinal configuration	Protonation of Schiff Base
bR	570	63,000	<i>all-trans</i>	protonated
K	586	52,100	<i>13-cis</i>	protonated
L	544	48,900	<i>13-cis</i>	protonated
M	409	48,800	<i>13-cis</i>	-
N	562	46,100	<i>13-cis</i>	-
O	629	61,900	<i>all-trans</i>	protonated

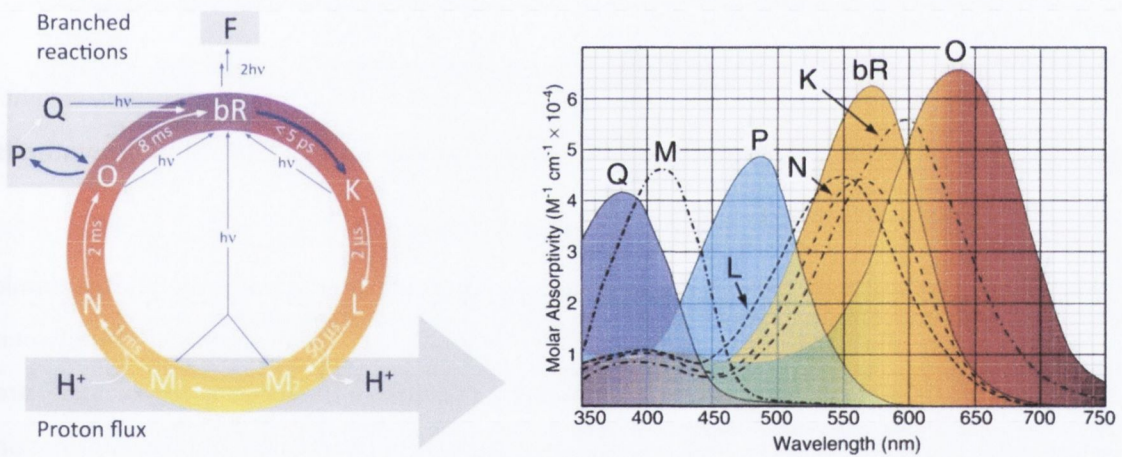
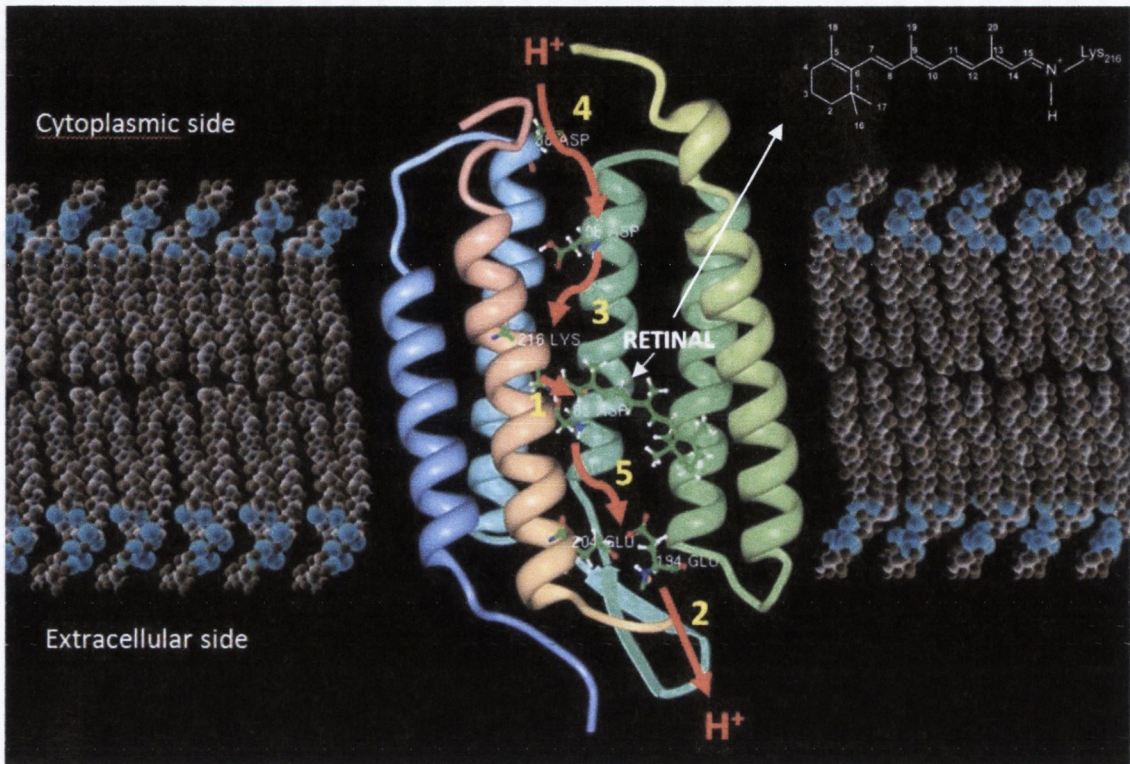


Figure 5.4| Proton transport by bacteriorhodopsin protein. Top panel shows the bacteriorhodopsin protein integrated into a bilipid membrane. bR has seven trans-membrane α -helices (one helix was omitted for clarity). The chromophore element of the protein is a retinal molecule (structure shown in top right corner). It is attached to one of the helices through the Lys-216 amino acid. The red arrows and the corresponding numbers (in yellow) indicate the sequence of protonation events that occur during the transport of a proton from the cytoplasmic to extracellular side of the membrane. Each step of the proton transport cycle corresponds to a different intermediate state of bR. **Bottom panel** shows the bR photocycle. The blue arrows indicate optical transitions; the white arrows are thermal transitions. The lifetimes of the intermediate states are indicated beside the arrows. A proton is released upon L to M₂ transition and uptaken in the M₁ to N transition. The two branched reactions are also shown. The bR to F transition requires two-photon absorption and is irreversible. The absorption spectra of bR intermediates are shown on the right (from Birge et al [1]).

The retinal molecule is highly sensitive both to its molecular conformation and to its electrostatic interaction with the nearby charged amino acids [11]. As a result, the intermediate states have different absorption spectra covering the whole visible wavelength range (bottom panel of Figure 5.4, Table 5.1).

5.1.3. Applications of bacteriorhodopsin

Bacteriorhodopsin has been considered for a broad range of applications due to its unique properties and also its excellent thermal, chemical and photo- stabilities. As an example, its cyclicity at ambient temperature exceeds 10^6 , and it is operational at temperatures up to 140 °C and at 0 – 12 pH range [4]. All of the technological applications of this protein are based on either of its photoelectric, photochromic or charge transfer properties (Figure 5.5).

The photoelectric properties of bR arise from the electron density shift that takes place immediately after absorption of a photon by bR in its ground state [4]. The shift in electron density is large enough to create a measurable photovoltaic response. Several reports exist on utilization of this property of bR in the development of ultrafast light detectors [15], artificial retinas [16-18] and motion detectors [18].

The charge transfer properties rely on the biological function of bacteriorhodopsin as a light-activated proton pump. This property of the protein can be used in artificial photosynthesis [19-23] or saltwater desalination [24].

By far the majority of the research has been focused on the exploitation of the photochromic properties of bR. These applications are based on the possibility of optically switching between different bR states that have distinct absorption maxima. Of particular importance are information storage and processing applications, such as 3-D and holographic information storage [1, 25-28], associative memories [1, 4, 29], spatial light modulators [4, 11, 30, 31], pattern recognition [4, 32, 33] and optical filtering [33, 34] to name but a few (Figure 5.5). Most of these applications require some intermediate states to be “frozen” (stabilised thermally) or stabilised through genetic modification of the protein. For example, substitution of the aspartic acid residue 96 by asparagines (D96N mutant) or drying of the PM film both inhibit the proton transport function of the protein and as a result considerably lengthen the lifetime of the M-state [35].

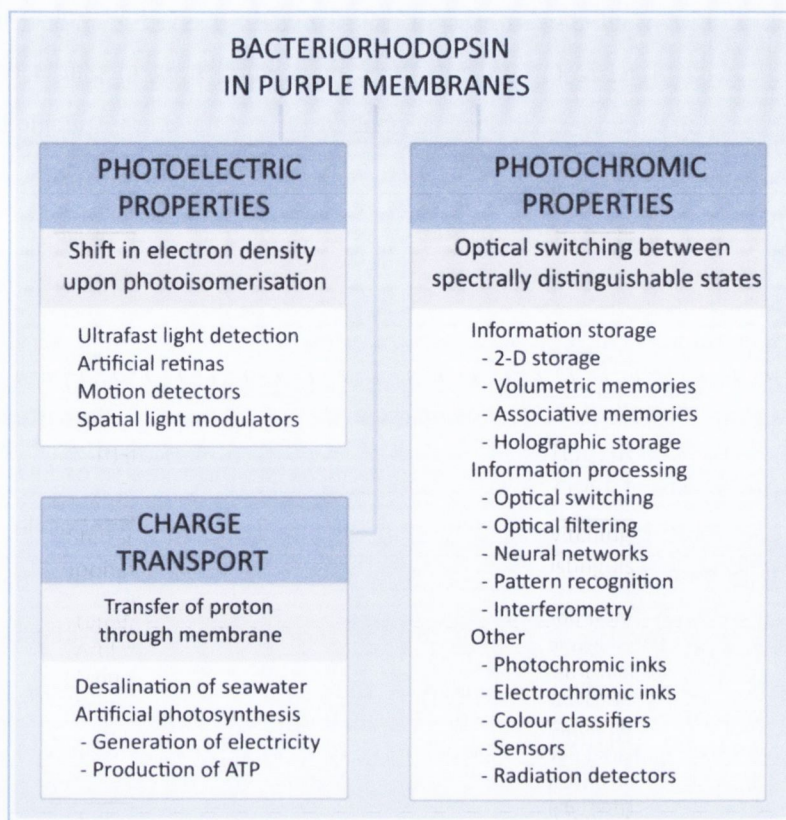


Figure 5.5| Bacteriorhodopsin properties and applications. Technological applications of bacteriorhodopsin are based on at least one of its properties.

5.1.4. Bacteriorhodopsin and semiconductor nanocrystals

Due to the harsh environmental conditions in which *Halobacteria salinarum* live the function of the bR has been optimised by evolution. For technological applications this promises reliable device performance with high fatigue resistance. Furthermore, site-selective mutagenesis allows modification of the original (“wild-type”) bacteriorhodopsin. Using this type of genetic engineering, the protein can be made sensitive to specific chemicals or biological structures, interactions with which induce changes in the proton-transport and the photocycle of bR. As a result, bR is considered to be the most promising biological candidate for optoelectronic device applications thereby comprising a unique molecular platform onto which various functional elements can be built.

Several obstacles exist to the wide-spread commercial application of this protein. First of all, photosensitive proteins are not able to interact with UV photons and often they do not absorb them at all. If photons of such high energy are absorbed, they might destroy the light-harvesting chromophores [36] or induce apoptotic-like cell death [37]. As a result, the input-to-

output conversion of energy in protein-based systems is often very low. For example, owing to the presence of a light-harvesting system, the energy harvesting in plants has a maximum efficiency of 5% [38, 39]. Bacteriorhodopsin, which does not have any specific light-harvesting system, is able to utilize only 0.1-0.5% of the solar light [38]. Furthermore, current devices based on bR have dimensions on the order of several millimetres and utilize relatively large light sources. Finally, the cost of bR-based devices remains high, making it the main factor hindering commercial application.

Nanotechnology may open the way to enhance the performance of bR biological function. Very recent technological developments to control the shape and size of QDs show that it is now possible to concentrate and transfer optical energy on the nanoscale, far below the diffraction limit of light [40, 41]. This presents a novel way to exploit these nanosized optical materials. The energy transfer from QDs to bacteriorhodopsin is possible because the bR-linked chromophore - the retinal molecule - is located near to the centre of the PM, at a distance of ~ 2.5 nm from both PM surfaces (Figure 5.6(a)) [42]. This distance is far less than the average Förster radius of ~ 5 nm found in energy transfer processes involving semiconductor QDs [43].

The integration of QDs with biological systems to form functional assemblies offers great promise for the design of highly efficient energy transfer-based nanomaterial, combining the unique properties and functionality of the bacteriorhodopsin with the broad absorption bands and size-tunable emission of QDs. Provided that energy transfer between QDs and bR can be achieved, emission of QDs immobilized on the PM surface could be modulated depending on the stage of the bR cycle. Moreover, if the nanocrystals can be specifically attached to the protein, a whole array of such nanoscale optical switches could be created. Such hybrid structures may find applications in nanosensing, nanoactuators, lighting, optical data storage, optical switching, transmission and computational devices. Furthermore, the proposed strategy can significantly reduce the material costs involved in the development of bR-based devices.

In this chapter, the investigations carried out on the preparation, energy transfer properties and biofunctionality of the hybrid material consisting of semiconductor quantum dots and bacteriorhodopsin protein within purple membranes are detailed (Figure 5.6).

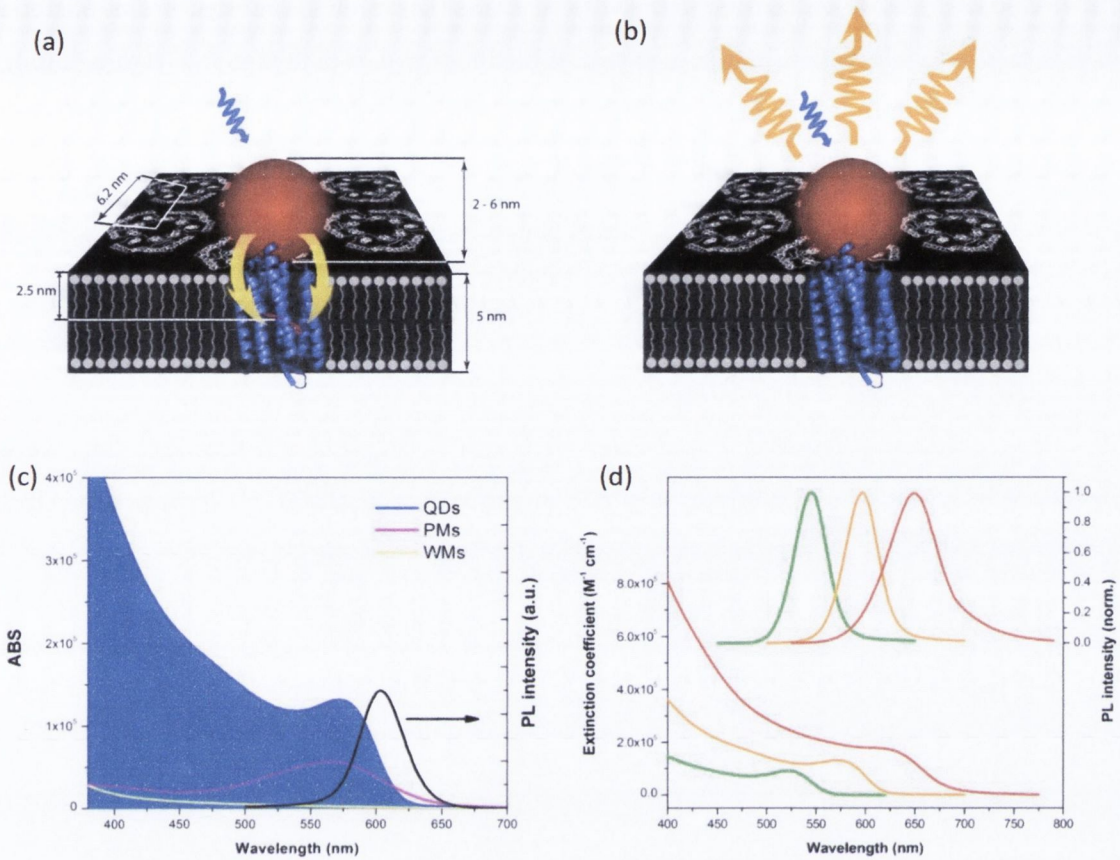


Figure 5.6 | Structure of Purple membrane/Quantum Dot hybrid material and optical properties of constituents.

All objects drawn in panels **a** and **b** are given to scale. **(a)** Photons are absorbed by a QD immobilized on the surface of the PM containing bR protein. Each bR molecule contains one chromophore, which absorbs in visible region of optical spectrum (retinal, shown in purple). Retinal is located in the centre of the PM, ~ 2.5 nm from each membrane side. An exciton from the QD (donor, shown in red) is transferred via FRET to the retinal molecule of bR (acceptor) thus initiating retinal photoisomerisation, charge separation near the retinal's Schiff base, bR photocycle and proton pumping through the PM. The energy transfer process quenches QDs' emission, and so there is no emission from this PM/QD material. Panel **(b)** shows the QD complex with the "white membrane" – the bR-containing PMs as those shown in **(a)** but with the retinal molecule extracted. Here, QD immobilized on the surface of the PM does not transfer an exciton to the acceptor because the acceptor (retinal) is absent. In the absence of energy transfer, the QD remain fluorescent due to the electron-hole recombination within the QD. **(c)** UV-vis spectra of PM (purple line), white membranes (grey line), UV-vis spectrum for one of the types of QD used in the study (filled with blue) and the PL emission spectrum of this QD sample (black line). **(d)** UV-vis absorption and PL emission spectra of CdTe QD550 (green curves), QD600 (orange) and QD650 (red) used in the study.

5.2. Preparation of PM/QD material

The preparation of PM/QD material involved assembly of PMs, purified from bacteria *Halobacterium salinarum* as described above, with either CdTe or CdSe/ZnS QD (Figure 5.6(a)). QDs samples of different diameters were chosen for the assembly to provide varying spectral overlaps between the emission bands of the QDs (donors of energy) and the absorption of the retinal molecule (acceptor) of bacteriorhodopsin (Table 5.2, Figure 5.6(b)). QDs were attached to the PMs using both electrostatic self-assembly and covalent conjugation techniques.

5.2.1. QD/PM complex formation

To prepare covalent conjugates of QDs and PMs, PEG-COOH-stabilised CdSe/ZnS QDs were chemically attached to PMs using carbodiimide chemistry¹, in which COOH- groups of the QDs' ligand molecules react with the NH₂- groups of bR, forming a peptide bond:

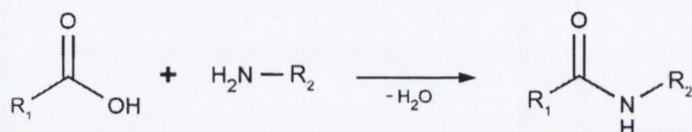


Table 5.2| Physico-chemical properties of Quantum Dot samples used for electrostatic assembly.

Sample*	Emission maximum (nm)	Quantum yield (%)	Core Diameter** (nm)	Hydrodynamic diameter*** (nm)	Zeta potential (mV)
Cys CdSe	533	40	2.5	5 ± 1	-29.2
PEG-COOH CdSe	528	38	2.5	9 ± 2	-30.7
PEG-OH CdSe	529	38	2.5	10 ± 3	-14.4
QD550-CdTe	545	34	2.5	3 ± 1	-23.8
QD590-CdTe	589	24	3.1	4 ± 1	-24.8
QD600-CdTe	597	36	3.2	4 ± 1	-25.4
QD645-CdTe	645	28	3.8	5 ± 1	-41.3
QD650-CdTe	650	29	3.8	5 ± 2	-32.6

*CdSe QDs were CdSe/ZnS QDs. CdTe QDs were stabilised by thioglycolic acid (TGA). **The diameters of CdTe and CdSe QDs were calculated according to Rogach *et al.* [44] and Yu *et al.* [45] respectively. ***The hydrodynamic diameters and zeta potentials were determined by dynamic light scattering measurements (described in Chapter 2).

¹ Performed by Dr. A. Sukhanova (Université de Reims Champagne-Ardenne, France).

All conjugates were purified using gel filtration on Superdex 200 resin (GE Healthcare) columns. The collected fractions were inspected by UV-vis spectroscopy and the bR to QD molar ratio for each fraction was determined by deconvoluting the absorption spectrum of the complex into contribution from QD and bRs' retinal. Only fractions containing bR-QD complexes were used for further experiments.

For electrostatic assembly, PMs and QDs stock solutions were sonicated for 1 minute. Different amounts of PMs were then added to the QD stock to discretely vary the bR to QD molar ratio of the assembled complexes. The mixed PMs and QDs were allowed to self-assemble for 30 minutes under gentle agitation, at ambient conditions.

5.2.2. Self-assembly of QDs on PMs

A purple membrane consists of ~9% bacteriorhodopsin protein embedded in a bi-lipid membrane [46]; therefore, there are approximately 19 lipid molecules for each bR protein. In a membrane, the lipid molecules are oriented such that their negatively-charged PO_3^- groups are on the surface of the membrane (Figure 5.7). The bacteriorhodopsin itself has 14 positively-charged amino acid residues (lysine and arginine), 9 of which are on the cytoplasmic surface of the bR protein and 3 acid residues are exposed on the extracellular side [46]. This means that, although the overall charge of the PMs is negative, there are sufficient positive charges on the PMs (localised at bR trimers) for negatively-charged QDs to interact with (Figure 5.7). It can be envisaged that such interaction, in the form of electrostatic attraction, can display certain specificity of QDs adsorption towards the bR trimers.

High-resolution atomic force microscopy (AFM) images of purple membranes, deposited onto freshly-cleaved mica, clearly show the bR protein trimers arranged in a hexagonal lattice with a unit-cell dimension of 6.2 nm (Figure 5.8(a)), which is in good agreement with previously reported value [47]. Deposition of a small amount of QDs solution on top of the PMs (1:2 QD:bR molar ratio) for 30 minutes, followed by washing-out of the non-bound QDs results in a 2-D organisation of QDs on the PMs' surface (Figure 5.8(b)). Most notably, the period of QDs' organisation of ~6.09 nm corresponds well with the unit cell dimension of the 2-D hexagonal crystalline lattice of bR protein (6.2 nm), suggesting that specific association exists between the negatively-charged QDs and the positively-charged groups of bR trimers on the surface of the PM at low QD/bR ratios. An increase of the QD/bR ratio in the QD-PM hybrids leads to the disappearance of the regular ordering of QD on the surface of the PMs and formation of irregular multilayers (panels C and D of Figure 5.8), similar to Stranski-Krastanov growth.

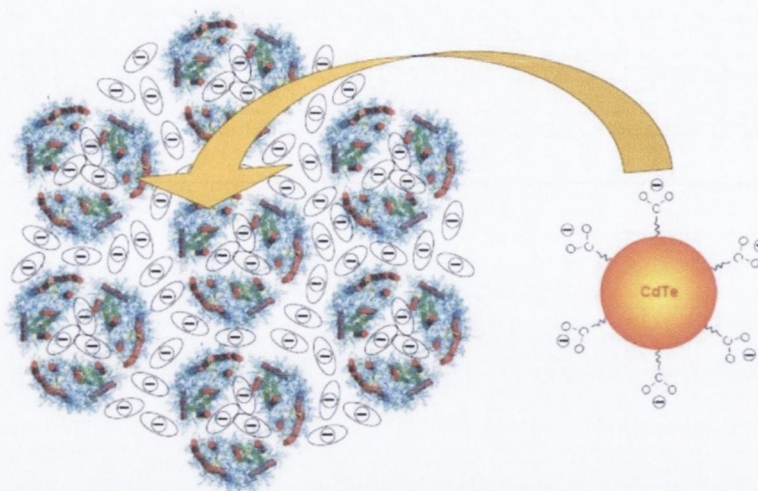


Figure 5.7| Electrostatic attraction between quantum dots and bacteriorhodopsin. The lipid molecules of the PMs have negatively-charged end-groups, giving an overall negative surface charge to PMs. The bacteriorhodopsin protein (shown in colour) has positively-charged amino acid residues on PM surface. The negatively-charged QDs are electrostatically attracted to these positive patches.

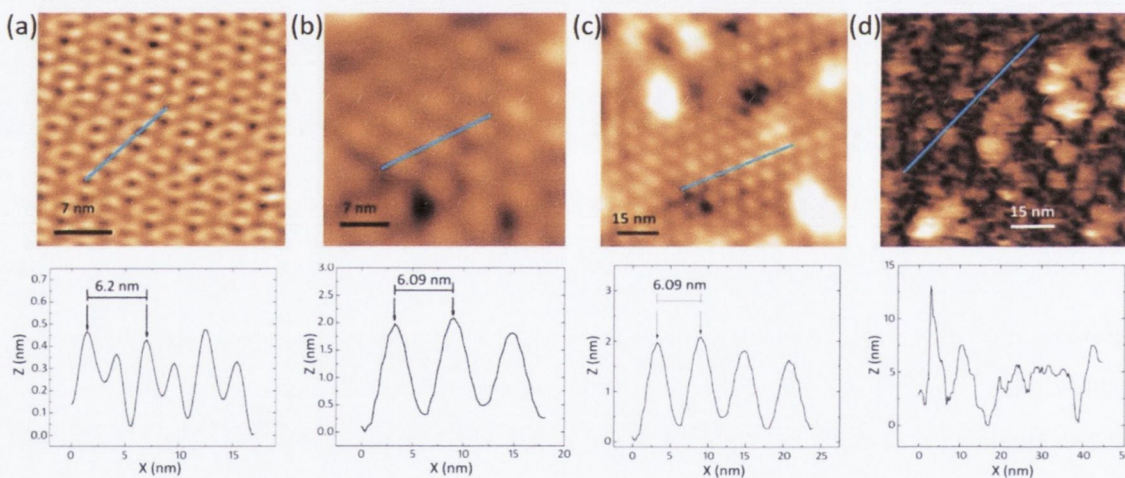


Figure 5.8| Atomic force microscopy images¹ of bacteriorhodopsin within its natural purple membrane (a) and the assemblies of purple membrane with quantum dots (b, c, d). Graphs below the AFM images of the Panels a-d show AFM profiles (cross-sections) along the blue lines in the corresponding AFM-images. These profiles show that the period of bR trimers organisation within the PM (6.2 nm, Panel a) corresponds well to the period of QD organisation on the PMs upon assembling in aqueous solution (6.09 nm, Panels b and c). Panels c and d compare assembly of QDs at the low (one-to-two, Panel c) and the high (three-to-one, Panel d) QD to bacteriorhodopsin molar ratios. An increase of the QD/bR ratio in a QD-PM hybrid material leads to disappearance of the regular ordering of QDs on the surface of the purple membranes.

¹ AFM scans in a liquid chamber were performed by Nicolas Bouchonville, Michael Molinari. Full details can be found in the supplementary information of [3].

The assembly of QDs on PMs in aqueous solution was also monitored by zeta potential measurements (Table 5.3). Upon initial addition of PMs, which have an overall negative charge, to negatively-charged QDs the zeta potential increased in amplitude (from -24 mV to -67 mV). A further increase of bR to QD molar ratio resulted in a decrease of the overall negative surface charge from -67 mV to -47 mV, corresponding to self-assembly of QDs on top of the PMs via electrostatic interactions between QDs and the positive groups of bR protein.

Table 5.3| Zeta potential data for QD550-CdTe assembled with PMs at different bR to QD molar ratios. The initial decrease of the zeta potential upon addition of PMs to QDs was followed by a steady increase, corresponding to the electrostatic interaction between negatively-charged QDs and positively-charged groups of bR protein.

bR to NC ratio	Zeta Potential (mV)
0	-24 ± 6
0.02	-67 ± 8
0.05	-62 ± 13
0.09	-59 ± 16
0.14	-49 ± 8
0.19	-47 ± 12

5.3. Investigations of energy transfer

One of the prerequisites of the enhancement of the photochromic, photoelectric and proton pumping properties of bacteriorhodopsin in bR/QD hybrid material is the occurrence of energy transfer. This section describes the investigations of the energy transfer process in this material, including verification of the energy transfer occurrence and analysis of the parameters that affect the energy transfer process.

5.3.1. Verification of energy transfer occurrence

The preliminary spectroscopic measurements of the PM/QD hybrid material were aimed at the verification of the occurrence of FRET from QDs (donors) to the retinal molecule (acceptor) of the bR protein. Measurements involved electrostatically-assembled complexes of PMs with CdTe QDs emitting at 590 nm (QD590-CdTe) and 650 nm (QD650-CdTe). Results of the steady-state PL measurements showed that PM-QD assembly at increasing bR to QD molar ratios lead to increasingly efficient quenching of the excitonic emission of QDs (Figure 5.9(a)). The smaller QD590 were quenched more efficiently at same bR to QD molar ratios, when compared to the quenching of QD650. Such difference in quenching behaviour is expected when one considers the smaller donor-acceptor distance between the QDs and the retinal of the bR protein due to smaller diameter of QD590, as well as the slightly better spectral overlap between the PL band of QD590 and the absorption spectrum of bR's ground state (Figure 5.11(a)).

Time-resolved PL decay data provided further evidence of FRET within the bR/QD hybrid material (panels (c) and (d) of Figure 5.9). For example, the average lifetime for a complex consisting of ~0.5 bR per CdTe QD650 decreased from 10 ns to 8 ns; this constitutes a decrease of about ~20% (Table 5.4). A decrease in the average radiative lifetime of QD' PL is expected if FRET exists since the energy transfer from QD to the retinal provides an additional kinetic pathway for the decay of QDs' excitation [48]. The integrated PL intensity for this bR/QD complex decreased by ~19%, so there is very good agreement between the two measurements suggesting that FRET is the main mechanism of the QDs' PL quenching.

Confirmation of FRET as the principle quenching mechanism was also obtained from the comparative quenching of QD with the PMs and white membranes (WMs). White membranes are purple membranes from which the retinal molecule has been removed. Since the retinal molecule acts as acceptor of energy, WMs present an excellent control material for studying FRET between QD and bR. The structure and morphology of the protein and lipid components in WM are the same as those for PM, providing equal possibilities for any non-radiative quenching of QDs upon their binding to either PM or WM, whereas the absence of retinal

(acceptor) completely excludes the FRET-channel of QD quenching in their complex with WM (Figure 5.6(a) and (b)).

The WMs were produced using a standard protocol, in which a solution of PMs in 0.3 M hydroxylamine is illuminated with white light until the Schiff base, through which the retinal molecule is connected to the bR protein, is entirely reduced (equivalent to complete photobleaching of PMs) [49]. Parallel titration of CdTe QD590 with PMs and with WMs were performed and showed that quenching of QDs' fluorescence by WMs is 4-5 times less than with the PMs. This experiment provided us with a quantitative level of the possible contribution of non-radiative QD quenching in the PM or WM hybrids and proved that the main mechanism of QD quenching with PM is indeed FRET.

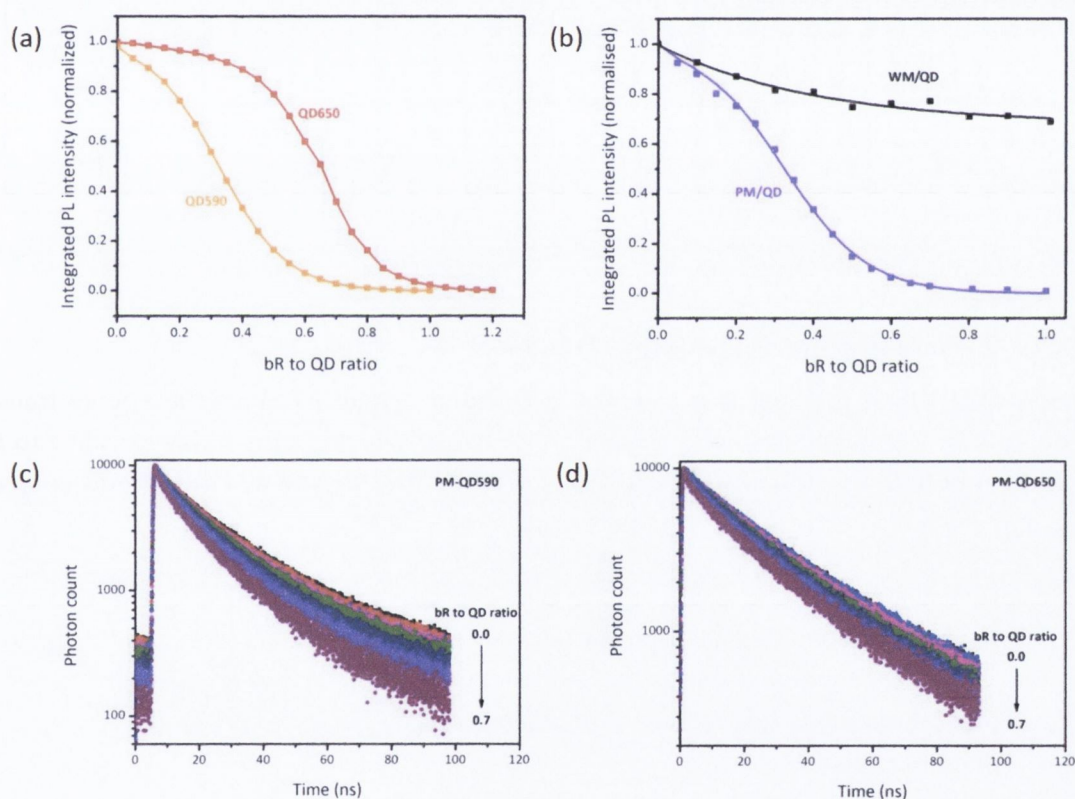


Figure 5.9| Integrated and time-resolved photoluminescence as a function of protein to quantum dots molar ratios. (a) Quenching of CdTe QD590 and QD650 emission by bacteriorhodopsin. **(b)** Comparison of PL quenching of QD590-CdTe by purple membranes (purple, PM/QD) and white membranes (black, WM/QD). **(c) and (d)** Time-resolved fluorescence measurements show the decay of **(c)** QD590-CdTe and **(d)** QD650-CdTe fluorescence in complexes containing increasing amounts of PMs. An increased rate of PL decay for complexes with increasing bR (acceptor) to QD (donor) molar ratios corresponds to a decrease in lifetime, indicative of FRET in these complexes.

Table 5.4 | Quenching of QD650-CdTe luminescence by bacteriorhodopsin and corresponding changes in radiative lifetime. τ is the average lifetime of a bR/QD complex, E is FRET efficiency calculated from the reduction of QDs' radiative lifetime and $(1 - E)$ is the expected PL intensity for a complex for an ideal case, in which FRET is the only mechanism of quenching. $I_{complex}/I_{QD}$ is the normalised PL intensity of the complex measured by steady-state photoluminescence measurements.

bR to QD molar ratio	τ (ns) ± 0.15	E (%) $\pm 2\%$	$1 - E (= \tau_{complex}/\tau_{QD})$ ± 0.02	$I_{complex}/I_{QD}$ ± 0.01
0.00	9.94	0	1.00	1.00
0.14	9.58	4	0.96	0.98
0.36	9.19	8	0.92	0.91
0.48	7.98	20	0.80	0.82
0.66	5.58	44	0.56	0.48
0.78	3.57	64	0.36	0.19

5.3.2. Parameters affecting energy transfer

The PM/QD hybrid material is a complex FRET-based system in which the energy transfer process from QDs to the retinal molecule of the bacteriorhodopsin is highly sensitive to the properties of both constituents (Figure 5.10). Consequently, the energy transfer efficiency was found to depend on a number of parameters, such as:

- QDs' diameter
- QDs' composition (type, material, ligand layer)
- QDs' surface charge (electrostatic self-assembly)
- pH of the solution (electrostatic self-assembly)
- Method of assembly
- Mutation of bR protein

The effect of each of these parameters was evaluated by measuring the quenching of QDs' emission in the presence of increasing amounts of PMs by steady-state PL measurements.

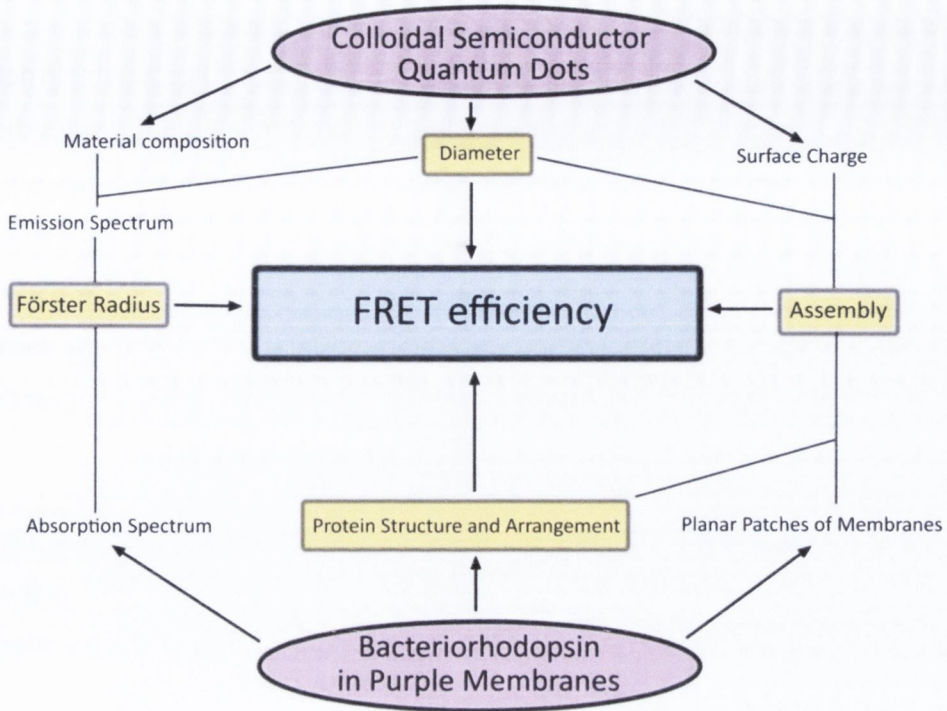


Figure 5.10| Parameters affecting Förster Resonance Energy Transfer in Purple Membrane/Quantum Dot complexes. The physico-chemical properties of both the QDs and the PMs influence the energy transfer efficiency from QDs to the retinal molecule of bR protein in PM/QD complexes.

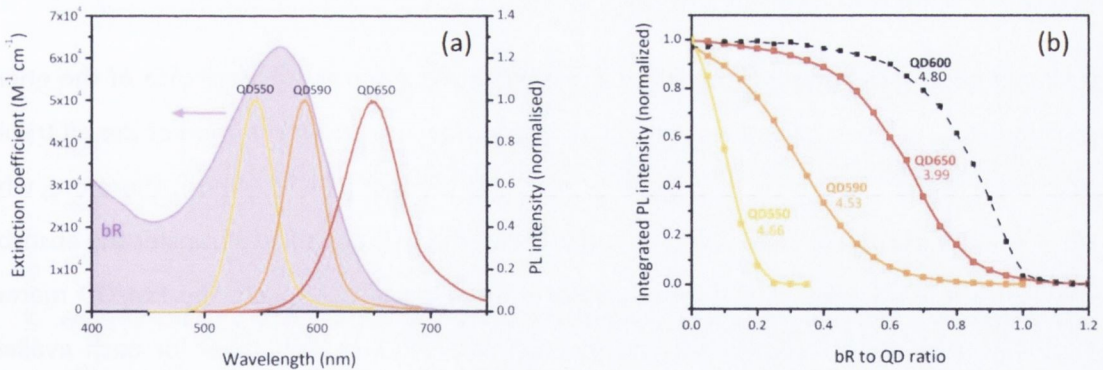


Figure 5.11| QDs' size-dependence of the energy transfer efficiency in QD/PM complexes. (a) Position of PL bands of CdTe QDs' relative to bR's absorption band (shaded purple) for increasing QDs sizes. The diameters of QDs samples were 2.8 nm, 3.1 nm and 3.8 nm for QD550, QD590 and QD650 respectively. (b) Fluorescence quenching curves for QDs of increasing diameters. The Förster radii for each QD sample are given below QDs' label. The quenching of QD600 of 3.2 nm core diameter (dashed black line) did not follow the expected size-dependence trend.

Quantum Dots' diameter

The average diameter of a QD sample is perhaps the most influential parameter in determining FRET efficiency. First of all, for any given material, the size of the QDs determines the position of the emission band and thus the amplitude of the spectral overlap with the absorption band of the bacteriorhodopsin. For example, as the core diameter of QDs is increased from ~2.5 nm to 3.1 nm to 3.8 nm, the QDs' emission shifts from 550 nm to 590 nm to 650 nm. Since bacteriorhodopsin ground state has an absorption maxima at 567 nm, the best spectral overlap is achieved for QD550 and QD590 (panel A of Figure 5.11), ensuring largest the Förster radii and most efficient transfer of energy for these QD samples (panel B).

The physical size of QDs also determines the QD-to-retinal separation distance. The smallest achievable separation distance can be approximated to be a sum of QDs' radius and the position of the retinal molecule from the surface of the PM (~2.5 nm):

$$D_{min} = 1/2 * D_{QD} + 2.5 \text{ nm} \quad (5.1)$$

According to this analysis, complexes containing the smallest QDs should display the strongest FRET. As shown in panel B of Figure 5.11, the fluorescence of QD550 ($D_{min} = 3.90 \text{ nm}$) is quenched significantly better by bacteriorhodopsin when compared to the quenching of QD590 ($D_{min} = 4.05 \text{ nm}$), despite the fact that QD550 and QD590 have similar Förster radii (4.66 nm and 4.53 nm respectively).

It should be noted, however, that the discussion above assumes an ideal case of the energy transfer between one QD and one retinal molecule. However, the dimension of the bR trimers (6.2 nm) is of the same order of magnitude as the diameter of QDs (2 - 4 nm). Therefore, when small amount of QDs are assembled on top of a PM, the QDs are able to transfer the absorbed energy to at least three retinal molecules of the nearby bRs. As such, the PM/QD material embodies a multiple-acceptor system, in which case FRET contributions for each available acceptor are additive. As a result, large FRET efficiencies are possible for small QD to bR ratios (large bR to QD molar ratios). For higher quantities of QDs (small bR to QD molar ratios), the system becomes multiple-donor multiple-acceptor one, resulting in competing and therefore reduced energy transfer between neighbouring QDs and several adjacent retinal molecules. This reasoning explains the unique shape of the PL quenching curves observed for the PM/QD complexes (Figure 5.12).

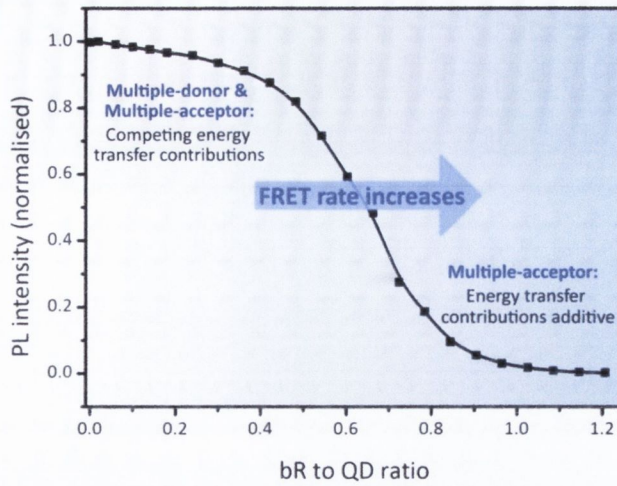


Figure 5.12| Energy transfer in purple membrane/quantum dot complexes. Due to the planar geometry of the purple membranes and the small size of bR's trimers, the energy transfer process is different for low and high bR to QD molar ratios. FRET efficiency is highest for large bR to QD ratios, where energy transfer contributions for each available acceptor are additive.

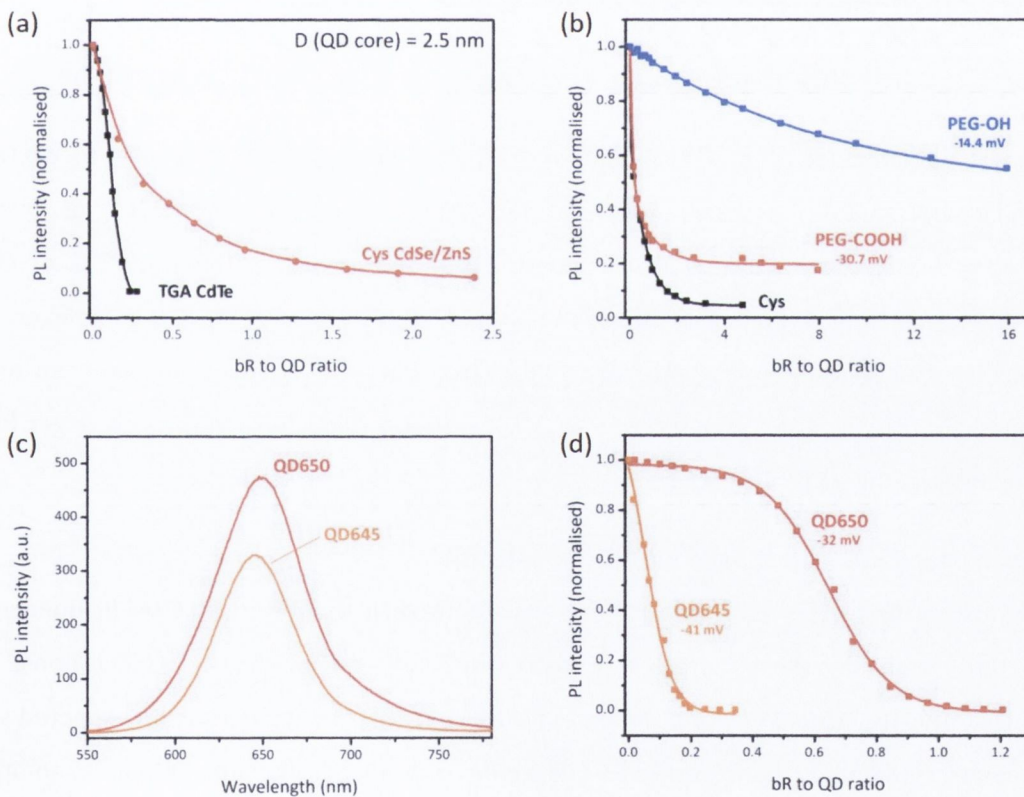


Figure 5.13| Parameters influencing the efficiency of energy transfer. (a) The inorganic shell of CdSe/ZnS QDs, results in increased QD-to-retinal separations when compared to core-only CdTe QDs of same core diameter. As a result, quenching of CdTe QDs is more efficient. (b) Comparison of quenching of CdSe/ZnS QDs of 2.5 nm core diameter capped by different ligands. The thickness of Cys capping is much smaller than PEG-derived polymeric shells. (c) Emission spectra and (d) quenching curves for CdTe QD650 and QD645, which have considerably different surface charges but similar sizes. The numbers (in mV) in panels (b) and (d) are the zeta potentials of QD samples.

Quantum Dots' composition

The effect of QDs' composition on FRET efficiency was evaluated by comparative PL quenching measurements for TGA-stabilised CdTe QDs and several CdSe/ZnS QDs, stabilised by cysteine molecules (Cys) or by PEG-derived polymeric layers (PEG-COOH and PEG-OH). Parameters that were considered were the material of QDs' core, QDs' type and the stabilising ligand molecules.

The position of fluorescence band of QDs of a particular diameter depends primarily on the composition of its core. For example, CdSe QDs of core diameter of ~2.5 nm have emissions peak shifted by ~20 nm to the blue relative to the emission of 2.5 nm CdTe QDs (Table 5.2), resulting in slightly smaller spectral overlap for 2.5 nm CdSe QDs. Furthermore, the CdTe QDs are core-only, while CdSe/ZnS QDs are of core-shell type. Due to the thickness of the inorganic ZnS shell, the overall diameter of CdSe/ZnS QDs is larger than that of CdTe QDs even for smallest stabilising molecules (cysteine). As a consequence of both of these facts, the efficiency of energy transfer in complexes containing CdSe/ZnS QDs was found to always be reduced compared to CdTe QDs/PM complexes of similar bR to QD molar ratios (Figure 5.13(a)).

The final characteristic of a QD sample to be considered was the composition of QDs' stabilising layer and, in particular, the size of the molecules that constitute this layer. Due to the strong dependence of FRET on the donor-acceptor separation, the thickness of QDs' stabilising ligand layer has a strong influence on the energy transfer in PM/QD complexes. For instance, the fluorescence of Cys-stabilised CdSe/ZnS QDs was found to be quenched more efficiently by PMs than the fluorescence of CdSe/ZnS QDs solubilised with much larger PEG-derived polymer layers (Figure 5.13(b)).

Quantum Dots' surface charge and pH of solution

While most of the factors considered above explain the observed trends in QDs' PL quenching by bacteriorhodopsin, there were a few cases which did not conform to expectations. The quenching of CdTe QD600 sample, shown in Figure 5.11 (b), did not follow the expected size-dependency trend when compared to PL quenching of QD550, QD590 and QD650. In addition, the energy transfer efficiency in complexes containing CdSe/ZnS QDs capped with PEG-OH was significantly smaller than same QDs capped with PEG-COOH, despite the fact that the thicknesses of these two polymeric layers are approximately equal. These data indicate that other factors, and in particular the assembly process itself, may play a role in determining the efficiency of FRET in PM/QD complexes.

The self-assembly of QDs with PMs in aqueous solution is likely to be susceptible to the surface charge of the QDs, since it is an electrostatic interaction between the QDs and the bR that is responsible for the assembly. To test this, a control experiment was performed with two close-emitting CdTe QD samples – QD645 and QD650 (Figure 5.13(c)). These two QD samples were similar in all respects except for their surface charge, or equivalently, zeta potentials (Table 5.2). When assembled with PMs, fluorescence of QD645, which have a higher zeta potential of -41 ± 9 mV, was found to be quenched far quicker than that of the lesser charged QD650 nm (zeta potential of -32 ± 6 mV), as expected for electrostatic assembly (higher surface charge allows for stronger attraction between the oppositely charged species, resulting in larger amounts of donor-acceptor pairs interacting and shorter separation distances between them).

Electrostatic assembly of QDs and PMs in aqueous solution can also be controlled by adjusting the pH of the solution. There are several reasons for this. First of all, the de-protonation of QDs' and bR's end groups is sensitive to pH values. Consequently, the surface charge of QDs and the overall charge of the PMs change according to pH changes, affecting the electrostatic interaction between them. Furthermore, the de-protonation of COOH-groups of TGA molecules on the surface of CdTe QDs determines the stability of these QDs. In fact, TGA-stabilised QDs are most stable at pH of ~ 11 , at which QDs' emission is most efficient (inset of Figure 5.14). Such a small increase of QDs' emission can result in a measurable increase of FRET efficiency due to the Förster radius dependency on the QY of QDs, combined with the high sensitivity of FRET efficiency at separation distances close to this radius, which is the case in PM/QD system. The spectral properties of bR also depend on the pH of the solution; in particular, bR's absorption band blue-shifts and decreases as the pH of the solution is raised (Figure 5.14). When assembled with QD550, the shift of the absorption band to the blue enhances the spectral overlap between the PL band of QDs and absorption band of PMs. On the other hand, the overall decrease of the absorption acts to decrease the spectral overlap.

The combined effect of the pH variations was monitored on a 1.1 bRs per QD550 complex, in which the QDs fluorescence was quenched to 50% by PMs at pH7. When such PM/QD550 complexes were assembled at increasing pH values their emission decreased, reaching a maximum reduction of $\sim 60\%$. This is likely to be due to QDs' solubility and stability effects described above – as the pH was increased, QDs become slightly more charged and soluble, and the electrostatic assembly and energy transfer between QDs and membranes is facilitated.

When the pH of the assembling solution was increased further, the fluorescence intensity started to increase. This is due to the fact that bR's absorption is significantly reduced at pH

values above 10, resulting in a lesser spectral overlap between QDs' emission and bR's absorption bands. The bR ability to act as acceptor is thereby lessened and QDs' fluorescence intensity increases.

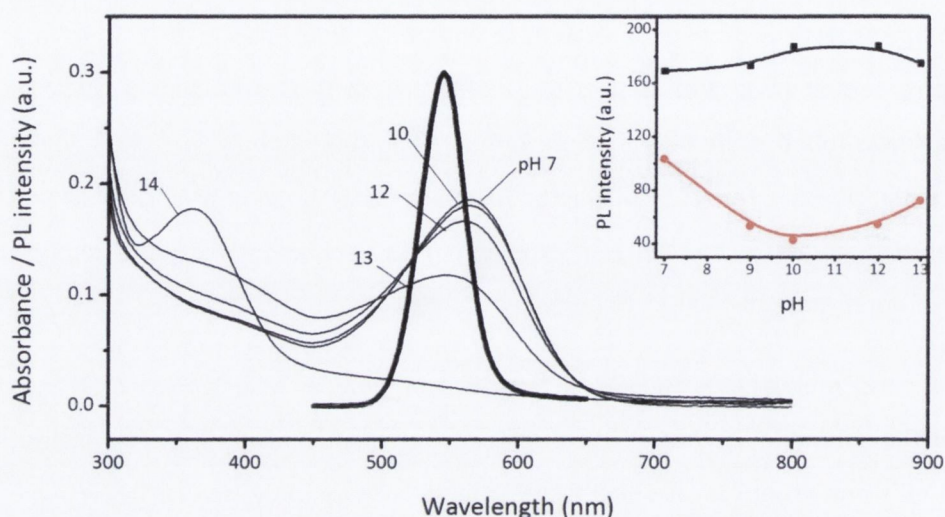


Figure 5.14| Assembly of Quantum Dot/Purple Membrane complexes at different pHs. Main graph: changes in absorption spectrum of bacteriorhodopsin at different pH values, compared to the fluorescence band of QD550. Inset: comparison of PL intensity of 50% quenched PM/QD complexes (red data points) to PL intensity of a pure QD solution (black data points) for 7 to 13 pH range.

Covalent conjugation

Electrostatic assembly, while an effective method of PM/QD material fabrication, does not produce the optimum binding between QDs and bRs because the electrostatic repulsion between the negatively-charged lipid membrane and the negatively-charged QDs is always present. Theoretically, direct chemical attachment of QDs to the exposed amino-acid residues of bR provides a way for the specific attachment of QDs at minimum possible distances from the retinal molecule of the protein.

The experimental estimate of the improvement of QD/PM binding consisted of comparative photoluminescence measurements for electrostatically assembled PM/QD *complexes* with two PM/QD *conjugates*, prepared by Dr. A. Sukhanova. First, QD/PM complexes were assembled in the standard manner, and their fluorescence intensity was measured as a function of bR to QD molar ratio to provide a PL titration curve for this QD sample (panel A of Figure 5.15).

PM/QD conjugates were prepared by formation of a covalent bond between the $-\text{COOH}$ end group of the polymeric shell of CdSe/ZnS QDs and the $-\text{NH}_2$ groups of bR's amino acid residues. After purification, the concentrations of QDs and bR in these conjugates were

determined by least-squares deconvolution of the corresponding absorption spectra (as described in Chapter 2). Using the determined concentration values, the corresponding bR to QD molar ratios for the two conjugates were calculated to be 1.2 and 5.4 bR:QD.

After the normalisation of conjugate emission for QD concentration, which was slightly less than in PM/QD complexes, the fluorescence intensities of PM/QD complexes and conjugates of equal bR to QD molar ratios were compared (panel B of Figure 5.15). The fluorescence intensity of 1.2 bR to QD complex was quenched by ~18% compared to 41% quenching for the corresponding PM/QD conjugate, constituting a 2.3-fold increase in quenching efficiency. Similarly, a 24% quenching for the 5.4 bR/QD complex was enhanced to 42% (1.8-fold increase)¹.

Mutation of bacteriorhodopsin

The genetic modification of bacteriorhodopsin has been extensively used to optimise the protein for specific applications. A typical mutation involves replacement or removal of some amino acid residues in the protein's structure, stabilising the useful intermediate states through lengthening of their lifetime. In the D96N mutant, for example, the lifetime of the M-state is increased by orders of magnitude [50]. If QDs are coupled to the ground state of the bacteriorhodopsin (absorbs at 570 nm), such stabilisation of the M-state (absorbs at 420 nm) would certainly impact the FRET efficiency from QDs to the retinal molecule.

For instance, CdTe QD550 and QD600 have strong overlap with the ground state of the bacteriorhodopsin, but very little overlap with the absorption of the intermediate M state (Figure 5.16(a)). Both of these samples are efficiently quenched in PM/QD complexes containing the wild-type (WT) bacteriorhodopsin protein (panels B and C of Figure 5.16). When assembled with the D96N mutant, which, upon excitation, spends a significant amount of time in the M-state, the quenching of QDs' fluorescence by bacteriorhodopsin is significantly reduced. In fact, a maximum quenching of 15% was observed for QD550, while quenching of QD600 sample never exceeded 3%. The difference in behaviour for the two samples is due to both the smaller diameter of the QD550 and the slightly better spectral overlap of QDs' PL band with the M-state absorption.

¹ Note that the intensity of 5.4 bR to QD complex was estimated from a Boltzmann fit to the experimental PL titration curve (see panel A of Figure 5.15).

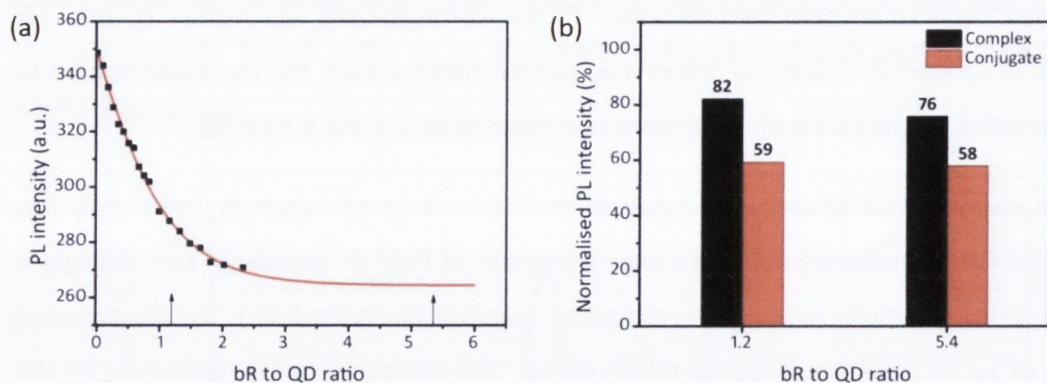


Figure 5.15 | Electrostatic assembly and chemical conjugation as methods of hybrid material preparation. (a) QDs' photoluminescence quenching by bR in PM/QD complexes as a function of bR to QD ratio. Black squares are experimental data, which was fitted with a Boltzmann curve, shown in red. The arrows indicated the bR to QD ratios of the two PM/QD conjugates. **(b)** Comparison of QDs' PL in PM/QD electrostatic complexes (black bars) and covalent conjugates (red bars). PL intensities were normalised to the intensity of QDs' emission in the absence of PMs.

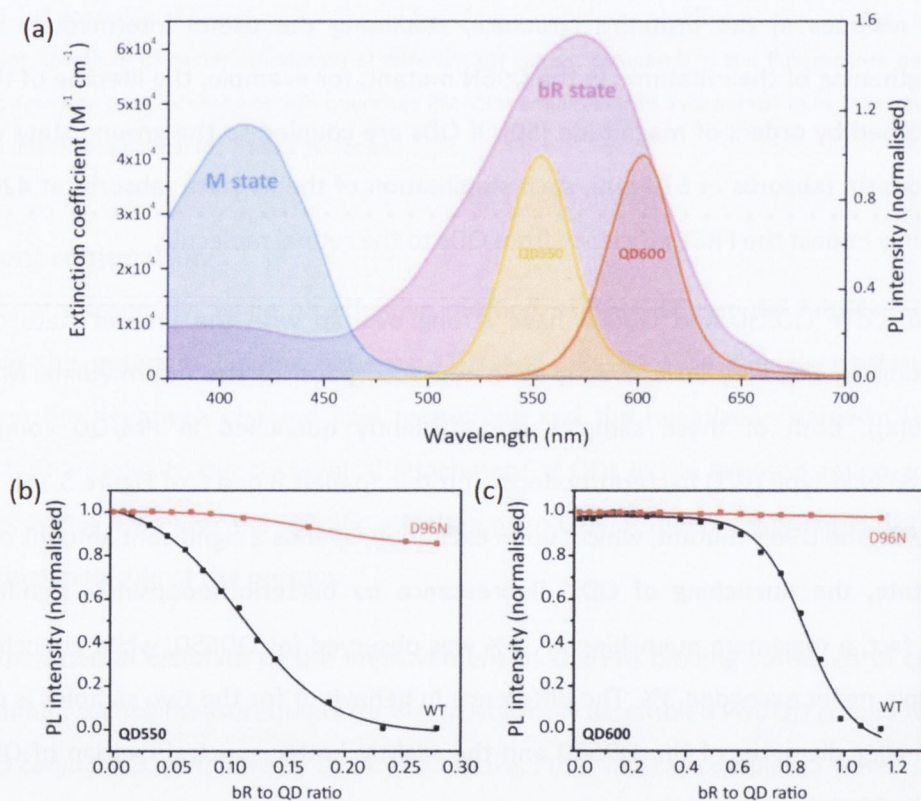


Figure 5.16 | Effect of genetic modification of bacteriorhodopsin. (a) Spectral overlap between the PL bands of CdTe QD550 and QD600 with the absorption spectra of the ground bR state (purple) and the intermediate M state (blue) of the bacteriorhodopsin. **(b) and (c)** Comparison of QDs' PL quenching by wild-type bR (WT, black) and D96N mutant (red) in **(b)** PM/QD550 and **(c)** PM/QD600 complexes.

5.4. Proton pumping

As a continuation of the above work, the first proof-of-principle measurements of the increase of the biological function of bR (proton pumping) in the presence of QDs were executed¹. This demonstration was done using oriented proteoliposomes (PTLs) - lipid vesicles (liposomes) with the bR protein molecules incorporated within the walls of these vesicles in a highly oriented manner [51]. PTLs with an average diameter of 57 nm were prepared according to the classical protocol of Racker & Stoeckenius [51]. The structural arrangement of bR proteins within the PTLs is similar to the bR packaging in native PMs. But, in contrast to the bacterial PM, where bR pumps protons out from the cell, the orientation of bR in the PTLs prepared according to the protocol of Racker & Stoeckenius is known to be opposite, so that the protons are pumped to the inside of the PTLs [52]. As a result, illumination of these structures provokes a photoinduced decrease of the proton concentration (increase of pH) in the solution outside of the PTLs. The photoinduced pH-response of the PTLs suspension was found to be reversible, with a complete relaxation of the system to the initial pH value upon switching off of illumination (panels B and C of Figure 5.17). The recorded value of the variation of pH at 2 kW/cm² illumination is typical for the preparation of extremely highly oriented bR-containing PTLs [52].

Hybrid PTLs/QD material was prepared by immobilisation of CdTe or CdSe/ZnS QDs on the surface of the PTLs (Figure 5.17(a)). Integration of CdTe QD590 within the PM at the one-to-five QD/bR molar ratio induces a pronounced (~25%) increase of the photoresponse of bR proton pumping (Figure 5.17(b)). On the other hand, the photoresponse of the CdSe QDs-containing hybrids was smaller (~15%) attributed to the increased donor-acceptor separation distance for this type of QDs due to the thickness of the PEG-COOH organic shell. However, this increase correlated well with the 17% decrease in CdSe/ZnS QD fluorescence for this bR-to-QD ratio, as well as with the FRET efficiency of ~18 % obtained from PL time-resolved data (data not shown, [3]).

¹ The preparation of PTLs and PTL/QD hybrids and measurements of proton pumping were performed by Vladimir Oleinikov (Shemyakin-Ovchinnikov Institute of Bioorganic Chemistry, Russian Academy of Sciences, Moscow, Russian Federation).

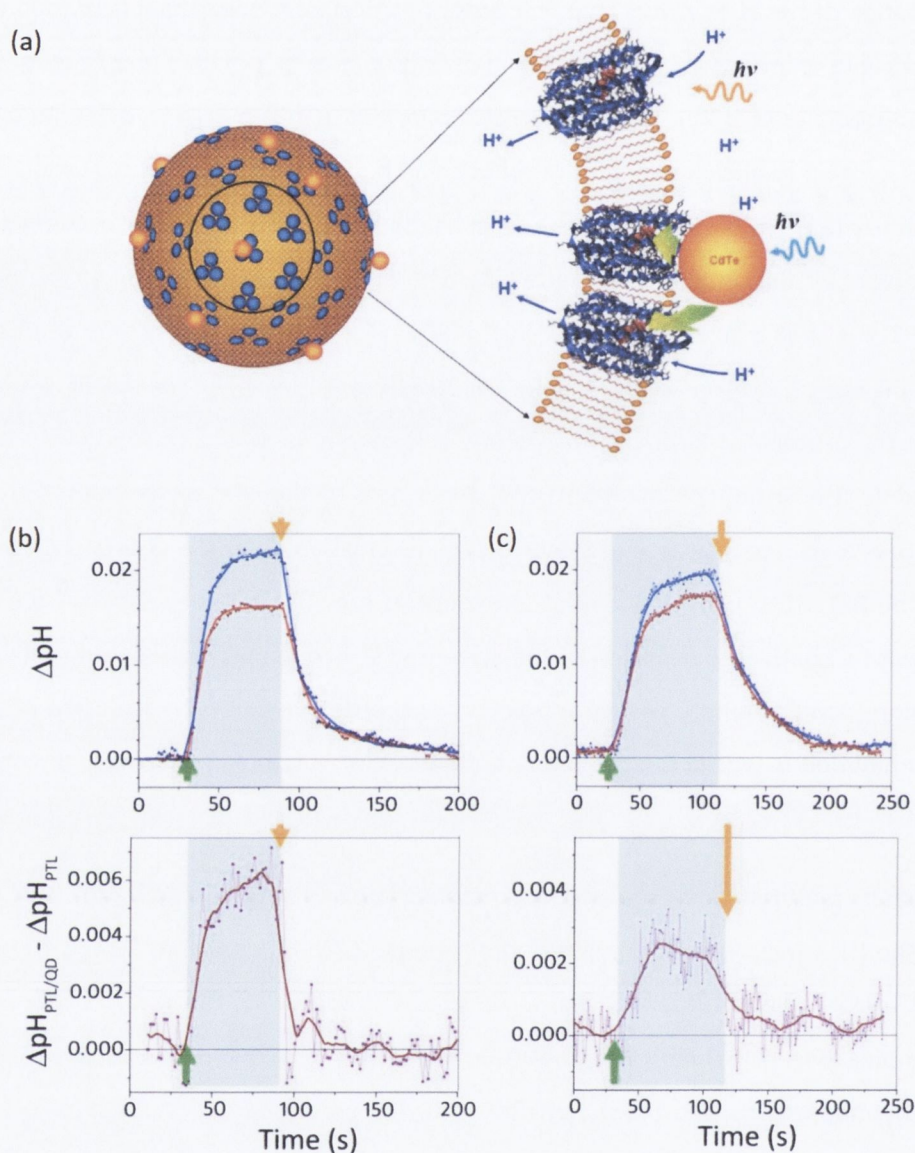


Figure 5.17] Proton pumping by bacteriorhodopsin in proteoliposomes and proteoliposome/quantum dot hybrids. (a) A diagrammatic representation of the PTL/QD hybrid material. Semiconductor QDs are immobilised on the surface of a PTL – a spherical lipid membrane (~57 nm in diameter), containing trimers of bacteriorhodopsin. The bR protein is unidirectionally oriented, and pumps protons from the outside to the inside of the PTL, causing changes in the pH of the outside solution. Energy collected and transfer by QDs to bR can enhance the rate of proton pumping. All objects are drawn to scale. **(b) and (c)** respectively show the effect of CdTe and CdSe/ZnS QDs on the efficiency of photoinduced proton pumping in PTL/QD hybrids, evaluated by measuring corresponding changes in the pH of the solution. Top graphs: when the white-light illumination was turned on (green arrows), the pH of the PTL suspensions increased (red lines). Turning off of the illumination (orange arrows) returned the system to the original pH value. Upon immobilization of QDs on top of PTLs, the proton pumping was further enhanced (blue lines) due to the energy transferred from QDs to bR. Bottom graphs show the differential pH curve, which is the difference in the photoresponses of the PTL/QD hybrids and pure PTL suspensions.

5.5. Conclusions

The retinal molecule in bR protein is the only chromophore of the PMs that absorbs light in the visible region. Properly chosen QDs can dominate over the intrinsic absorption of the bR in the 400-600 nm range by orders of magnitude (panel C of Figure 5.6). Furthermore, they play the role of a built-in light energy convertor by harvesting light which would not be absorbed efficiently by the purple membranes alone (from UV to blue region) and then transfer it to the bR, thereby enhancing the light-harvesting capability and, potentially, the quantum efficiency of the protein.

QDs were immobilized on the surface of PMs by covalent conjugation or by self-assembly through electrostatic interactions between the QDs and positive patches on PMs. Membrane-immobilized QD transfer the harvested energy via highly efficient FRET to this complex biological system. The energy transfer process was found to be influenced by a number of parameters, including QDs size, composition and mutation of bR, allowing optimisation of the PM/QD material. In addition, although QDs demonstrated highly efficient FRET to the bR protein, they have moderate extinction coefficients. Further optimization of the hybrid material can be done using semiconductor nanowires or nanorods which typically have very strong absorption.

Finally, a first proof-of-the-principle measurements were performed that bR, as part of the engineered QD-PM hybrid material, is able to utilize the additional energy transferred by QDs to improve the efficiency of its biological function – the proton pumping. Since the technologically exploitable (photoelectric, photochromic and photoelectric) properties of bR are coupled to its biological function, it is expected that an increased proton pumping efficiency can increase these properties and facilitate the integration of this material into photonic technologies.

References

1. Birge, R.R., et al., *Biomolecular electronics: protein-based associative processors and volumetric memories*. J. Phys. Chem. B **103**, 10746-10766 (1999)
2. Hampp, N. and D. Oesterhelt, *Bacteriorhodopsin and its potential in technical applications*, in *Nanobiotechnology* (Eds.: C.M. Niemeyer and C.A. Mirkin). pp. 146-167. WILEY-VCH, Weinheim (2004)
3. Rakovich, A., et al., *Resonance Energy Transfer Improves the Biological Function of Bacteriorhodopsin within a Hybrid Material Built from Purple Membranes and Semiconductor Quantum Dots*. Nano Lett. **10**, 2640-2648 (2010)
4. Hampp, N., *Bacteriorhodopsin as a Photochromic Retinal Protein for Optical Memories*. Chem. Rev. **100**, 1755-1776 (2000)
5. Lozier, R.H., R.A. Bogomolni, and W. Stoeckenius, *Bacteriorhodopsin: a light-driven proton pump in Halobacterium Halobium*. Biophys. J. **15**, 955-962 (1975)
6. Becher, B.M. and J.Y. Cassim, *Improved isolation procedures for the purple membrane of Halobacterium halobium*. Prep. Biochem. **5**, 161-178 (1975)
7. Oesterhelt, D. and W. Stoeckenius, *Isolation of the cell membrane of Halobacterium halobium and its fractionation into red and purple membrane*. Methods Enzymol. **31**, 667-678 (1974)
8. Lorber, B. and L.J. DeLucas, *Large scale preparation of homogeneous bacteriorhodopsin*. FEBS Lett. **261**, 14-8 (1990)
9. Wang, Z.H., et al., *Thickness determination of biological samples with a zeta-calibrated scanning tunneling microscope*. Proc. Natl. Acad. Sci. USA **87**, 9343-9347 (1990)
10. Nuss, M.C., et al., *Femtosecond spectroscopy of the first events of the photochemical cycle in bacteriorhodopsin*. Chem. Phys. Lett. **117**, 1-7 (1985)
11. Birge, R.R., *Protein-Based Optical Computing and Memories*. Computer **25**, 56-67 (1992)
12. Mathies, R., et al., *Direct observation of the femtosecond excited-state cis-trans isomerization in bacteriorhodopsin*. **240**, 777-779 (1988)
13. Pollard, W.T., et al., *Direct observation of the excited-state cis--trans photoisomerization of bacteriorhodopsin: Multilevel line shape theory for femtosecond dynamic hole burning and its application*. J. Chem. Phys. **90**, 199-208 (1989)
14. Wise, K.J., et al., *Optimization of bacteriorhodopsin for bioelectronic devices*. Trends Biotechnol. **20**, 387-394 (2002)
15. Trissl, H.W. and M. Montal, *Electrical demonstration of rapid light-induced conformational changes in bacteriorhodopsin*. Nature **266**, 655-657 (1977)
16. Chen, Z. and R.R. Birge, *Protein-based artificial retinas*. Trends Biotechnol. **11**, 292-300 (1993)
17. MIYASAKA, T., K. KOYAMA, and I. ITOH, *Quantum Conversion and Image Detection by a Bacteriorhodopsin-Based Artificial Photoreceptor*. **255**, 342-344 (1992)
18. Miyasaka, T. and K. Koyama, *Image sensing and processing by a bacteriorhodopsin-based artificial photoreceptor*. Appl. Opt. **32**, 6371-6379 (1993)
19. Caplan, S.R. and G. Fischer, *Photovoltaic behavior of bacteriorhodopsin-loaded cation-exchange membranes*. J. Membr. Sci. **16**, 391-405 (1983)
20. Oren, R., et al., *ATP synthesis catalyzed by the ATPase complex from Rhodospirillum rubrum reconstituted into phospholipid vesicles together with bacteriorhodopsin*. Arch. Biochem. Biophys. **205**, 503-509 (1980)

21. Winget, G.D., N. Kanner, and R. Efraim, *Formation of ATP by the adenosine triphosphatase complex from spinach chloroplasts reconstituted together with bacteriorhodopsin*. *Biochim. Biophys. Acta, Bioenerg.* **460**, 490-499 (1977)
22. Sigalat, C., B. Pitard, and F. Haraux, *Proton coupling is preserved in membrane-bound chloroplast ATPase activated by high concentrations of tentoxin*. *FEBS Lett.* **368**, 253-256 (1995)
23. Ryrie, I.J., C. Critchley, and J.-E. Tillberg, *Structure and energy-linked activities in reconstituted bacteriorhodopsin-yeast ATPase proteoliposomes*. *Arch Biochem. Biophys.* **198**, 182-194 (1979)
24. Oesterhelt, D., *Bacteriorhodopsin as a light-driven ion exchanger?* *FEBS Lett.* **64**, 20-2 (1976)
25. Kawata, S. and Y. Kawata, *Three-Dimensional Optical Data Storage Using Photochromic Materials*. *Chem. Rev.* **100**, 1777-1788 (2000)
26. Stuart, J.A., et al., *Volumetric optical memory based on bacteriorhodopsin*. *Synthetic Met.* **127**, 3-15 (2002)
27. Chen, Z., et al., *Advances in protein-based three-dimensional optical memories*. *Biosystems* **35**, 145-151 (1995)
28. Hampp, N., C. Bräuchle, and D. Oesterhelt, *Bacteriorhodopsin wildtype and variant aspartate-96' asparagine as reversible holographic media*. *Biophys. J.* **58**, 83-93 (1990)
29. Birge, R.R., *Photophysics and Molecular Electronic Applications of the Rhodopsins*. *Annu. Rev. Phys. Chem.* **41**, 683-733 (1990)
30. Song, Q.W., et al., *Chemically enhanced bacteriorhodopsin thin-film spatial light modulator*. *Opt. Lett.* **18**, 1373-1375 (1993)
31. Takeji, H. and N. Shimizu, *Nonlinear optical properties of a bacteriorhodopsin film in a Fabry-Perot cavity*. *Opt. Lett.* **19**, 248-250 (1994)
32. Hampp, N., et al., *Bacteriorhodopsin Variants for Holographic Pattern Recognition*, in *Molecular and Biomolecular Electronics* (Eds.: R.R. Birge). pp. 511-526. American Chemical Society (1994)
33. Okamoto, T., I. Yamaguchi, and K. Yamagata, *Real-time enhancement of defects in periodic patterns by use of a bacteriorhodopsin film*. *Opt. Lett.* **22**, 337-339 (1997)
34. Thoma, R., et al., *Bacteriorhodopsin films as spatial light modulators for nonlinear-optical filtering*. *Opt. Lett.* **16**, 651-653 (1991)
35. He, J.-A., et al., *Bacteriorhodopsin Thin-Film Assemblies—Immobilization, Properties, and Applications*. *Adv. Mater.* **11**, 435-446 (1999)
36. Lao, K. and A.N. Glazer, *Ultraviolet-B photodestruction of a light-harvesting complex*. *Proc. Natl. Acad. Sci. USA* **93**, 5258-5263 (1996)
37. Danon, A. and P. Gallois, *UV-C radiation induces apoptotic-like changes in Arabidopsis thaliana*. *FEBS Lett.* **437**, 131-136 (1998)
38. Archer, M.D. and J. Barber, *Photosynthesis and Photoconversion*, in *Molecular to Global Photosynthesis* (Eds.: M.D. Archer and J. Barber). pp. 1-41 Imperial College Press, London (2004)
39. Bolton, J.R., *Solar energy conversion in photosynthesis – features relevant to artificial systems for the photochemical conversion of solar energy*, in *Solar energy: Chemical conversion and storage* (Eds.: King J.B, Hautala R.R, and K. C.R). pp. 31-50. Humana Press, Inc., Clifton, N.J. (1979)
40. Willard, D.M., et al., *Directing energy flow through quantum dots: towards nanoscale sensing*. *Anal. Bioanal. Chem.* **384**, 564-571 (2006)
41. Sukhanova, A., et al., *Controlled self-assembly of nanocrystals into polycrystalline fluorescent dendrites with energy-transfer properties*. *Angew. Chem. Int. Ed.* **45**, 2048-52 (2006)

42. Nabiev, I., R.G. Efremov, and G.D. Chumanov, *The chromophore-binding site of bacteriorhodopsin. Resonance and surface-enhanced resonance Raman spectroscopy and quantum chemical study.* J. Biosciences **8**, 363-373 (1985)
43. Clapp, A.R., I.L. Medintz, and H. Mattoussi, *Forster resonance energy transfer investigations using quantum-dot fluorophores.* Chemphyschem. **7**, 47-57 (2006)
44. Rogach, A.L., et al., *Aqueous synthesis of thiol-capped CdTe nanocrystals: State-of-the-art.* J. Phys. Chem. C **111**, 14628-14637 (2007)
45. Yu, W.W., et al., *Experimental determination of the extinction coefficient of CdTe, CdSe, and CdS nanocrystals.* Chem. Mater. **15**, 2854-2860 (2003)
46. Szundi, I. and W. Stoeckenius, *Surface pH controls purple-to-blue transition of bacteriorhodopsin. A theoretical model of purple membrane surface.* Biophys. J. **56**, 369-83 (1989)
47. Muller, D.J., et al., *Imaging purple membranes in aqueous solutions at sub-nanometer resolution by atomic force microscopy.* Biophys. J. **68**, 1681-1686 (1995)
48. Lakowicz, J.R., *Energy Transfer*, in *Principles of Fluorescence Spectroscopy* (Eds.: J.R. Lakowicz). pp. 443-475. Springer, New York (2006)
49. Birnbaum, D. and S. Seltzer, *A highly reactive heteroatom analog of retinal and its interaction with bacteriorhodopsin.* Photochem. Photobiol. **39**, 745-752 (1984)
50. Miller, A. and D. Oesterhelt, *Kinetic optimization of bacteriorhodopsin by aspartic acid 96 as an internal proton donor.* Biochim. Biophys. Acta - Bioenerg. **1020**, 57-64 (1990)
51. Racker, E. and W. Stoeckenius, *Reconstitution of Purple Membrane Vesicles Catalyzing Light-driven Proton Uptake and Adenosine Triphosphate Formation.* J. Biol. Chem. **249**, 662-663 (1974)
52. Oesterhelt, D. and W. Stoeckenius, *Functions of a New Photoreceptor Membrane.* PNAS **70**, 2853-2857 (1973)

6. NONLINEAR OPTICAL PROPERTIES OF QUANTUM DOT/BACTERIORHODOPSIN MATERIAL

In the previous chapter, the first studies of the nanoscale interactions between semiconductor quantum dots and bacteriorhodopsin protein within purple membranes were described. It was shown that these interactions, in the form of FRET, lead to an improvement of the biological function of bR. The observed effects indicate that that improvement of bR's photoelectric and photochromic properties can also be achieved. Recent reports exist that explore this possibility. In particular, Griep *et al.* [1] have shown that the photoelectric response of bacteriorhodopsin films can be increased by up to 35% by addition of QDs.

Many of the optical applications of bacteriorhodopsin are based on its strong nonlinear properties, which are coupled to the photochromic properties of this protein [2]. As such, the experimentally observed improvement of the biofunction of bacteriorhodopsin in the presence of QDs should influence the nonlinear properties of the bR protein. This chapter details the initial investigations of the nonlinear properties of PM suspensions and solutions containing the hybrid PM/QD material using the Z-scan technique. Z-scan was chosen as the method of measurements of the nonlinear optical (NLO) properties both due to the ease of the technique and the ability to perform measurements on liquid samples.

6.1. Nonlinear properties of materials

The optical properties of some materials display nonlinear dependencies on the intensity of incident excitation. In particular, the absorption and refractive properties of such materials demonstrate significantly different behaviour at high incident light intensities. At high intensities, samples possessing nonlinear absorption (NLA) properties absorb either less or more than expected for a linear behaviour (Figure 6.1(a)). In samples with nonlinear refraction properties, the refractive angle is either increased or decreased as the intensity of the incident light is increased (Figure 6.1(b)).

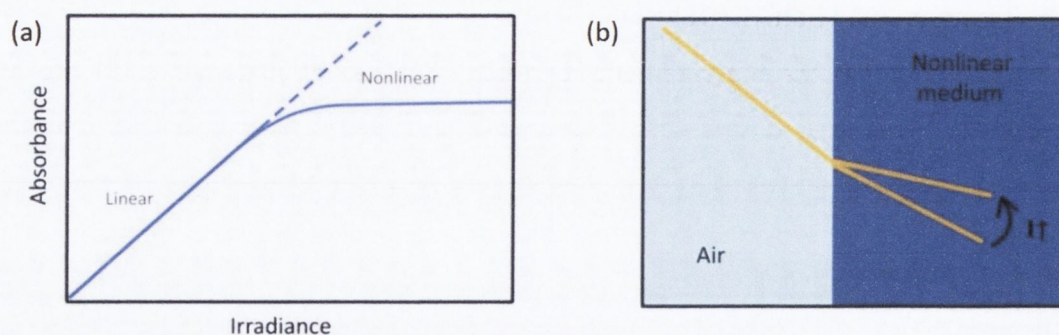


Figure 6.1|Nonlinear optical behaviour of materials. (a) At low intensities, the absorption of a sample with nonlinear absorption properties follows a linear dependence. Above a certain threshold value, however, the absorbance of such a sample starts to deviate from the linear behaviour (the nonlinear absorptive region). In the example shown, the sample absorbs less than expected at high intensities. **(b)** In a nonlinear refractive medium, the refraction of the incident beam depends on the irradiance. For a sample with negative lensing, the angle of refraction decreases as incident beam intensity increases.

Bacteriorhodopsin films show a very significant nonlinear absorption and refraction response under illumination. Both of these effects can be attributed to the different conformations of the bR's intermediate states. The small changes of the crystalline structure of bR upon illumination as well as the accompanying shifts in electron density result in significant changes in dipole moments with subsequent shifts of bR's absorption band and also changes in its refractive index [3]. These properties can be exploited for a variety of optical applications, such as optical limiting and several of types of holographic applications.

The nonlinear refractive properties of the bacteriorhodopsin are usually described in terms of a three-level scheme [3, 4] involving the ground state (bR), a short-lived intermediate state (a combination of K and L state) and a long-lived intermediate state (M), all of which possess different refractive and absorption indices. Since the lifetimes of the states and the excitation and relaxation efficiencies between them depend on the environmental conditions (e.g. pH value, temperature, bR mutation), the nonlinear properties of bacteriorhodopsin show a similar dependence. For example, the refractive index of the D96N bacteriorhodopsin mutant changes significantly less when compared to the wild-type bR [5].

6.2. The Z-scan technique

Several methods for the measurements of NLO properties of materials exist, the most common of which are Z-scan and phase-modulated beams techniques. Each of these techniques has their own merits. The advantages of the Z-scan technique are the ease of its implementation and the fact that it can be applied to both liquid and solid samples.

The basis of the Z-scan is the positional dependence of the irradiance of a laser beam focused by a converging lens and the intensity-dependence of the NLO properties of the material. In a typical Z-scan set-up, a laser beam is focused by a lens (Lens 1 in Figure 6.2) and a thin sample is moved through the focal position of the focused beam, while the transmittance of this beam through an aperture placed in the far-field is measured. The converging/diverging profile of the focused laser beam provides a variation in the intensity of illumination incident onto the sample, and therefore changes in position of the sample relative to the focal point of the beam translate into transmittance changes through a far-field aperture, which are measured by a detector placed behind the aperture (Detector 1 in Figure 6.2).

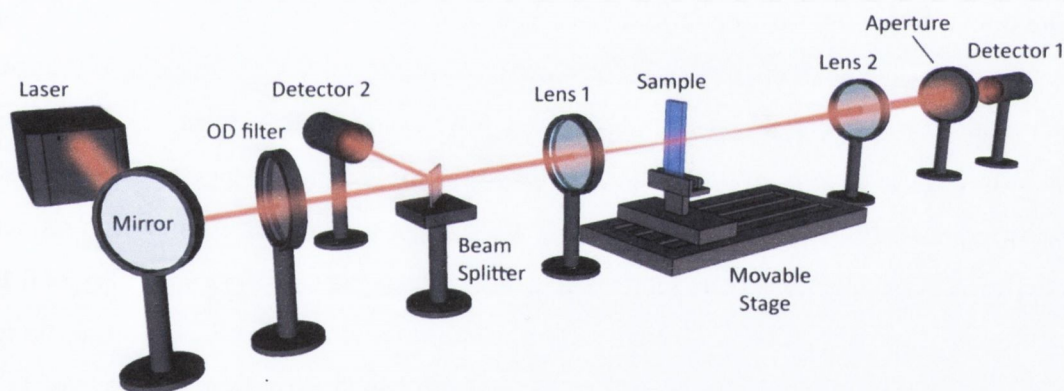


Figure 6.2 | A typical Z-scan set-up. The intensity of the laser is adjusted with OD filter. The beam splitter separates the laser beam into reference and main beams. The reference signal is measured by Detector 2, and is used to correct the data for laser intensity fluctuations. The main beam is focused by Lens 1 and is later collimated by Lens 2, before passing through an aperture in the far-field. The sample is moved along the optical path of the focused measurements beam (Z direction), and the transmittance changes due to the sample are measured by Detector 1.

6.2.1. Measurements of nonlinear absorption and refraction

There are two main configurations of the Z-scan technique – the open- and closed-aperture Z-scans. The configuration described above is that of a closed-aperture Z-scan, in which both nonlinear refraction (NLR) and nonlinear absorption (NLA) contributions are measured. In open-aperture Z-scans, the far-field aperture is either removed or it is opened so that its

transmission is close to unity. This configuration only measures the NLA contributions to transmission changes.

Consider, for example, a sample displaying only nonlinear absorption. At high intensities, such a sample absorbs either more or less than a sample with linear optical properties (Figure 6.1(a)). At low incident intensities, however, the absorption follows a linear dependence. In a Z-scan, when the sample is far away from the focal point of the laser beam, the irradiance of the laser is not enough to invoke the nonlinearity. As the sample is brought close to the narrowest part of the beam ($Z=0$), the NLA becomes stronger and the sample starts to transmit either more or less light. The effect is strongest at the $Z=0$ position, resulting in a Lorentzian-type peak in the transmission versus Z position trace (Figure 6.3(a)), termed the Z-scan trace. The changes in transmission due to the NLA are observed in both the open- and the closed-aperture because NLA does not affect the path of the laser beam. However, in closed-aperture Z-scans, the height of the NLA peak is proportional to the aperture transmittance.

A sample with non-linear refraction properties acts as an additional intensity-dependent lens with either positive or negative lensing that either increases or decreases the refractive angle. For a focused incident beam, this either diverges or converges the beam resulting in changes in the irradiance of the laser beam as it reaches the detector in the far field (Figure 6.3(b)). When an aperture is placed in front of the detector (closed-aperture Z-scan), these changes translate into changes in transmittance. For example, if a sample has negative non-linear refractive index, it will act as an intensity-dependent lens that reduces the refractive angle (Figure 6.1(b)) and diverges the incident beam. During a Z-scan, when the sample is far away from the focal plane, the irradiance within the sample is low and the non-linear effect is negligible. As the sample is moved closer to the focal plane the irradiance increases giving rise to non-linear effects. Before the focal plane, the divergence of the beam by the nonlinear optical sample results in light of higher intensity being transmitted through the aperture in the far field (top panel of Figure 6.3(b)). After the focal plane, the effect is opposite – the beam divergence gives rise to smaller power densities at the aperture (bottom panel of Figure 6.3(b)). The result is a typical Z-scan trace (Figure 6.3(c)) consisting of a peak and a valley that correspond to increased and decreased transmittance through the aperture before and after the focal plane respectively. For a positive non-linear refractive index material, an opposite valley-peak arrangement is expected for a Z-scan trace, allowing the determination of the sign of the non-linearity of the refractive index of material directly from the raw Z-scan data.

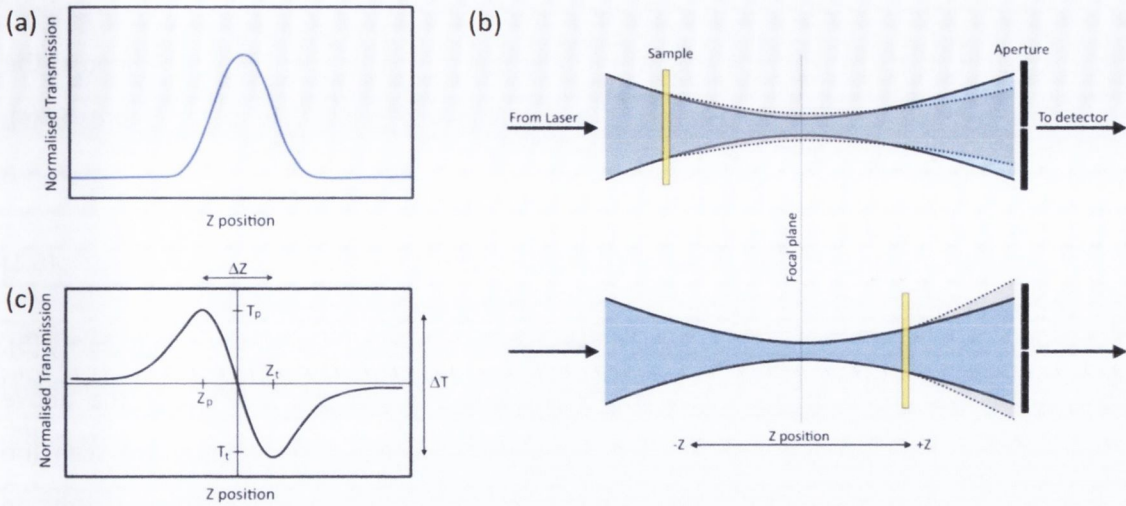


Figure 6.3 | Measurements of nonlinear optical properties using Z-scans measurements. (a) Representative open-aperture Z-scan trace for a sample with NLA properties. During a Z-scan, an NLA sample transmits more near the narrowest part of the beam where the irradiance values are highest, resulting in a Lorentzian profile of the Z-scan trace. (b) Refraction of the focused laser beam by a sample with negative lensing properties at different Z positions relative to the focal plane of the collimating lens (lens 1 in Figure 6.2). Before the focal plane (top figure), the divergence of the incident beam is decreased by the negative lensing resulting in increased beam irradiance at the aperture. After the focal plane (bottom figure), the effect is opposite. The divergence increases and therefore beam irradiance decreases. (c) A typical Z-scan trace for a sample with negative lensing, showing a peak and a trough in transmittance corresponding to the pre- and post-focal position of the sample in (b). The difference in peak-to-trough transmission ($\Delta T = T_p - T_t$) depends on the nonlinear refractive index n_2 , while $\Delta Z (= Z_t - Z_p)$ is determined by the properties of the focusing lens of the Z-scan set-up (Lens 1 in Figure 6.2).

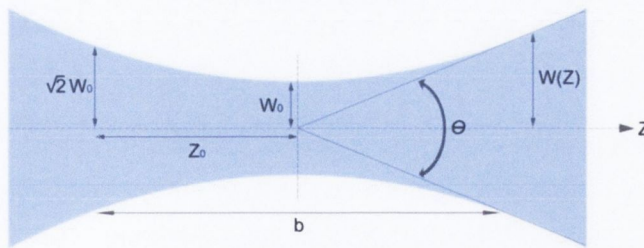


Figure 6.4 | Representative cross-section of a focused laser beam. A Gaussian beam is characterised by beam waist w_0 , a divergence angle θ and Rayleigh width Z_0 , at which the width of the beam is equal to $\sqrt{2} w_0$, and which is half the depth of focus (b) of the beam.

6.2.2. Extraction of nonlinear coefficients from Z-scan data

The overall amplitude of the transmittance changes due to nonlinear refraction, defined as the difference in the peak and trough transmission values ($\Delta T_{p-t} = T_p - T_t$) in Figure 6.3(c), depends on the transmittance of the aperture (S):

$$\Delta T_{p-t} = 0.406 (1 - S)^{0.25} |\Delta\Phi_0| \quad (6.1)$$

where $\Delta\Phi_0$ is the on-axis phase change at the focus caused by the third-order non-linearity [6]. In a closed-aperture scan both NLA and NLR make a contribution, however the above expression assumes the absence of nonlinear absorption. For an open-aperture scan (no aperture, $S=1$), the NLR plays no role in the transmitted intensity, and only NLA is measured. In this case, the transmittance as a function of Z position ($T(Z)$) is given by

$$T(Z) = 1 + \frac{q_0}{2\pi} \left(\frac{1}{Z^2 + Z_0^2} \right) \quad (6.2)$$

Here $q_0 = \beta L_{eff} I_0$, where β is the nonlinear absorption index (cm W^{-1}) and L_{eff} is the effective sample thickness, given by $(1 - e^{-\alpha L})/\alpha$ where L is the actual thickness of the sample and α is the linear absorption coefficient of the material.

Alternatively, both the NLA and NLR contributions can be calculated directly from the normalized transmittance ($T(x)$) curve by fitting the closed-aperture Z-scan trace to the following equation [7]:

$$T(x) = 1 + \frac{2(-\rho x^2 + 2x - 3\rho)}{(x^2 + 9)(x^2 + 1)} \Delta\Phi_0 \quad (6.3)$$

Here, $x = Z/Z_0$ where Z is the position of the sample relative to focal plane and Z_0 is the diffraction length of the focused beam ($= k(w_0)^2/2$), where $k = 2\pi/\lambda$ is the wavevector and w_0 is the radius of the beam waist (Figure 6.4). ρ is a parameter that relates the phase changes caused by non-linear absorption ($\Delta\Psi_0$) and nonlinear refraction ($\Delta\Phi_0$) or, equivalently, the nonlinear absorption and nonlinear refraction (n_2) indices:

$$\rho = \frac{\Delta\Psi_0}{\Delta\Phi_0} = \frac{\beta}{2k n_2} \quad (6.4)$$

The nonlinear refractive index (n_2) and the associated phase change ($\Delta\Phi_0$) are related by $\Delta\Phi_0 = k n_2 I_0 L_{eff}$, where I_0 is the on-axis irradiance at the focus position. Similarly, the nonlinear absorption index can be calculated from the corresponding on-axis phase shift using $\Delta\Psi_0 = \beta I_0 L_{eff}/2 = q_0/2$.

6.2.3. Z-scan set-up

Z-scan measurements were performed at several wavelengths, using a LTS150 motorised stage (ThorLabs). The laser beam was focused and collimated by bi-convex spherical lenses (ThorLabs). The wavelength of the pulsed laser beam from a Verdi V10 laser (<130 fs, 80 MHz, Coherent) was set to 550 - 800 nm using the Mira 900/Mira-OPO system (Coherent). The intensity of the incident beam was adjusted using a series of neutral density filters (NT59 series, Edmund Optics). The intensities of the reference beam and the transmitted measurement beam were measured using two silicon photodiodes (SM05PD1B, ThorLabs) amplified by two photodiode amplifiers (PDA200C, ThorLabs). These intensities were recorded as a function of sample position using a LabView program that incorporated the ThorLabs software for the motorised stage. The measured transmitted intensity was first corrected for laser fluctuations by dividing it by the intensity of the reference beam. After being normalised to transmission at the Z=0 position, the corrected Z-scan trace was fitted to equation 6.3 to extract the values of phase changes due to the NLA and NLR properties.

6.3. Optical nonlinearities in bR/QD material

The hypothesis that the enhancement of the biological function of bacteriorhodopsin in the presence of QDs can result in enhancement of its nonlinear optical properties was tested on an example of a bR/QD hybrid material assembled from wild-type bR and TGA-stabilised CdTe QDs emitting at ~ 650 nm. This QD sample was chosen because it displayed efficient FRET coupling to the bR protein. Furthermore, this sample had relatively high extinction coefficients (Figure 6.5) due to the larger size of the QDs, allowing for larger NLA properties when compared to smaller QDs with potentially better FRET coupling. The effect of the addition of QDs on the NLO properties of PMs was then studied through comparative studies involving Z-scans of pure QDs solutions, PM suspensions and aqueous solutions of assembled PM/QD material.

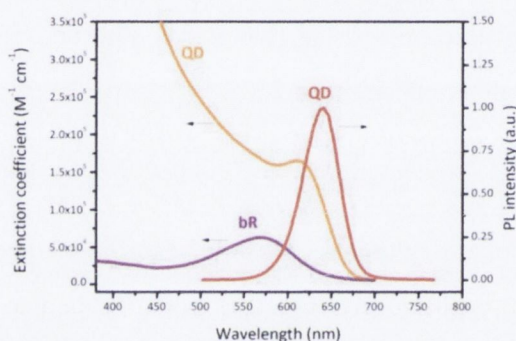


Figure 6.5| Comparison of spectral properties of QD650 and bacteriorhodopsin protein. The extinction coefficient of the QD650 sample, used in the study of the NLO properties of QD/PM complexes, is significantly higher than that of the retinal molecule of the bR protein. The absorption band of the retinal molecule has significant spectral overlap with the QD650 emission spectrum, allowing for strong optical coupling of QDs and PMs.

6.3.1. Assembly of PM/QD complexes

The PM/QD650 complexes were self-assembled and purified in a standard manner, as described in Chapter 5 [8]. The assembly was monitored by absorbance measurements above the QDs' and bR's absorption edges. At these wavelengths, the main contribution being measured is scattering, which has a strong dependence on the average size of the particles. Temporal absorbance measurements of PMs/QD650 complexes at 700 nm showed increased scattering by the self-assembling complexes (Figure 6.6(a)). The scattering reached saturation after ~ 1 hour, corresponding to the end of the assembly process and remained constant thereafter.

QD/PM assembly was also monitored by temporal fluorescence measurements. This was possible due to the fact that QDs, self-assembled on top of PMs and illuminated with UV or visible light, transfer the energy they absorb to the retinal molecule of the bacteriorhodopsin protein via FRET [8]. The FRET process results in increasingly quenched emission from the PM/QD650 complexes (lower left axis, Figure 6.6(b)) as the assembly proceeds. Furthermore, fluorescence measurements revealed the bR-to-QD ratio dependence of the strength of optical interaction between the QDs and the retinal molecule (i.e. the strength of FRET coupling). For PM/QD650 system, efficient FRET coupling was achieved for bR-to-QD ratios as small as 0.2, even after only a few minutes of the assembly process (Figure 6.6(b)).

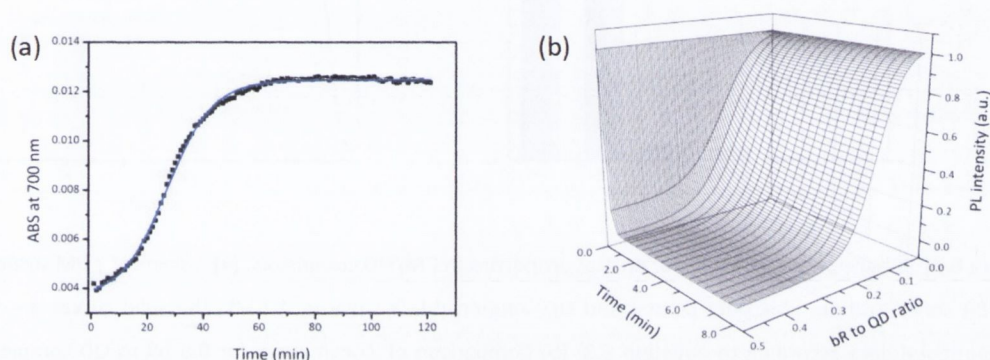


Figure 6.6| Self-assembly of PM/QD650 complexes monitored by (a) absorption and (b) photoluminescence measurements. (a) Scattering from 0.5 bR-to-QD complexes increased as QDs and PMs assembled in solution. Scattering reached saturation after ~ 1 hour, corresponding to the end of the assembly process. It then remained constant for at least another hour. (b) The quenching of QDs' fluorescence depends on the bR to QD molar ratio. For any chosen ratio, quenching increased with time as QDs and PMs electrostatically assemble in solution. 100% quenching was achieved for bR-to-QD molar ratios above 0.2, suggesting strong interactions between QDs and bR within the 0.2 – 0.5 bR-to-QD molar ratio range.

6.3.2. Enhancement of nonlinear optical properties of bacteriorhodopsin

In view of the strong FRET coupling for PM/QD650 complexes with bR-to-QD molar ratios above 0.2, it is reasonable to assume that, if nanoscale interactions between QDs and bR can result in the improvement of NLO properties of bR, then such enhancement would be most pronounced within this bR-to-QD molar ratio range. On the other hand, the enhancement effect should be small in complexes with bR-to-QD ratios smaller than 0.2. In view of this, four bR-to-QD ratios were chosen (0.02, 0.1, 0.25, 0.5), which covered the whole range of the strength of optical interactions between the bR protein and QDs in the PM/QD complexes.

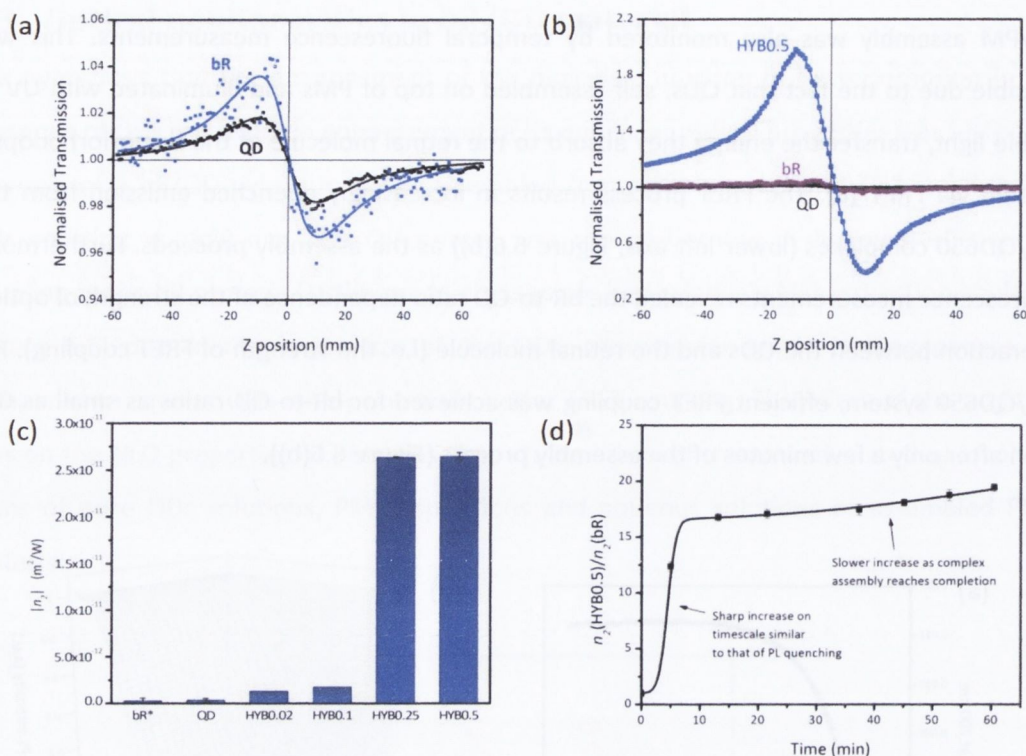


Figure 6.7] Enhancement of nonlinear optical properties in PM/QD complexes. (a) Z-scans of a PM suspension (0.5 μM bR concentration, blue data points) and QD solution (black squares, 1 μM). The solid curves are fits to the experimental data according to equation 6.3. **(b)** Comparison of Z-scan curve for 0.5 bR-to-QD complex (HYB0.5, blue) and Z-scans of the components – same as those shown in (a). **(c)** Nonlinear refractive indices of bR, QD and four of PM/QD complexes of different bR-to-QD ratios (labelled HYB, followed by the bR-to-QD ratio). An increase of n_2 was obtained for all bR-to-QD ratios, with maximum increases for bR-to-QD ratios above 0.2 (consistent with PL quenching data). The concentration of QDs was the same in all complexes (1 μM). The bR concentration in the PM sample (bR*) is the average of the four concentrations of bR in hybrid complexes (0.22 μM). **(d)** Temporal evolution of the NLR index of the 0.5 bR-to-QD complex relative to the NLR index of the PM suspension containing same bR concentration (0.5 μM). The initial sharp increase of n_2 occurred on the same timescale as the PL quenching observed during HYB0.5 complex assembly (Figure 6.6(b)). The increase slowed down as assembly reached completion. The enhancement of n_2 reached a maximum of ~ 20 relative to the NLR index of PM suspension or ~ 40 relative to NLR index of QD solution.

Closed-aperture Z-scans at 700 nm of a pure QD solution and a PM suspension showed that both these samples display negative lensing at 700 nm (Figure 6.7(a)), in accordance with literature [5, 9, 10]. Upon QD/PM assembly, there was a significant increase in the transmittance variations (Figure 6.7(b)) corresponding to considerable increase in the amplitude of the NLR index (n_2) of the bR-QD system (Figure 6.7(c)). For example, for the 0.5 bR-to-QD complex, $|n_2|$ increased from $-6.07 \times 10^{-13} \text{ m}^2/\text{W}$ for the PM suspension and $3.29 \times 10^{-13} \text{ m}^2/\text{W}$ for the QD650 solution to $1.32 \times 10^{-11} \text{ m}^2/\text{W}$. This is equivalent to ~ 20 - and 40 -fold increase of the NLR index of the PM suspension and the QD solution respectively.

Enhancement of n_2 was significantly lower for PM/QD complexes with bR-to-QD molar ratios below 0.2 (Figure 6.7(c)), similar to PL quenching efficiencies in these complexes.

Temporal evolution of n_2

The results described above are not sufficient to establish the physical coupling between QDs and bR as the cause of the observed enhancement effect. Since these optical effects are by definition nonlinear, the combination of two nonlinear media may result in a further enhanced nonlinear effect. So, even though the concentration of QDs in all complexes was same, the observed dependency of n_2 on the bR-to-QD molar ratio could be the result of the cumulative effect of the NLR properties of the QD solution and the PM suspensions of different concentrations. In this instance, the enhancement effect is expected to be immediate, with no temporal evolution after the initial mixing of QDs and PM solutions. This was not found to be the case. In fact, temporal Z-scan measurements showed that increase of n_2 follows a temporal trend similar to that observed during the fluorescence quenching measurements, used to monitor the assembly of the PM/QD – both measurements showed strong changes within the first 10 minutes, followed by much slower changes thereafter (Figure 6.7(c)). This result implies that the amplitude of the NLR index of the PM/QD complex is larger than the cumulative effect of the NLR indices of the constituents.

Effect of QD aggregation

Another possible source of the n_2 enhancement with the observed molar ratio dependency is the aggregation of QDs. There have been reports in the literature that aggregation of *metallic nanoparticles* can cause increases in the optical nonlinearity of a sample due to the red-shifting of existing bands or an appearance of new plasmonic bands, red-shifted to the original ones [11, 12]. By extension, it is reasonable to assume that *semiconductor nanocrystals* may show a similar behaviour. Although no such effect has as yet been reported in the literature, the concentration-dependence of the optical properties of semiconductor nanocrystals has been observed. Artemyev *et al.* [13] showed that the absorption spectrum of QDs in a concentrated sample (referred to as a denser state) red-shifts relative to a dilute sample.

Now, the self-assembly of PM/QD complexes can be thought of in terms of a formation of a denser state of QDs. An important thing to note, however, is that assembly of PM/QD complexes involving a well-dispersed QD sample would be significantly different to the assembly behaviour of an aggregated QD sample. Furthermore, the increase of the n_2 due to the assembly would be significantly less for the aggregated sample since QDs in this sample are already in a dense state. As a result, the comparison of temporal n_2 evolution during the

assembly of PM/QD complexes for a well-dispersed (WD) and an aggregated (AGR) QD samples provides a way to evaluate whether or not the formation of a denser state of QDs is responsible for the enhancement of NLO properties.

In order to perform these comparative measurements, an aggregated QD sample had to be prepared first. It was crucial to perform the aggregation in a controlled manner – aggregated QDs must remain to be soluble to allow their assembly with the PMs. A more typical case is one where QDs' aggregation leads to the irreversible precipitation of QDs out of the solution. Several methods of aggregating QDs were attempted.

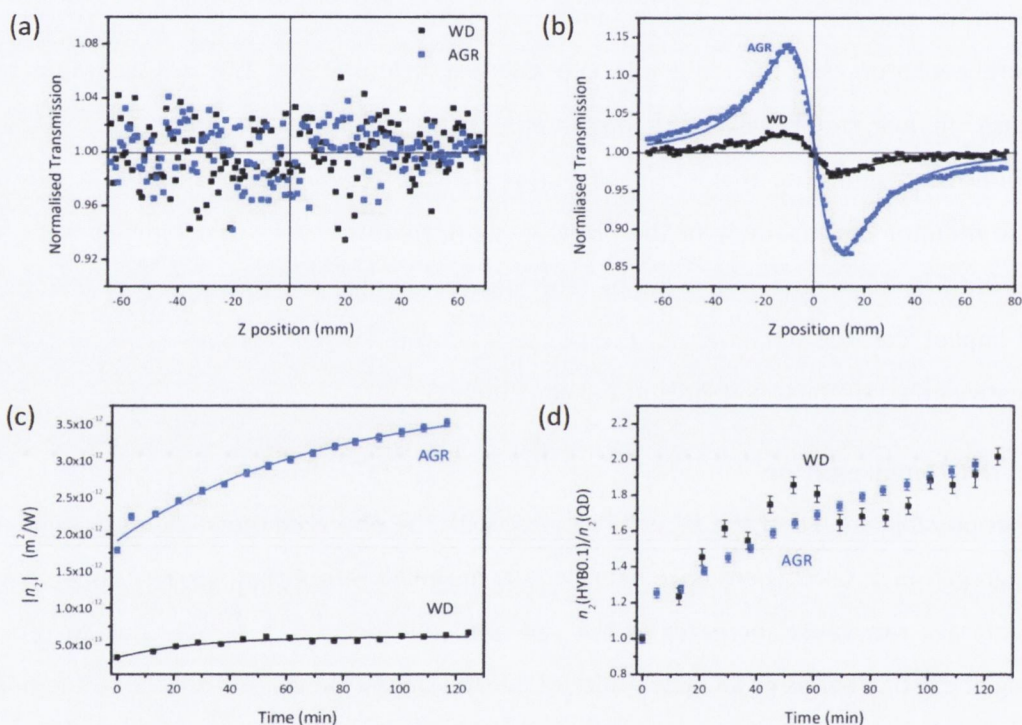


Figure 6.8| Effect of QD aggregation on nonlinear properties of PM/QD complexes. (a) Z-scan curves of a well-dispersed (WD) QD sample and an aggregated (AGR) QD sample prepared by centrifuge filtration of the WD sample. The WD sample produced by this method was of very low concentration, resulting in large noise and no noticeable signal in Z-scan data. (b) Z-scan curves of WD sample and AGR QD samples prepared by prolonged gentle heating of the WD sample. The aggregation caused a significant increase (~5-fold) in the NLR properties of the QD sample. (c) and (d) show temporal evolution of the NLR index of 0.1 bR-to-QD complex. The absolute values of n_2 were significantly larger for complexes assembled with the AGR QD sample (c), due to the larger NLR index of this QD sample. However, when n_2 values were normalised to NLR indices of QD samples, the overall trend in the temporal evolution of n_2 was found to be same for both AGR and WD QDs (d), suggesting that aggregation is not the cause of the enhancement effect.

First, QDs sample was separated into an “aggregated” (AGR) and “well-dispersed” (WD) samples by centrifuge filtration through an eppendorf filter with $0.2 \mu\text{m}$ pore size (3 min, at 10,000 rpm). QD precipitate, which was left on the filter, was re-dissolved in water to provide the AGR sample. The rest of the solution, which went through the filter, was collected as a WD sample. Since the concentration of the WD sample was significantly less than that of the AGR sample, the AGR sample was diluted until the concentration of QDs in both samples was equal. The WD sample was sonicated for ~ 15 min prior to Z-scan measurements to ensure best dissolution of QDs in this sample. However, due to fairly low concentrations of both of these samples, the noise in the Z-scan measurements was very high (Figure 6.8(a)) and no significant nonlinear effects were observed for either of these samples.

Other methods of aggregating the QD sample were attempted next, but most proved to be unsuccessful: the sonication of a QD solution of high concentration had no effect on its nonlinear properties; excessive evaporation of solvent lead to a sudden precipitation of nanocrystals out of solution and lowering of the pH below 7 had a similar effect. In both of these cases, precipitation of QDs was found to be irreversible.

Finally, it was found that gentle and prolonged heating of the sample ($\sim 25^\circ\text{C}$ for ~ 48 hours) caused the sample to form an aggregated state without immediate precipitation¹⁹. After this treatment, the assembly of the 0.1 bR:QD complex was monitored over a period of 2 hours for the AGR and the WD QDs samples. First of all, it was found that the NLR index of the AGR QD sample was approximately 5 times larger than that of the WD QD sample (Figure 6.8 (b) and (c)). As a result, the overall values of $|n_2|$ of the PM/QD complexes were significantly larger for the AGR QD sample (Figure 6.8(c)). However, both AGR and WD samples produced same trends in terms of the increase of $|n_2|$, which was clearly seen when n_2 values were normalised to the initial QD value (Figure 6.8(d)). This is in contradiction to what was discussed above and suggests that, although the aggregation does influence the amplitude of $|n_2|$, it does not play a role in determining the overall increase of the NLR index for a given complex. This leads to the conclusion that neither QDs aggregation nor, in fact, the formation of a denser state of QDs is the cause of the enhancement of NLR in PM/QD complexes.

It is well-known that colloidal QD samples naturally aggregate over time; thus, it is very important to account for the significant increase of the nonlinear properties of aggregated QDs when analyzing the nonlinear properties of the PM/QD hybrid material. The simplest way to achieve this is to normalise the n_2 values of the PM/QD complexes to the NLR index of the QD

¹⁹ After this treatment, the QDs fall out of solution and precipitate within 2 days

solution. For this reason, all further increases of n_2 were assessed in terms of the enhancement of the QDs' NLR properties and not in terms of the increase of bR's NLR index.

6.3.3. Origin of n_2 enhancement

Having eliminated the "macroscopic" interactions (cumulative nonlinear effect and aggregation) as the source of n_2 enhancement, it is likely that some sort of nanoscale interaction between the QDs and bR protein at the QD/membrane interface is the cause of the observed effect.

The nature of these interactions is not immediately clear – both physical and chemical effects are possible. The NLO properties of bR are derived from its photochromic properties and, in particular, from the different absorption and refractive properties of its intermediate state. As a result, the strong optical coupling that exists between bR and QDs when PM/QD complexes are illuminated with UV or visible light can in fact lead to changes in the nonlinear properties of bR, as previously suggested. On the other hand, QDs have charged ligand molecules on their surfaces and the surface groups of the bacteriorhodopsin can have chemical affinity towards the ligand molecules resulting in small changes to the crystalline structure of the bacteriorhodopsin and ensuing changes of the optical properties of the protein. Another possible source is the surface charge of the adsorbed QDs, which can have an influence on the dipole moment that exists across the PM. A series of further experiments were devised and executed in an attempt to elucidate the nature of the bR-QD interactions that are responsible for enhanced nonlinear properties of the PM/QD material.

Wavelength dependence of n_2 enhancement

First of all, it is important to note that many physical phenomena, including optical coupling, show a significant dependence on the frequency of incident light. The chemical and charge effects, on the other hand, are not expected to show any wavelength dependency. For this reason, measurements of NLR properties of PM/QD complexes were extended to wavelengths above the absorption edge of the QDs.

The enhancement of n_2 was measured at 700 nm, 750 nm and 800 nm for the bR/QD complexes with four different molar ratios, as before. At nearly all wavelengths, the best enhancement was observed for 0.5 bR-to-QD complex and for all complexes the enhancement was maximum at 700 nm (Figure 6.9). Above this wavelength, the enhancement was found to diminish with increasing wavelength of the incident beam.

These results suggest that a wavelength-dependent process plays a role in n_2 enhancement. One possibility is that the enhancement is due to some type of nanoscale interaction between the bacteriorhodopsin protein and QDs excited through multi-photon absorption (MPA). QDs are known to exhibit MPA – a process which has a wavelength dependency similar to that observed in above measurements. The nonlinear absorption index of the QD sample used in these measurements, $\beta = -(6.3 \pm 0.2) \times 10^{-7} \text{ m/W}$, is similar to values reported in the literature ($-1 \times 10^{-6} \text{ m/W}$, M. S. Abd El-sadek et al [14]) making the above proposition plausible.

If this theory is viable, then a significant change in the behaviour of the PM/QD system is expected as the absorption mechanism transitions from nonlinear to a linear regime. That is, as the wavelength of the incident light is brought below the absorption edge of the QDs, the enhancement of the NLR properties of the hybrid complexes should either decrease or increase. Experimentally, the enhancement of the n_2 in PM/QD complexes at wavelengths below 700 nm was found to be considerably reduced (Figure 6.9). In fact, even for the highest bR-to-QD molar ratio used, the increase in n_2 never exceeded 80%, compared to ~4000% enhancement for this complex at 700 nm²⁰. This indicates that excitation of QDs does indeed play a role in the enhancement of NLR properties of PM/QD complexes.

The observed reduction of the enhancement effect can be understood by considering the relative increase of bR excitation above and below 700 nm. As mentioned previously, the nonlinear properties of bR are coupled to the properties of its intermediate states and as a result additional excitation of the protein via energy transfer or other process would certainly result in changes of its nonlinear properties. Now, below 700 nm, direct excitation of both QDs and the bR protein occurs, and such excitation is much more significant than excitation of either of the components by MPA above this wavelength. As a result, the additional energy received by bR from QDs, relative to the direct excitation of bR, is greater above 700 nm where only minimum absorption by bR occurs.

²⁰ The increases were evaluated are relative to the n_2 value of a pure QD solution.

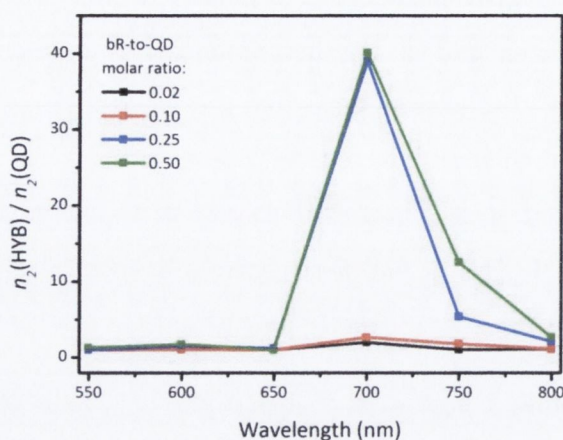


Figure 6.9 | Wavelength dependence of nonlinear refraction properties of PM/QD complexes. The NLR indices of the PM/QD complexes of different bR-to-QD molar ratios all showed similar wavelength trends – the enhancement of the nonlinear refraction properties of complexes was much smaller at wavelengths below the absorption edge of the QDs (~650 nm) than at wavelengths just above the absorption edge.

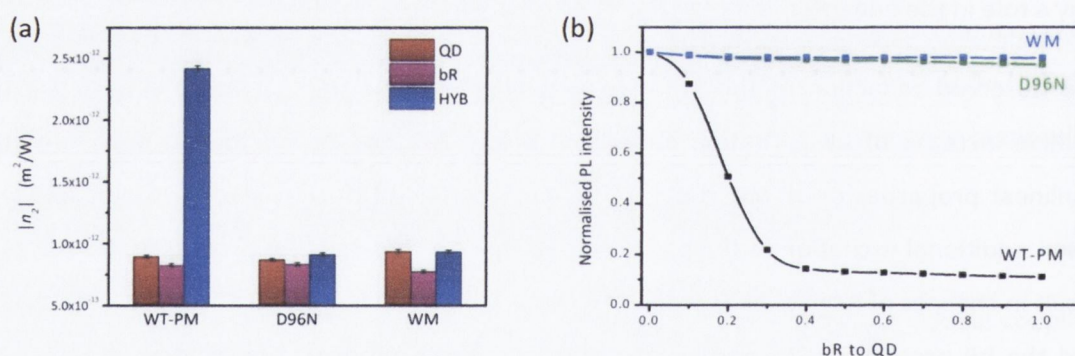


Figure 6.10 | Enhancement of n_2 for different types of bacteriorhodopsin protein. (a) The enhancement of n_2 was found to depend strongly on the type of the bacteriorhodopsin used. Only with wild-type bacteriorhodopsin (WT-PM) a significant enhancement was obtained. For a mutant bacteriorhodopsin and white-membranes very little and no enhancement was observed respectively. This corresponds well with the photoluminescence quenching data for these three types of bacteriorhodopsin, shown in panel (b). The quenching of QDs' photoluminescence (PL) was very significant for the WT-PM (black), signifying efficient energy transfer in this complex. Only a slight quenching of PL was obtained with the mutant bacteriorhodopsin (green), hence only a small percentage of energy donated by QDs is accepted by this protein. Finally, white membranes (WM) were used as a control (blue). Since the acceptor molecule (the retinal) is missing from this protein structure, no energy can be transferred to WMs.

FRET contribution to n_2 enhancement

It is interesting to note that the maximum n_2 enhancement below 700 nm was of the same order of magnitude as the increase of the proton pumping efficiency by bR due to FRET from QDs to the protein. At these wavelengths, the energy transfer between bR and QDs has been shown to occur [8], indicating the possibility that FRET may in fact be the cause of the enhancement effect.

In order to establish the role of FRET in the enhancement process, control experiments were performed involving hybrid complexes composed from different types of bR protein. In particular, the enhancement of n_2 was compared for complexes containing wild-type (WT) bR, white membranes (WMs, see Chapter 5) and D96N mutant. The D96N mutant was chosen because it was found to be very poor in accepting the energy from QDs, while in WM/QD complexes the energy transfer process is altogether absent due to the absence of the acceptor – the retinal molecule.

For each type of bR, 0.5 bR:QD complexes were assembled for 20 minutes, and the measured value of n_2 (at 750 nm) for each complex was normalised to that of the QDs' n_2 . Only the complex containing wild-type bacteriorhodopsin, in which FRET is very efficient (Figure 6.10(b), black data points), showed a measurable increase in n_2 (Figure 6.10(a)). The change in n_2 for the D96N mutant bR was only of the order of a few percent (Figure 6.10(a)), corresponding well with the inefficient quenching of QDs' PL by this bR (Figure 6.10(b), green data points). Finally, no measurable enhancement in $\Delta\Phi_0$ was observed for the white membranes (Figure 6.10(a)), in agreement with the lack of FRET in this complex (Figure 6.10(b), blue data points).

6.4. Conclusions and future work

The presented data represent the first investigations of the nonlinear properties of the PM/QD hybrid material involving comparative measurements of the NLR indices (n_2) of QD solutions, PM suspensions and assembled PM/QD complexes using the Z-scan technique.

Overall, the NLR indices for QDs and bR solutions obtained using the Z-scan technique compared well with the literature values. The NLR index of the QD sample was determined to be between $-3.3 \times 10^{-13} \text{ m}^2/W$ and $-6.5 \times 10^{-12} \text{ m}^2/W$ comparing to, for example, a value of $-7.2 \times 10^{-13} \text{ m}^2/W$ reported by M. S. Abd El-sadek et al [14]. The NLR index of a purple membrane suspension was measured to be between -1×10^{-14} and $-8 \times 10^{-13} \text{ m}^2/W$ depending on the wavelength, while a solution of free retinal molecules was reported to have similar value of NLR index in the -3.9×10^{-14} to $-7.8 \times 10^{-13} \text{ m}^2/W$ range at 532 nm [15].

The NLR indices of the assembled PM/QD complexes were determined to be significantly larger than those of the constituent solutions. The n_2 enhancement upon self-assembly of QDs on PMs showed a dependency on both the bR-to-QD molar ratio and the wavelength of incident light. The maximum enhancement was obtained for the 0.5 bR-to-QD complex at 700 nm, which had $n_2 = -1.32 \times 10^{-11} \text{ m}^2/W$ comparing to the similar values of n_2 of $-3.29 \times 10^{-13} \text{ m}^2/W$ and $-6.07 \times 10^{-13} \text{ m}^2/W$ for the QD and PM solutions respectively. This corresponds to an increase in NLR index by almost 2 orders of magnitude.

The observed molar ratio and wavelength dependencies, together with the temporal evolution of n_2 during complex assembly, suggest that the observed enhancement effect involves excitation of QDs by MPA followed by FRET from QDs to bR. The lack of enhancement of the NLR index for complexes assembled with WMs and D96N mutant bR (instead of the WT bR) is in support of this mechanism. However, other mechanisms, such as non-resonant interactions between QDs and the retinal molecule, have not been excluded. Further Z-scan experiments involving QDs of different sizes can divulge the significance of the MPA by QDs in the enhancement process, while transient spectroscopy of the PM/QD solutions can shed light on the nature of the nanoscale interactions responsible for the enhancement effect.

Finally, the effects observed in this study indicate that the nonlinear optical properties of PM films, which have much larger NLO indices, can be further increased by sandwiching QD layers between the PMs. Considering that many of the proposed applications of bR films are based

on its nonlinear optical properties, the PM/QD hybrid material represents a significant step in the implementation of this unique protein in technological applications.

References

1. Griep, M.H., et al., *Quantum dot enhancement of bacteriorhodopsin-based electrodes*. *Biosens. Bioelectron.* **25**, 1493-1497 (2010)
2. Zeisel, D. and N. Hampp, *Spectral relationship of light-induced refractive index and absorption changes in bacteriorhodopsin films containing wild-type BR_{WT} and the variant BR_{D96N}*. *J. Phys. Chem.* **96**, 7788-7792 (1992)
3. Sifuentes, C., Y.O. Barmenkov, and A.V. Kir'yanov, *The intensity dependent refractive index change of bacteriorhodopsin measured by the Z-scan and phase-modulated beams techniques*. *Opt. Mater.* **19**, 433-442 (2002)
4. Kir'yanov, A.V., et al., *Application of the Z-scan technique to a saturable photorefractive medium with the overlapped ground and excited state absorption*. *Opt. Commun.* **177**, 417-423 (2000)
5. Hampp, N., *Bacteriorhodopsin as a Photochromic Retinal Protein for Optical Memories*. *Chem. Rev.* **100**, 1755-1776 (2000)
6. Sheik-Bahae, M., et al., *Sensitive measurements of optical nonlinearities using a single beam*. *IEEE J. Quantum. Elect.* **26**, 760-769 (1990)
7. Ganeev, R.A., et al., *Investigation of nonlinear refraction and nonlinear absorption of semiconductor nanoparticle solutions prepared by laser ablation*. *J. Opt. a-Pure Appl. Op.* **5**, 409-417 (2003)
8. Rakovich, A., et al., *Resonance Energy Transfer Improves the Biological Function of Bacteriorhodopsin within a Hybrid Material Built from Purple Membranes and Semiconductor Quantum Dots*. *Nano Lett.* **10**, 2640-2648 (2010)
9. Loicq, J., et al., *Non-linear optical measurements and crystalline characterization of CdTe nanoparticles produced by the 'electropulse' technique*. *New J. Phys.* **6**, 32 (2004)
10. Aranda, F.J., et al., *Nonlinear Optical Interactions in Bacteriorhodopsin Using Z-scan*. *Opt. Rev.* **3**, 204-206 (1995)
11. Kodirov, M.K., *Nonlinear refraction and nonlinear absorption of silver aggregates in a polymeric matrix*. *Opt. Spectrosc.* **102**, 73-76 (2007)
12. Ganeev, R.A., et al., *Nonlinear susceptibilities, absorption coefficients and refractive indices of colloidal metals*. *J. Phys. D: Appl. Phys.* **34**, 1602-1611 (2001)
13. Artemyev, M.V., et al., *Optical Properties of Dense and Diluted Ensembles of Semiconductor Quantum Dots*. *Phys. Stat. Sol. (B)* **224**, 393-396 (2001)
14. El-sadek, A.M.S., et al., *Influence of different stabilizers on the optical and linear optical properties of CdTe nanoparticles*. *Opt. Comm.* **In press**, (2011)
15. Bezzera, A.G., Jr., et al., *Z-scan measurements of the nonlinear refraction in retinal derivatives*. *Chem. Phys. Lett.* **276**, 445-449 (1997)

7. CONCLUSIONS

The remarkable advances in nanomaterials have resulted in an impressive degree of control over their fabrication and characterisation, opening up the possibility of utilization of these new materials to probe biological structures at scales much smaller than previously thought possible. The nano-bio-materials have great potential as the next-generation materials since they combine the ever-increasing expertise of the nano- and bio-technologies. In this work, three hybrid model systems were examined for nano-scale interactions at the nano/bio interface with the aim of demonstrating that such interactions can result in increased functional efficiencies of the biomolecules. The three model systems chosen were composed from semiconductor quantum dots and 1) a model photosensitiser (methylene blue dye); 2) photosynthetic reaction centres (RCs) extracted from bacteria; and 3) bacteriorhodopsin (bR) membrane protein within purple membranes (also extracted from bacteria). All three systems were examined using a variety of spectroscopic techniques in order to elucidate the origin of the interactions within them.

In the first system, the methylene blue (MB) dye was employed as the model photosensitiser. Spectroscopic investigations revealed the adsorption and partially dimerisation of the dye on the QDs' surfaces, with ensuing photoinduced charge transfer from quantum dots to methylene blue. In the case of strong spectral overlap between the QDs' emission spectrum and MB absorption spectrum, this process was accompanied by Förster Resonance Energy Transfer (FRET). Both of these transfer processes resulted in additional excitation of MB dye and a consequent increase of ~15% in its production of the singlet oxygen species and its cell kill efficiency, revealed through *in vitro* growth of HeLa cells. The obtained results can be extended to include any general photosensitiser that operates in the visible or NIR spectral regions.

Secondly, the investigation of the QD/RC system described in this thesis is one of the first examples of studies demonstrating efficient energy transfer from QDs to a functional biological complex. In this system, the naturally-occurring light-harvesting complexes were removed from the bacterial reaction centres and QDs were used instead. It was shown that QDs were able to collect the available photon energy and transfer it to the reaction centres. Measurements of the photoluminescence intensity of the special pair in the RCs confirmed

that the energy transfer process resulted in an increase of the photosynthetic efficiency of the RCs (up to 3-fold), thus demonstrating the ability of QDs to act as light-collecting elements in artificial photosynthetic systems. Further optimization of this nano-bio photosynthetic system can improve its efficiency and increase the potential impact of these findings.

The final system, that containing QDs and bR protein, was by far the most complex; however, it also is the most promising for technological applications owing to its stability and the photochromic, photoelectric and charge transfer properties of the bacteriorhodopsin protein. The latter, in the form of proton pumping, is the main biological function of the protein and all other technological-exploitable properties of bR arise from this function. Investigations of the bR/QD system showed that photon energy collected by QDs and transferred to the retinal molecule of the bR resulted in an increase of the proton pumping efficiency of the protein. Several of environmental factors were shown to affect the energy transfer process, including QDs' size, bR mutation and pH of the solution among others, and these factors can be exploited to further optimise the energy transfer process.

Due to the coupling between the biological function of the protein and its optical and electrical properties, the observed increase of the proton pumping efficiency points towards the possibility of improvement of these properties. This was the topic of the last chapter, in which the nonlinear optical properties of the bacteriorhodopsin were studied. Overall, an up to 20-fold enhancement of the bR's nonlinear refractive index was observed (~40-fold enhancement relative to QDs), making this nano-bio-material very promising for nonlinear optical applications such as optical eye limiters and spatial light modulators.

In conclusion, the potential of nanomaterials to improve the in-built functionalities of biomolecules has been successfully shown on an example of semiconductor quantum dots and three model biosystems. The studied here systems have potential applications ranging from medicine to green energy to nonlinear optics, demonstrating the great promise of nanobiotechnology for the development of next-generation materials.

APPENDICES

A. Determination of effective excitation volume for FCS

The accuracy of the quantitative results obtained by FCS relies heavily on the precise knowledge of the dimensions of the effective excitation volume (V_{eff}), which must be determined experimentally. There are three main methods to do this (see Chapter 2) and each has its own advantages. Two methods of determination of V_{eff} were utilised in this work: FCS measurements on a dilution series of a dye and direct measurement by raster scanning of sub-resolution fluorescent particles.

A.1. FCS measurements on a dilution series of a dye

This method uses the fact the average number of particles present in the excitation volume ($\langle N \rangle$) is directly proportional to the overall concentration of the dye molecules in the sample (C) and the effective excitation volume itself:

$$\langle N \rangle = N_A V_{eff} C \quad (\text{A.1})$$

Furthermore, the intensity of the correlation signal ($G(0)$) is inversely proportional to $\langle N \rangle$:

$$\langle N \rangle = \frac{1}{G(0)} \quad (\text{A.2})$$

Hence, the average number of particles in the excitation volume can be obtained from the measured FCS curves. For a series of dye samples of varying concentrations, the effective excitation volume can be calculated from the slope of $\langle N \rangle$ versus C plot.

The biggest advantage of this method is that it can be performed at conditions identical to those of the experimental measurements, thus accounting for almost all of the factors that influence the dimensions of the excitation volume. However, this method is prone to large uncertainties arising from the dilution steps during sample preparation and also saturation effects for high-concentration samples.

For example, when the above procedure was applied to a dilution series of Rhodamine 6G dye (Figure A.1), the error in the effective excitation volume was determined to be almost a half of its value: $V_{eff} = (1.06 \pm 0.47) \text{ fL}$ for a $75 \mu\text{m}$ pinhole at 480 nm excitation.

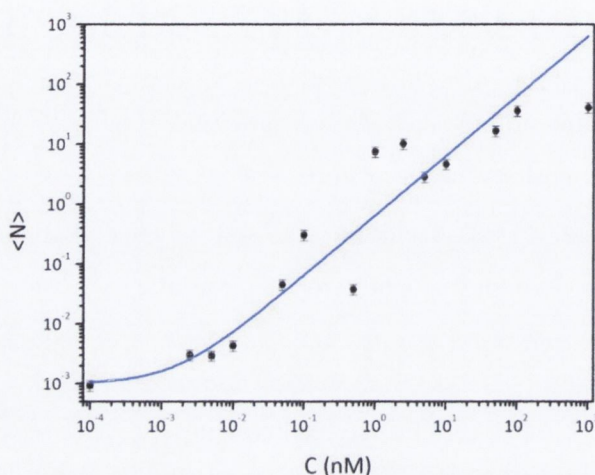


Figure A.1| Calibration of the effective excitation volume using a dilution series of Rhodamine 6G dye. The average number of dye molecules ($\langle N \rangle$) present in the effective excitation volume (V_{eff}) were obtained from the FCS curves using equation A.2. For small dye concentrations, a correction factor χ^2 was introduced to account for the influence of the uncorrelated background signal ($\langle N \rangle = (\chi^2 * G(0))^{-1}$). This data (black data points) were fitted to equation A.1 (blue curve), and from the slope of the fit, a value of $(1.06 \pm 0.47) \text{ fL}$ was obtained for V_{eff} .

A.2. Raster scanning of sub-resolution fluorescent particles

This method involves imaging of a sub-resolution fluorescent particle by raster scanning. Since particle size is smaller than the diffraction limit, it approximately acts as a point source. Therefore, imaging of such a particle directly yields the effective excitation volume. Figure A.2 shows XY (panel a) and XZ (panel b) scans of 100 nm fluorescent beads (TetraSpeck, Invitrogen) under 480 nm excitation, imaged at 10 nm resolution in the XY plane and 100 nm resolution in the Z-direction using a $30 \mu\text{m}$ pinhole. Cross-section of the XY and XZ raster scans were fitted to Gaussian functions to yield the lateral focal radius ($w_0 = 210 \text{ nm}$), and the focal length along the optical axis ($Z_0 = 1.2 \mu\text{m}$) was determined from the $1/e$ intensity points. Combining these values gives the effective excitation volume of $(0.3 \pm 0.02) \text{ fL}$ for 480 nm excitation and collection through $30 \mu\text{m}$ pinhole. Note that this is the simplest and most accurate way to measure V_{eff} ; however, it does not account for many experimental factors (e.g. solvent polarity, refractive index changes).

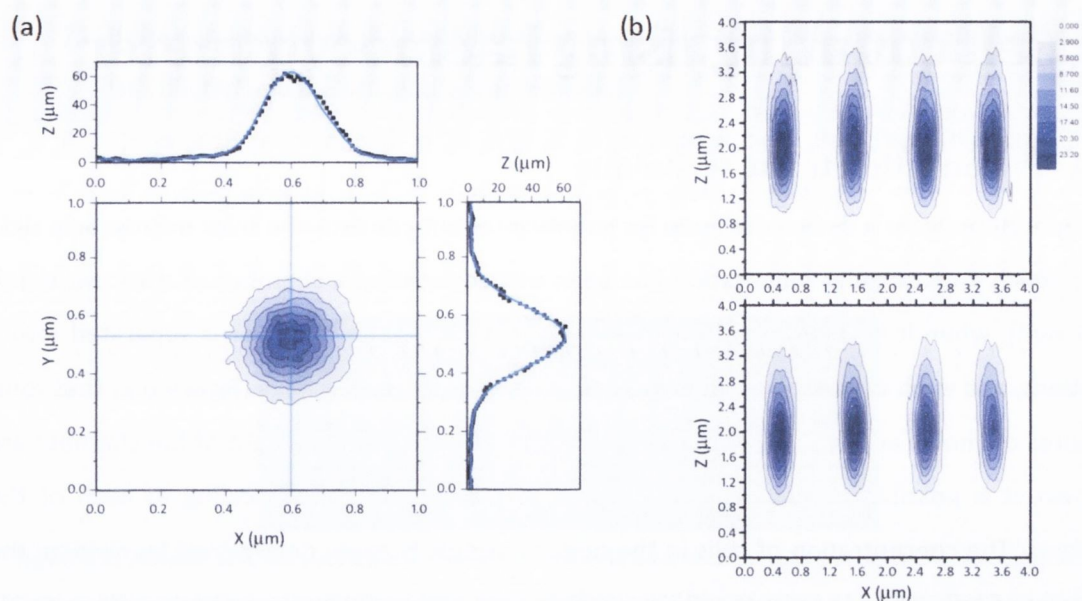


Figure A.2| Raster scans of 100 nm fluorescent beads. (a) XY raster scan of a 100 nm fluorescent bead on a glass substrate. The cross-sections along the X and Y axis (top and to the right) were fitted with Gaussian peak functions (blue) to determine the lateral optical radius (w_0). (b) XZ scans of eight fluorescent beads. The focal length along the optical axis (Z_0) was determined from the $1/e$ intensity points ($\sim 1.2 \mu\text{m}$) along the Z-axis. w_0 and Z_0 values were used to calculate the effective excitation volume ($V_{eff} = 3.0 \pm 0.2 fL$).

B. Cell counting using haemocytometer

B.1. Introduction to the technique

Haemocytometer is a device designed for counting cells. It consists of a thick microscopic slide into which a rectangular indentation has been etched creating a chamber of a known depth (0.1 mm), when it is covered with a coverslip (Figure B.1). This chamber is separated into 2 sections, and each of those has an engraved grid of perpendicular lines (Figure B.2) that form squares of known areas. Since both the area of the squares and the height of the chamber are known, it is possible to calculate the volume of the sample corresponding to each of the squares. The concentration of cells in the original sample is easily determined by dividing the number of cells that can be seen within a certain area of the grid by the corresponding sample volume.

It is important to note that, while this technique is generally considered to be less accurate for the determination of the total number of cells, it can be advantageous due to the fact that it involves visual inspection of the cells while counting making it easier to exclude misshapen and dying cells.

B.2. Protocol for cell counting

1. Cells were detached from the wells of the growth plate, and suspended and thoroughly mixed in their growth medium in a 2 mL eppendorf tube.
2. Haemocytometer and coverslip were washed with water and then wiped with alcohol.
3. After breathing on the surface of the haemocytometer, the coverslip was quickly placed onto the central portion of the haemocytometer and pressed down until Newton's rings could be seen.
4. A small amount of the cell suspension was taken up with a fine tipped pipette. The tip of the pipette was placed against one side of the coverslip near the specially etched grooves. The suspension was aspirated gently to be taken up into the chamber by capillary action.
5. Step 4 was repeated for the other side of the coverslip to fill the second chamber.
6. The haemocytometer was placed under a microscope, fitted with a 60x objective. Cells lying inside the central portion of the grid were counted (Figure B.2). Cells on the bordering triple lines were only counted if they were on the top or left lines.

7. If the number of cells did not fall between the 600 – 1000 cells, the original suspension was diluted and the procedure was repeated.
8. The concentration of cells in the original suspension was calculated according to:

$$\text{No of cells per mL} = \text{Cells counted} * 10^4 * \text{Dilution} \quad (\text{B.1})$$

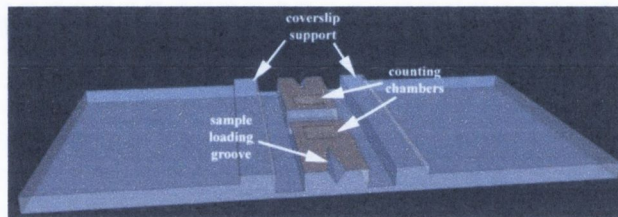


Figure B.1| A model of a haemocytometer. Haemocytometer is used to count cells and other microscopic entities. Once a special coverslip is properly placed onto the coverslip support, two chambers of 0.1 mm height are formed between it and the central portion of the haemocytometer – the counting chambers. Sample, in form of a suspension, is loaded by placing a small amount onto the sample loading grooves, etched close to the counting chambers. On the surface of the counting chambers a grid is etched (see Figure B.2) which is used to determine the concentration of cells in the original solution.

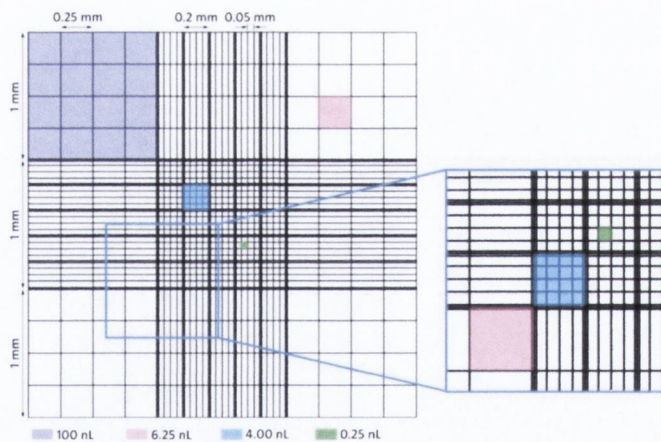


Figure B.2| A haemocytometer grid. The pattern etched on the haemocytometer has 9 large squares, each of 1 mm height/width, corresponding to an area of 1 mm² and 100 nL volume, taking into account the 0.1 mm depth of the counting chamber. One such square is highlighted in purple. There are four large squares in the corners of the grid, and each of these is further divided into 16 squares of 0.25 mm width (pink), corresponding to an area of 0.0625 mm² and a volume of 6.25 nL. The central portions of the grid are divided into 5 sections of 0.2 mm by triple lines (see inset). Each of these is further divided into 4 sections of 0.05 mm by single lines. The resulting grid in the centre has larger squares (blue) of 0.04 mm² area defined by the triple lines, corresponding to 4 nL volume. The smaller squares (green), defined by single lines, are of 0.0025 mm² area, corresponding to 0.25 nL sample volume.